

Application of polarized neutron reflectometry to studies of artificially structured magnetic materials

M. R. Fitzsimmons
Los Alamos National Laboratory
Los Alamos, NM 87545 USA

and

C.F. Majkrzak
National Institute of Standards and Technology
Gaithersburg, MD 20899 USA

Introduction.....	3
Neutron scattering in reflection (Bragg) geometry	6
Reflectometry with unpolarized neutron beams	6
Theoretical Example 1: Reflection from a perfect interface surrounded by two media of infinite extent.....	14
Theoretical Example 2: Reflection from perfectly flat stratified media	16
Theoretical Example 3: Reflection from “real-world” stratified media	22
Reflectometry with polarized neutron beams	30
Theoretical Example 4: Reflection of a polarized neutron beam from a magnetic film	35
Influence of imperfect polarization on reflectivity curves.....	37
“Vector” magnetometry with polarized neutron beams.....	40
Theoretical Example 5: Reflection from a magnetic medium in which the direction of magnetic induction is perpendicular to the applied field and parallel to the plane of the sample	42
A qualitative (and intuitive) understanding of “vector” magnetometry	45
Description of a polarized neutron reflectometer	51
Preparation of the cold neutron beam for a reflectometer at a pulsed neutron source..	52
Polarization of cold neutron beams.....	58
Spin-flippers.....	66
Applications of polarized neutron reflectometry	74
Magnetic vs. chemical structures identified through X-ray and polarized neutron reflectometry	74
Magnetic and chemical structures obtained from vector magnetometry using neutron scattering	86
Summary and conclusions	91
Acknowledgments.....	93
Appendix 1: Instructions for using CO_REFINE.....	94
Data file format	94
Model (or guess) file format	95
CO_REFINE	98
Tips for successful fitting.....	100
A worked example using CO_REFINE	101
Appendix 2: Instructions for using SPIN_FLIP.....	104
Data file format	105
Model (or guess) file format	105
A worked example using SPIN_FLIP.....	107

Introduction

Reflectometry involves measurement of the intensity of a beam of electromagnetic radiation or particle waves reflected by a planar surface and/or interfaces. The technique is intrinsically sensitive to the difference of the refractive index (or contrast) across surfaces and interfaces. For the case of specular reflection, i.e., the case when the angle of reflection, α_r , equals the angle of incidence, α_i , [see Figure 1(a)], the intensity of the reflected radiation is related to the depth dependence of the index of refraction averaged over the lateral dimensions of the surface or interface. In this simplest example of reflectometry, the sharpness of an interface can be quantitatively measured, the distance between two or more planar interfaces can be obtained, and the strength of the scattering potential, i.e., the index of refraction, between the interfaces can be measured relative to that of the medium through which the radiation travels to reach the sample surface (in many cases the surrounding medium is air or vacuum—for neutron scattering there is little distinction). In more complex situations, variations of the refractive index within the plane of the interface may give rise to diffuse scattering or off-specular reflectivity, i.e., radiation reflected away from the specular condition [see Figure 1(b and c)]. From measurements of off-specular reflectivity, correlations between lateral variations of the scattering potential along an interface can be deduced. Off-specular scattering introduces a component of wavevector transfer in the plane of the sample mostly parallel to the incident neutron beam [Figure 1(b)] [1] or perpendicular to it [Figure 1(c)] [23].

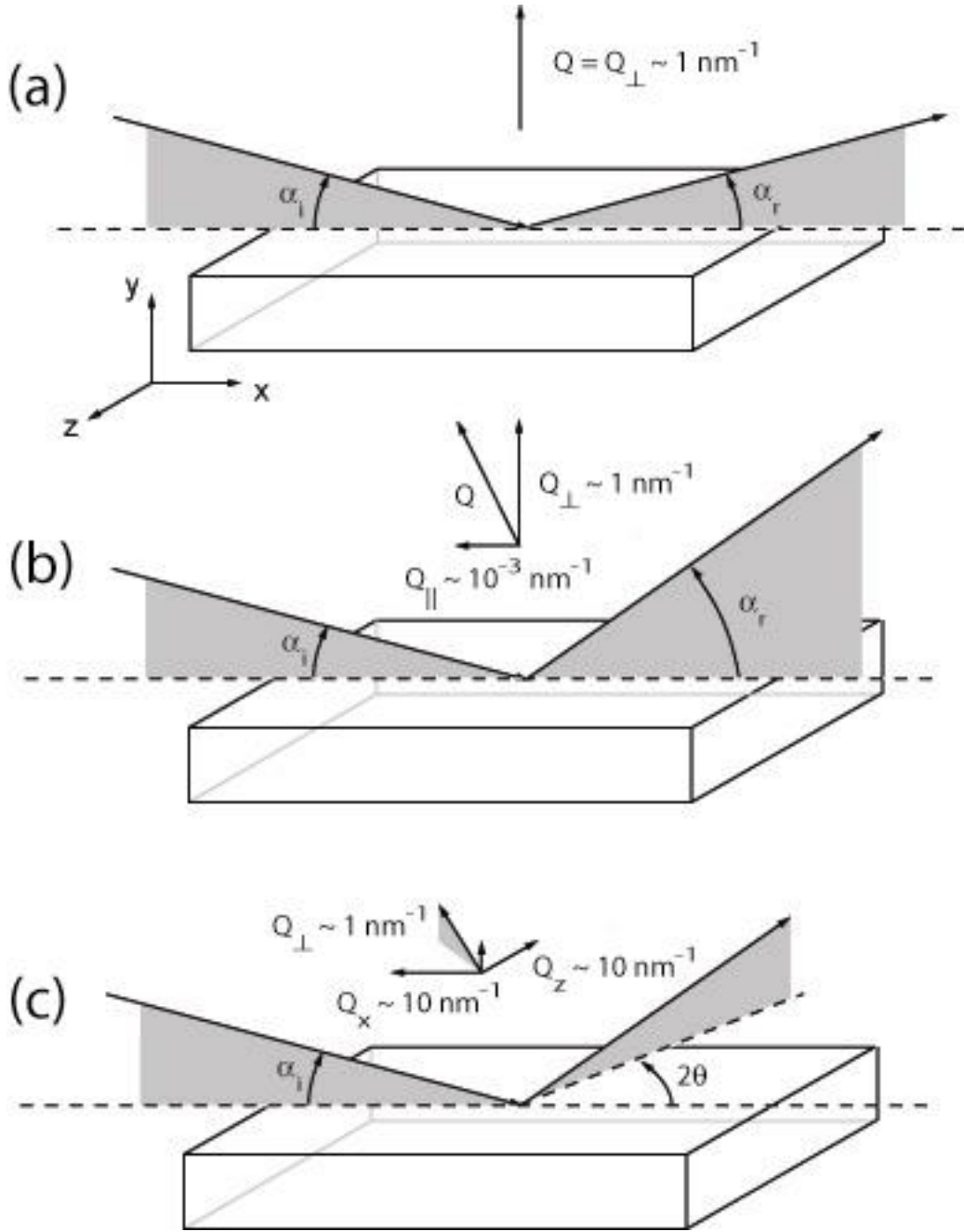


Figure 1 Scattering geometry for (a) specular reflectometry, where $\alpha_r = \alpha_i$, (b) off-specular reflectometry where $\alpha_r \neq \alpha_i$, and (c) glancing incidence diffraction where $2\theta \neq 0$. The components of wavevector transfer, $Q = k_r - k_i$ are shown for each scattering geometry.

So far, the capabilities of reflectometry have been described without regard to the kind of radiation used. Many detailed discussions of X-ray [4, 5, 6, 7, 8, 9, 10] and unpolarized neutron reflectometry [10, 11] from non-magnetic materials can be found in

the literature. Treatments of X-ray reflectometry invariably use concepts of optics and Maxwell's equations. Treatments of neutron reflectometry can be optical in nature, but often treat the neutron beam as a particle wave and use quantum mechanics to calculate reflection and transmission probabilities across interfaces bounding potential wells. In the present chapter, we focus on reflectometry of magnetic thin films and artificially structured magnetic materials using polarized neutron beams.

Polarized neutron reflectometry is a tool to investigate the magnetization profile near the surfaces of crystals, thin films and multilayers. Surface (or interface) sensitivity derives from working in glancing incidence geometry near the angle for total external reflection. Polarized neutron reflectometry is highly sensitive, having measured the absolute magnetization of a monolayer of iron ($\sim 10^{-4}$ emu) with 10% precision [12], and magnetization density as small as 30 emu/cm³ (e.g., as found in Ga_{0.97}Mn_{0.3}As) with comparable precision. Detection of small moments (from samples with surfaces measuring a ~ 4 cm² in area) is combined with excellent depth resolution—a fraction of a nanometer even for films as thick as several hundred nanometers. Reflectometry has enjoyed dramatic growth during the last decade and has been applied to important problems such as, the influence of frozen or pinned magnetization on the origin of exchange bias [13], the influence of exchange coupling on magnetic domain structures [14, 15], and the identification of spatially inhomogeneous magnetism in nanostructured systems [16, 17, 18].

Several descriptions of polarized neutron reflectometry are available in the literature [19, 20, 21, 22, 23, 24, 25]. Recently reviews of polarized neutron reflectometry, one that includes illustrative examples [26], and a second very detailed

account of the scattering of polarized neutron beams, with copious mathematical derivations of formulae, have been published [27,28]. In this chapter, we present a tutorial on polarized neutron reflectometry, a description of a polarized neutron reflectometer at a pulsed neutron source, and examples of applications of the technique.

Neutron scattering in reflection (Bragg) geometry

Reflectometry with unpolarized neutron beams

In Figure 2, we show the general situation for a neutron beam with wavelength λ represented by a plane wave in air (Medium 0) with incident wavevector \mathbf{k}_i ($|\mathbf{k}_i| = k_0 = 2\pi/\lambda$) and reflected wavevector \mathbf{k}_r (reflected by the sample, Medium 1). A portion of the plane wave is transmitted across the reflecting interface with wavevector \mathbf{k}_t . Depending upon the distribution of chemical or magnetic inhomogeneities in the plane of the sample, neutron radiation can be scattered in directions such that $2\theta \neq 0$ and/or $\alpha_r \neq \alpha_i$ [see Figure 1]. The case of elastic and specular ($2\theta = 0$ and $\alpha_r = \alpha_i$) reflection is the simplest to treat.

Neutron scattering is called elastic when the energy $E = \frac{\hbar^2 k_0^2}{2m_n}$ of the neutron is conserved. Thus, the magnitudes of \mathbf{k}_i and \mathbf{k}_r are equal, i.e., $|\mathbf{k}_i| = |\mathbf{k}_r|$. The magnitude of \mathbf{k}_t in Medium 1, $|\mathbf{k}_t| = k_1$, may be (and usually is) different than that of Medium 0.

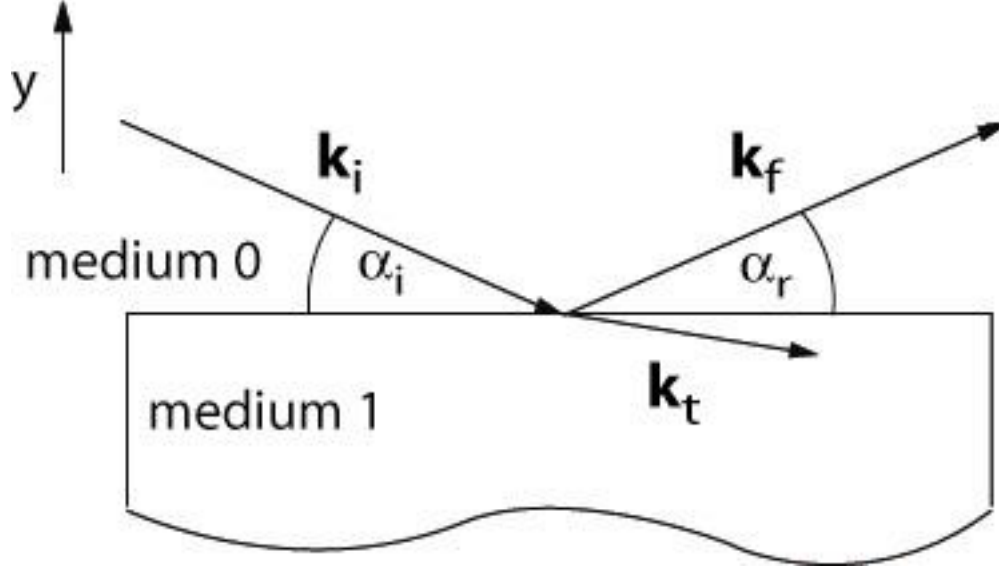


Figure 2 Schematic diagram showing the incident, reflected and transmitted wavevectors. The sample in this case is Medium 1.

The quantity measured in a neutron reflectometry experiment is the intensity of the neutron beam reflected from the surface. The probability of reflection or the reflectivity is given by the reflected intensity divided by the incident intensity. To calculate the reflectivity of an interface, we apply the time-independent Schrödinger equation [29] to obtain a solution for the wave function, Ψ , representing the neutron wave inside and outside of the reflecting sample. Dropping the parts of the wave function with wavevector components parallel to the interface (we consider a potential that varies in only one dimension which cannot change the neutron's wavevector parallel to the interface), the wave functions in mediums 0 and 1 are given by:

$$\begin{aligned}\Psi_0(y) &= e^{+ik_0y} + re^{-ik_0y} \\ \Psi_1(y) &= te^{+ik_1y}\end{aligned}$$

Equation 1

Unless otherwise noted, k_i is the \perp -component of the wavevector \mathbf{k}_i .

The neutron reflectivity, R , of the interface is related to the reflection amplitude, r , by $R = rr^*$. Ψ is obtained by solving Schrödinger's equation:

$$\left[\frac{\hbar^2}{2m_n} \frac{\partial^2}{\partial y^2} + V(y) \right] \Psi(y) = E \Psi(y)$$

Equation 2

where $V(y)$ is the depth dependent scattering potential. For a planar sample, the neutron (nuclear) scattering potential is represented by the expression:

$$V_n = \frac{2\pi\hbar^2}{m_n} \rho(y)$$

Equation 3

where $\rho(y)$ is the neutron scattering length density in units of \AA^{-2} . Owing to the decay in the strength of the reflected neutron beam with wavevector transfer (discussed later), neutron reflectometry usually involves measurements that are restricted to fairly small wavevector transfer, $Q_\perp < 0.3 \text{ \AA}^{-1}$. Over this range of Q_\perp , the scattering medium can be considered to consist of a continuous scattering length density of N (scattering centers or formula units per unit volume) each with coherent neutron scattering length b . For systems composed of a mixture of elements or formula units,

$$\rho = \sum_i^J N_i b_i$$

Equation 4

where J is the number of distinct isotopes, and N_i and b_i are the number density and scattering length for the i -th species. Values of N , b and ρ are given for a number of common materials in Table 1 30.

Invoking the condition of elastic scattering, Equation 2 can be rewritten as:

$$\left[\frac{\partial^2}{\partial y^2} + k_0^2 - 4\pi\rho(y) \right] \Psi(y) = 0$$

Equation 5

In the language of ordinary light optics, the \perp -component of the wavevector in Medium 1, k_I , is related to the \perp -component of the wavevector in Medium 0, k_0 , through the index of refraction, n , by

$$k_1 = nk_0 = \sqrt{1 - \frac{4\pi\rho}{k_0^2}} k_0$$

Equation 6

During an experiment, the intensity of the reflected radiation is measured for selected values of k_0 , which are chosen either by changing the angle of incidence of the beam to the sample surface, α_i , and/or by changing the wavelength, λ , of the neutron beam. For sufficiently small values of k_0 , the index of refraction will be imaginary, so the neutron wave in Medium 1 is evanescent (the wave does not loose energy to Medium 1 [31]). Therefore, the wave is reflected by the sample with unit probability. The wavevector transfer Q_\perp at which n obtains a real component is the called the critical edge, Q_c . For $Q_\perp < Q_c$, the reflected intensity is unity, and provides a means to normalize the reflectivity to an absolute scale (in contrast to small angle neutron scattering). Since the reflectivity of the sample is unity below Q_c , the scattering in this region is strong, so a dynamical treatment of the scattering is required. By dynamical, we mean the wave function inside Medium 1 is not the same as that illuminating the sample. Because the Born approximation [29] is a perturbation theory, it is valid for weak scattering, e.g., small-angle neutron scattering in transmission geometry, so this approximation is not

adequate for calculating reflection of neutrons or X-rays at glancing angles from planar or nearly planar interfaces.

Table 1 Listing of common elements and their neutron nuclear and magnetic scattering length densities.

Material	Number density, N [\AA^{-3}]	Nuclear scattering length, b [\AA]	Magnetic moment, μ [μ_B]	Nuclear scattering length density, ρ_n [\AA^{-2}]	Magnetic scattering length density, ρ_m [\AA^{-2}]
Ag	5.86×10^{-2}	5.92×10^{-5}		3.47×10^{-6}	
Al	6.02	3.45		2.08	
Al ₂ O ₃	2.13	24.4		5.21	
Au	5.90	7.90		4.66	
Co	9.09	2.49	1.715	2.26	4.12×10^{-6}
Fe	8.47	9.45	2.219	8.00	4.97×10^{-6}
FeF ₂	2.75	20.76		5.71	
Fe ₂ O ₃ (hematite)	2.00	36.32		7.26	
Fe ₃ O ₄	1.35	51.57	4.1	6.97	1.46×10^{-6}

(magnetite)					
GaAs	2.21	13.87		3.07	
LaAlO ₃	1.84	29.11		5.34	
LaFeO ₃	1.65	35.11		5.78	
LaMnO ₃	1.71	21.93		3.75	
MgF ₂	3.07	16.68		5.12	
MgO	5.35	11.18		5.98	
MnF ₂	2.58	7.58		1.96	
Nb	5.44	7.05		3.84	
Ni	9.13	10.3	0.604	9.40	1.46×10^{-6}
⁵⁸ Ni	9.13	14.4	0.604	13.14	1.46×10^{-6}
⁶² Ni	9.13	-8.7	0.604	-7.94	1.46×10^{-6}
Ni ₈₁ Fe ₁₉	8.93	10.14	1.04	9.06	2.46×10^{-6}
NiO	5.49	16.11		8.84	
Pd	6.79	5.91		4.01	

Pt	6.60	9.60		6.34	
Pu	4.88	5.8±2.3		2.8±1.1	
Si	4.99	4.15		2.07	
SiO ₂	2.66	15.76		4.19	
SrTiO ₃	1.68	21.00		3.54	
U	4.82	8.417		4.06	
V	6.18	-0.38		-0.23	

Theoretical Example 1: Reflection from a perfect interface surrounded by two media of infinite extent

The goal of a reflection experiment is to determine the distribution of material within the sample from measurements of the sample reflectivity as a function of Q_{\perp} . To accomplish this goal, we need to determine the probabilities that the wave function is reflected and transmitted by the sample. Conservation of neutron intensity, i.e., $|\Psi|^2 = 1$, and conservation of momentum require that $\Psi(y)$ and its derivative, $\frac{\partial \Psi}{\partial y}$, be continuous across the interface. Thus,

$$\begin{pmatrix} \Psi_0(0) \\ \left. \frac{\partial \Psi_0}{\partial y} \right|_{y=0} \end{pmatrix} = \begin{pmatrix} \Psi_1(0) \\ \left. \frac{\partial \Psi_1}{\partial y} \right|_{y=0} \end{pmatrix} \Rightarrow \begin{pmatrix} 1 + r \\ ik_0(1 - r) \end{pmatrix} = \begin{pmatrix} t \\ ik_1 t \end{pmatrix}$$

Equation 7

Solving Equation 7 for r , the reflection amplitude of a single interface between two media of infinite extent, gives:

$$r = \left(\frac{k_0 - k_1}{k_0 + k_1} \right)$$

Equation 8

from which the reflectivity of a single interface is obtained:

$$R = rr^* = \left(\frac{k_0 - k_1}{k_0 + k_1} \right) \left(\frac{k_0 - k_1}{k_0 + k_1} \right)^* = \left(\frac{1 - n}{1 + n} \right) \left(\frac{1 - n}{1 + n} \right)^*$$

Equation 9

As an example to illustrate application of Equation 9, we consider the case of an unpolarized neutron beam reflecting from a perfectly smooth silicon substrate (surrounded by air). The neutron scattering length density for Si is $\rho_{\text{Si}} = 2.07 \times 10^{-6} \text{ \AA}^{-2}$

(obtained from the entries listed in Table 1), and the depth dependence of the scattering length density profile for the sample is shown in Figure 3(a). The reflectivity versus Q_{\perp} [Figure 3(b)] is calculated using Equation 9. The position of the critical edge, Q_c , is determined by the condition $n = 0$, i.e., $Q_c = 4\sqrt{\pi\rho_{Si}}$.

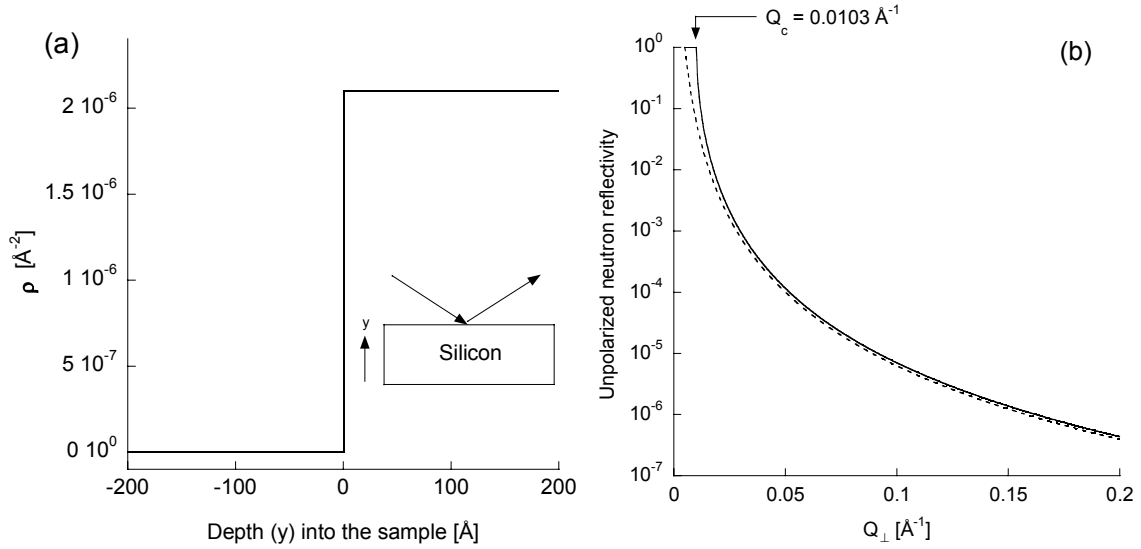


Figure 3 (a) Unpolarized neutron scattering length density profile of a perfect interface between air and a silicon substrate (inset). **(b)** The calculated reflectivity for the interface (a) is shown by the solid curve. The dashed curve represents a reflectivity curve calculated using the Born approximation (see text) and varies as Q_{\perp}^{-4} normalized to 0.9 times the solid curve at $Q_{\perp} = 0.2 \text{ \AA}^{-1}$ (see text).

The dynamical calculation of the silicon substrate reflectivity [solid curve, Figure 3(b)] in the region of $Q_{\perp} \sim 0.1 \text{ \AA}^{-1}$ is similar to that obtained the Born approximation (i.e., the kinematical case, dashed curve) from which the reflectivity is equated to the Fourier transform of the scattering length density profile:

$$R_{BA} \propto \frac{1}{Q_{\perp}^2} \left| \int_{-\infty}^{\infty} e^{iQ_{\perp}y} \rho(y) dy \right|^2$$

Equation 10

However, for smaller values of Q_{\perp} the two reflectivity curves diverge.

In the large Q_{\perp} regime, the decay of the curve scales as Q_{\perp}^{-4} . This decay, called the Fresnel decay [6], is a property of reflection from a planar surface, and thus contains little information leading to a better understanding of the spatial representation of matter beneath the surface. However, the Fresnel decay rapidly diminishes the reflected neutron beam intensity until it can become swamped by external sources of background, including incoherent scattering from the substrate.

Theoretical Example 2: Reflection from perfectly flat stratified media

For the case of reflection from a single perfect interface, there is little additional information that can be obtained beyond that provided by the position of the critical edge (surface roughness can also be measured—a topic discussed later). More interesting and realistic cases involve reflection from stratified media. In these cases, the scattering length density is not constant with depth, and indeed abrupt changes of the scattering length density, such as those produced by buried interfaces, modulate the reflectivity.

Now consider the representation of a stratified sample in Figure 4—one depicting reflection of a neutron beam from a perfect interface formed by the boundary between air and the surface of a thin film with thickness Δ that is in contact with a smooth Si substrate of infinite thickness.

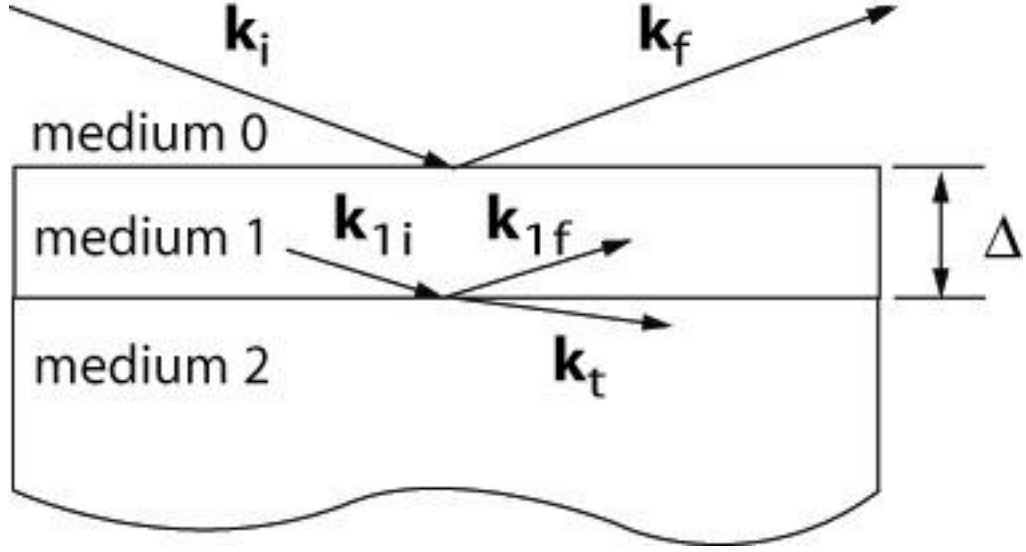


Figure 4 Schematic diagram showing the wavevectors in a stratified medium. The thickness of the thin film is Δ .

The wave functions in the different media are:

$$\Psi_0(y) = e^{+ik_0y} + re^{-ik_0y}$$

$$\Psi_1(y) = Ge^{+ik_1y} + He^{-ik_1y}$$

$$\Psi_2(y) = te^{+ik_{21}y}$$

Equation 11

Again Schrödinger's equation is solved yielding a matrix equation from which the reflection and transmission amplitudes, r and t , can be obtained:

$$\overline{\overline{M}}_1(\Delta) \begin{pmatrix} 1+r \\ ik_0(1-r) \end{pmatrix} = \begin{pmatrix} t \\ ik_2t \end{pmatrix} e^{ik_2\Delta}$$

Equation 12

and

$$\overline{\overline{M}}_1(\Delta) = \begin{pmatrix} \cos(k_1\Delta) & \frac{1}{k_1}\sin(k_1\Delta) \\ -k_1\sin(k_1\Delta) & \cos(k_1\Delta) \end{pmatrix}.$$

Equation 13

Equation 12 represents two simultaneous equations that can be solved to obtain r . (Note, Equation 7 is recovered for the case of a single (air/substrate) interface for the case of $\Delta = 0$.)

$$r = \frac{r_{01} + r_{12}e^{ik_1 2\Delta}}{1 + r_{01}r_{12}e^{ik_1 2\Delta}}$$

$$r_{mn} = \frac{k_m - k_n}{k_m + k_n}$$

$$k_j = n_j k_0 = \sqrt{1 - \frac{4\pi\rho_j}{k_0}} k_0$$

Equation 14

To calculate a reflectivity curve, a value of Q_\perp is chosen from which k_0 ($= Q_\perp/2$, a real quantity) is obtained. Next, the \perp -components of the wavevector in Medium 1 and Medium 2 are calculated (using Equation 14) from which the reflection amplitudes for a pair of interfaces are obtained. The reflection amplitudes for an ensemble of interfaces (in this case two, see Equation 14), r , is related to the reflection amplitudes of each interface, r_{01} and r_{12} (here, the amplitude of the wave reflected by the interface between Medium m and Medium n is called r_{mn}), in the ensemble after combination with a phase factor, $e^{ik_1 2\Delta}$, as appropriate (the wave reflected by the interface between Medium 1 and Medium 2 is out of phase by the path length 2Δ with respect to the wave reflected by the interface between Medium 0 and Medium 1). This procedure was performed to obtain the reflectivity curve (Figure 5) for a sample consisting of a 20 nm thick perfectly flat layer of material with the nuclear scattering length density of Fe on a perfect Si substrate.

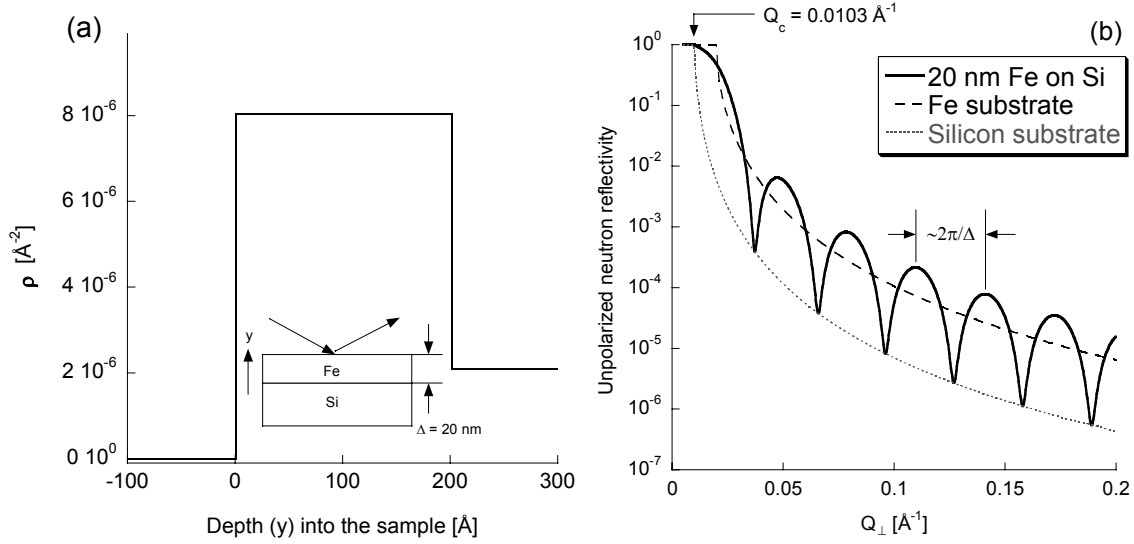


Figure 5 (a) The nuclear scattering length density profile of a perfect thin iron film on silicon (inset). (b) The reflectivity of the sample is shown as the solid curve. The reflectivities of a silicon substrate (dotted curve) and a substrate with the nuclear scattering length density of iron (dashed curve) are shown for comparison.

The most notable feature of the solid curve [Figure 5(b)] is the oscillation of the reflectivity. The period of the oscillation in the kinematical limit (far from the critical edge where dynamic effects are most pronounced) is approximately equal to $2\pi/\Delta$. The amplitude of the oscillation is related to the contrast or difference between the scattering length densities of the iron film and silicon substrate. A second notable feature is the position of the critical edge, which for the 20 nm Fe/Si sample still occurs at a position coinciding with that of the silicon substrate and not at the position for an iron substrate [compare the dotted and dashed curves in Figure 5(b)]. Unlike the case for X-ray reflectometry, in which only a couple of nanometers of material is sufficient to be opaque, and thus create a well-defined critical edge, the critical edge for neutron reflectivity is often determined by the sample substrate, and not the thin film owing to the fact that a neutron beam is a highly penetrating probe.

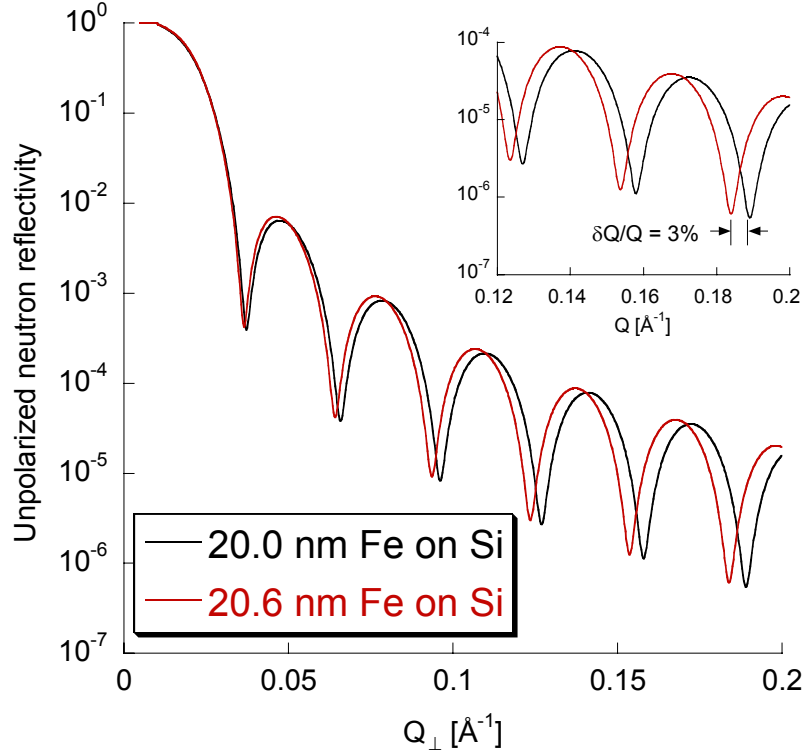


Figure 6 Comparison of reflectivity curves from Fe films with different thicknesses. The difference of 3% in thickness would be easily resolved.

One strength of reflectometry is its ability to measure layer thickness with very high precision and accuracy (for a discussion of the distinction see Ref. [32]). An illustrative example is to compare the calculated reflectivity curves for iron films of 20.0 nm and 20.6 nm thickness—corresponding to a 3% change in film thickness (Figure 6). The shift between the reflectivity curves at large wavevector transfer is easily distinguished, because the resolvable wavevector transfer is smaller than the shift. For small scattering angles, the resolution of a reflectometer, $\delta Q/Q$ is approximately given by:

$$\left(\frac{\delta Q}{Q}\right)^2 = \left(\frac{\delta \theta}{\theta}\right)^2 + \left(\frac{\delta \lambda}{\lambda}\right)^2$$

Equation 15

The first term is determined by a combination of factors including sample size and the dimensions of slits that collimate the incoming neutron beam. For glancing angles of incidence (typically less than 5°), $\delta\theta/\theta$ is of order 2% (root-mean-square). The second term is determined by how well the wavelength of the incident neutron beam is measured. For situations in which a graphite monochromator selects the wavelength (as used for example at a nuclear reactor), $\delta\lambda/\lambda$ is typically 1 to 2% (rms). For situations in which the time-of-flight technique measures neutron wavelength (as used for example at a short pulsed neutron source) $\delta\lambda/\lambda$ is typically 0.2% (rms). So, with little effort, the resolution of a reflectometer in $\delta Q/Q$ can be made less than 3% (rms). Consequently, the change of fringe phase, which is about 3% for the case illustrated in Figure 6, can be readily measured.

In contrast to measuring sub-nanometer changes in film thickness, detection of a single sub-nanometer thick film is considerably more challenging. The Fresnel decay of the reflectivity restricts the degree to which perturbations in the scattering length density profile over thin layers can be measured. Let Q_{\max} is the maximum value of Q_\perp that can be measured before the reflectivity, R_{\min} , is approximately equal to the instrumental background. Thin films having thickness $\Delta > 2\pi/Q_{\max}$ can perturb the reflectivity by superimposing oscillations on the Fresnel decay. In principle, by measuring the period and amplitude of the oscillations, information about the thickness of the thin film and its composition can be inferred. On the other hand, for films with thickness $\Delta < 2\pi/Q_{\max}$ the perturbation to the reflectivity might well be missed on account that the first pair of fringe maximum and minimum occur at wavevector transfer so large that the intensity of

the reflected beam is below R_{min} (in other words, the oscillations of the reflectivity curve might be swamped by instrumental background).

Neutron reflectivity has been measured to values of $R_{min} = 10^{-8}$ under ideal conditions. In these conditions, Q_{max} might be on order of 0.3 \AA^{-1} , so detection of films as thin as 2 nm might be possible. However, most experiments are not conducted under ideal circumstances. For example, experiments usually involve sample environment equipment, e.g., cryostats etc., or samples that are either not perfectly smooth or are themselves sources of incoherent scattering. In these situations neutron reflectivity measurements to less than 10^{-7} are often not achievable.

Theoretical Example 3: Reflection from “real-world” stratified media

The first two examples of perfect interfaces illustrate the importance of the critical edge (providing a means to place the reflectivity curve on an absolute scale), fringe period (related to layer thickness) and fringe amplitude (related to change of, or contrast between, scattering length density across an interface). Since real systems can be less than perfect, we consider the case of rough or diffused interfaces. This case serves to show how reflectometry can be a useful tool to study systems that are imperfect (indeed reflectometry provides a useful measure of imperfection).

Consider the case where the diffusion of Fe and Si across the Fe/Si interface in the previous example obeys Fick’s second law [33]. We further assume the characteristic diffusion length, σ , of Fe into the Si matrix is the same as Si into the Fe matrix (though this assumption is unlikely to be correct). In this case, the concentrations of Fe and Si with depth (in units of atoms/\AA^3) are given by:

$$N_{Fe}(y) = N_{Fe} \left[1 - \operatorname{erf} \left(\frac{y - \Delta}{\sqrt{2}\sigma} \right) \right]$$

$$N_{Si}(y) = N_{Si} \left[1 + \operatorname{erf} \left(\frac{y - \Delta}{\sqrt{2}\sigma} \right) \right]$$

Equation 16

After substitution of Equation 16 into Equation 9, and using the appropriate values of the neutron scattering lengths and densities for Fe and Si (see Table 1), the neutron scattering length density profile is obtained:

$$\rho(y) = b_{Fe} N_{Fe} + \frac{b_{Si} N_{Si} - b_{Fe} N_{Fe}}{2} \left[1 + \operatorname{erf} \left(\frac{y - \Delta}{\sqrt{2}\sigma} \right) \right]$$

Equation 17

The variation of the neutron scattering length density across the interface is represented by an error function connecting the scattering length densities of pure Fe and pure Si. We note the derivative of the error function with argument $\frac{y - \Delta}{\sqrt{2}\sigma}$ is proportional to a Gaussian function with root-mean-square width of σ [34]. The scattering length density profile for a 20 nm thick Fe layer bounded by a diffuse air/Fe surface (i.e., a rough surface) and diffuse Fe/Si interface with characteristic widths of $\sigma = 5 \text{ \AA}$ is shown in Figure 7(a).

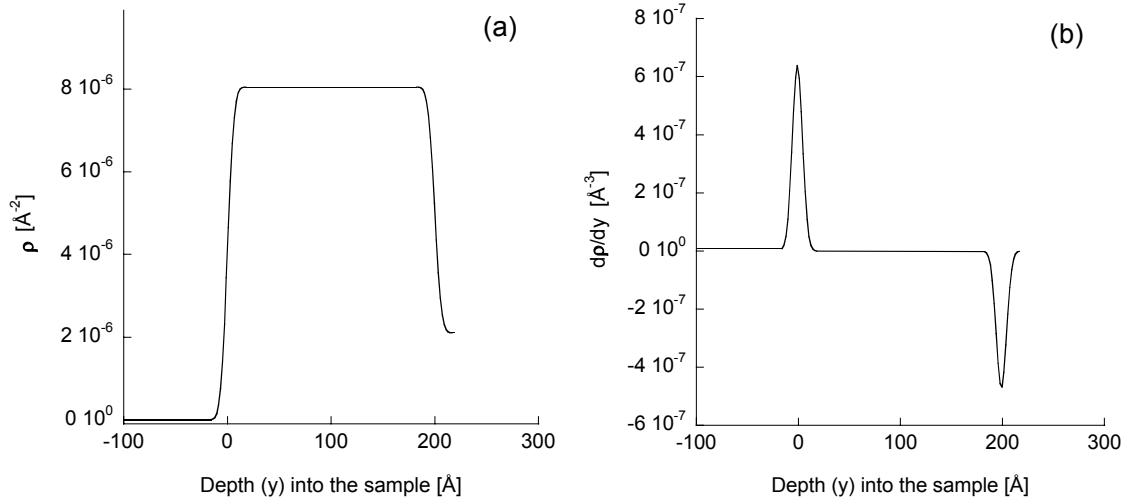


Figure 7 (a) Representation of the Fe/Si sample with rough and/or diffuse interfaces. (b) The derivative of the scattering length density profiles consisting of a pair of Gaussian profiles from which (a) is obtained upon integration.

While the scattering length density profile in Figure 7(a) can be obtained using Equation 17, in fact the profile shown in the figure was obtained by integrating the derivative of the scattering length density profile with respect to depth (y-coordinate) [Figure 7(b)]. The peaks in Figure 7(b) are Gaussian peaks whose positions, widths and integrals correspond to the positions, diffusion or roughness widths, and contrast across the interfaces, respectively. For example, the integral of the peak at $y = 0 \text{ \AA}$ in Figure 7(b) is $\rho_{\text{Fe}} - \rho_{\text{air}} = 8 \times 10^{-6} \text{ \AA}^{-2}$. One motivation for constructing the derivative of the scattering length density profile (and then integrating it) is to allow the possibility for interfaces to be positioned close together. By close together we mean the thickness of one or both layers on either side of an interface is thinner than the rms width attributed to the interface. While arguments can be made whether such a situation is physically meaningful, mathematically the situation corresponds to one where tails of adjacent Gaussian peaks overlap, and certainly such a profile can be integrated. When the tails of two Gaussian peaks overlap (significantly), the profile obtained from integrating the

derivative profile will not yield an error function variation between the two interfaces, but may nevertheless produce a calculated reflectivity curve that closely resembles a measured reflectivity. It should be emphasized that only in situations where $\sigma_{mn} \ll \Delta_m$ and $\sigma_{mn} \ll \Delta_n$, should the value of σ_{mn} be interpreted as an interface width and Δ as a layer thickness. Otherwise, the parameters of a density profile—ones that yield a well-fitting reflectivity curve, have little meaning, though the density profile might accurately represent the scattering potential of the system.

The process for calculating the reflectivity of the “roughened” sample first involves approximating the continuous profile in Figure 7 by a discrete sequence of thin slabs of width δ with step-like changes in scattering length density. The choice of δ , i.e., the thickness over which ρ is constant, is made such that $\delta \ll 2\pi/Q_{\max}$ —a relation assuring the Sampling Theorem of Fourier analysis [35] is satisfied. An example of such an approximation for $\delta = 2 \text{ \AA}$ is shown in Figure 8.

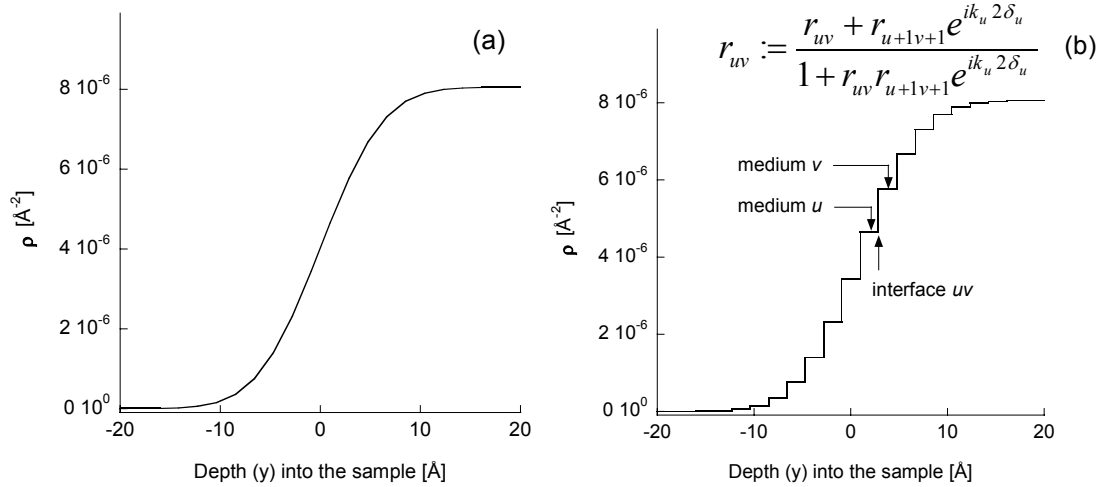


Figure 8 (a) Variation of the scattering length density profile of the air/Fe interface for $\sigma = 5 \text{ \AA}$ is shown. (b) Approximation of the continuous function in (a) using discrete steps.

There are two common approaches to calculate the (dynamical) reflectivity using the approximate scattering length density profile shown in Figure 8(a). The first approach, which is suitable for calculating the scattering length density profiles from scalar potentials (Equation 3 is an example of a scalar potential) is to use Equation 14 to calculate the reflection amplitude of the interface between the bottom-most thin slab and the infinitely thick substrate. Let the reflection amplitude of this interface be r_{mn} (bounded by Medium $m = n-1$ and Medium n —the substrate). Then, the reflection amplitude of the next higher interface—the $m-1$ -th interface, is computed using r_{mn} as the reflection amplitude of the phase-shifted term in Equation 14. This equation is applied recursively (as indicated in Figure 8(b) for the uv -th interface) until the top interface (the air/sample interface) is reached. Calculation of the reflectivity by recursively applying Equation 14 (for a particular Q_{\perp}) is required in order to properly account for dynamical scattering of the neutron beam by the sample surface at glancing angles. In other words, were the Born approximation a good representation of the scattering, then a recursive calculation to obtain the reflectivity curve would not be necessary. The recursive calculation is often referred to as the Parratt formalism [4].

The second approach to calculate the reflectivity curve is to generalize the matrix relation (Equation 12) for an arbitrary number of thin slabs, and then to solve the simultaneous equations to obtain the reflection amplitude of the ensemble (i.e., the entire sample). The second approach is one that can be used to calculate the reflection amplitude of a sample that might be represented by a scalar or vector potential (an example of a vector potential is one that includes the vector magnetization of a sample).

The matrix relation is generalized to the case of an any number of thin slabs as follows (for a detailed derivation see Ref. [28]):

$$\prod_{j=n-1}^0 \overline{M_j(\delta_j)} \begin{pmatrix} 1+r \\ ik_0(1-r) \end{pmatrix} = \begin{pmatrix} t \\ ik_n t \end{pmatrix} \prod_{j=n-1}^0 e^{ik_n \delta_j} = \begin{pmatrix} t \\ ik_n t \end{pmatrix} e^{ik_n \Delta}$$

$$\overline{M_j(\delta_j)} = \begin{pmatrix} \cos(k_j \delta_j) & \frac{1}{k_j} \sin(k_j \delta_j) \\ -k_j \sin(k_j \delta_j) & \cos(k_j \delta_j) \end{pmatrix}$$

$$\Delta = \sum_{j=1}^{n-1} \delta_j$$

Equation 18

The subscript “j” in Equation 18 represents the j-th medium or slab. So, for example, k_j is the magnitude of the \perp -component of the wavevector in the j-th medium (see Equation 14), and δ_j is the thickness of the medium over which the scattering length density is considered constant [2 Å for the case of Figure 8(b)].

The reflectivity calculated for a 20 nm thick Fe film with roughened interfaces [whose scattering length density profile is shown in Figure 8(b)] is the solid curve in Figure 9. The case for the ideal Fe film [whose scattering length density profile is shown in Figure 5(b)] is the dashed curve in the figure.

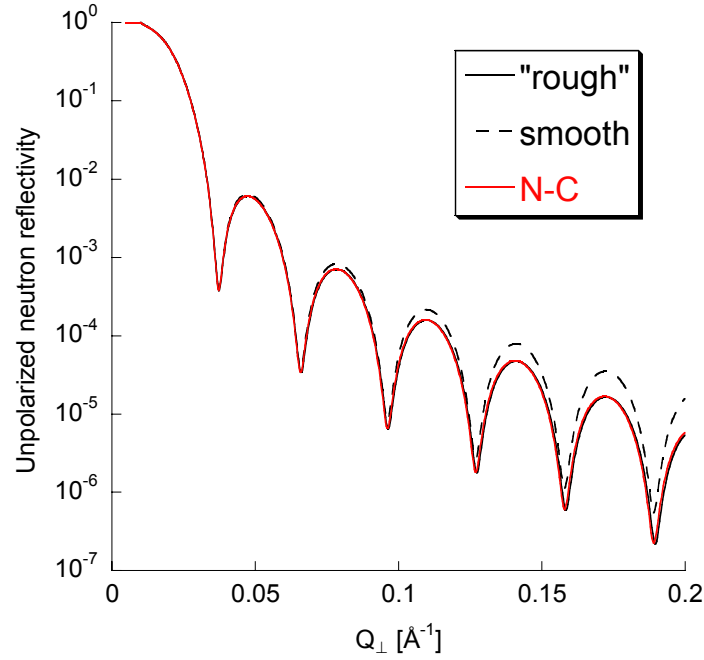


Figure 9 The influence of rough or diffuse interfaces is to attenuate the reflectivity with Q_{\perp} . The “rough” and “N-C” (computed using the Nevot and Croce relation) curves are essentially identical.

The reflectivity curve of a sample with rough or diffuse interfaces is attenuated more so than that of a smooth sample. The attenuation increases with Q_{\perp} . In fact, for the case of a single interface, Nevot and Croce [36] have analytically shown that the reflection amplitude of a single rough interface, r_r , having short length-scale roughness ($Q_{\perp}\sigma \ll 1$) is related to that of the ideal interface, r_i , by the relation:

$$r_r = r_i \exp(Q_{\perp} Q'_{\perp} \sigma^2 / 2)$$

Equation 19

where Q'_{\perp} ($= \mathbf{k}_{If} - \mathbf{k}_{Ii}$) is the wavevector transfer in the sample. As the kinematical limit is approached (i.e., $Q'_{\perp} \rightarrow Q_{\perp}$), the attenuation factor is identical to a “static” Debye-Waller factor [37] (application of Equation 19 to the “smooth” curve in Figure 9 yields the red “N-C” curve). The important consequence of this observation is that interface roughness (or diffusion) will further limit the accessible region of wavevector transfer,

and consequently the sensitivity of reflectometry to changes of the scattering length density profile over thin layers. The attenuation of the reflectivity with roughness is a strong function of σ and Q_{\perp} ; thus, more information can be extracted from samples with smooth interfaces than those with rough interfaces (although the physics of rough interfaces are often interesting!). For many experiments, useful information can be obtained from samples with (rms) interface roughness on the order of 10 Å, whereas, for samples with interface roughness of 20+ Å, success of the experiment may be hopelessly compromised.

The previous three theoretical examples have illustrated useful concepts and interpretations of reflectivity curves. The measurements and their interpretations are summarized in Table 2.

Table 2 Listing of measurements and the information yielded by the measurements.

Measurement feature	Information obtained from a sample of cm ² or so size
Position of critical edge, Q_c	Nuclear (chemical) composition of the neutron-optically thick part of the sample, often the substrate.
Intensity for $Q < Q_c$	Unit reflectivity provides a means of normalization to an absolute scale.
Periodicity of the fringes	Provides measurement of layer thickness. Thickness measurement with uncertainty of 3% is routinely achieved. Thickness measurement to less than 1 nm can be achieved.
Amplitude of the fringes	Nuclear (chemical) contrast across an interface.
Attenuation of the reflectivity	Roughness of an interface(s) or diffusion across an

	interface(s). Attenuation of the reflectivity provide usually establishes a lower limit (typically of order 1-2 nm) of the sensitivity of reflectometry to detect thin layers.
--	--

Reflectometry with polarized neutron beams

In the previous section, neutron reflectometry was discussed in terms of the reflection of neutron beams from scattering potentials that are purely nuclear in origin. Since the neutron possesses an intrinsic magnetic moment and spin, the scattering potential may be spin dependent. There are two reasons that the interaction between a neutron and matter may depend on the neutron's spin. In some scattering processes (e.g., incoherent scattering of neutrons by hydrogen), the nuclear spin of an atom can interact with the spin of a neutron. On other occasions, the nuclei in a material from which the neutron scatters, may possess net spin and be polarized. Examples include spin polarized ^3He nuclei [38], or spin polarized Ga or As nuclei in the presence of a magnetic material [39]. The spin dependence of the potential for these examples involves two neutron scattering lengths, b^+ and b^- , where the sign of the term indicates whether the spin of the nuclei is parallel or anti-parallel to the laboratory magnetic field of reference (see Figure 1), which will later be identified with the polarization axis of the neutron beam.

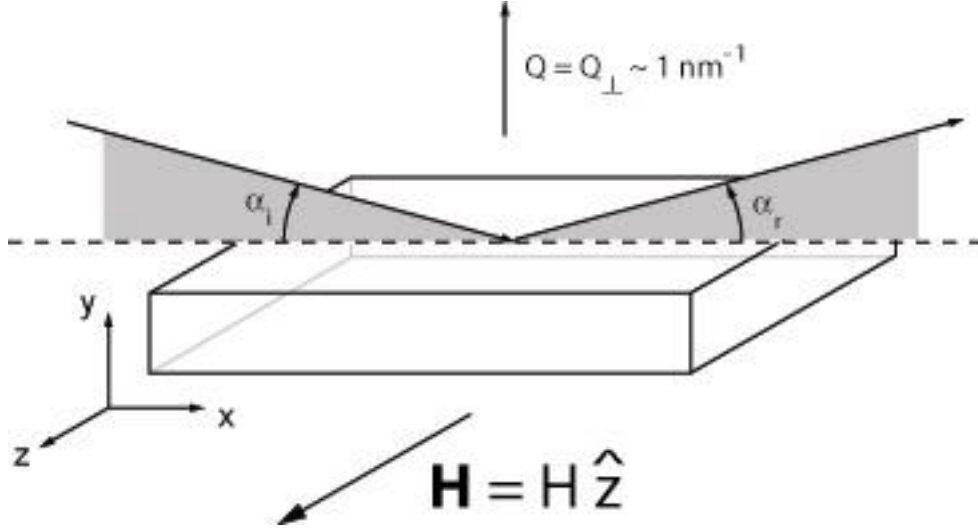


Figure 10 Diagram of a reflection experiment in which the sample is immersed in a magnetic field.

A commonly encountered second case involves the interaction of the neutron spin with atomic magnetism or other source of magnetic induction. The modification to the scattering potential (including the nuclear potential) is given by:

$$V = V_n + V_m = V_n \mp \underline{\mu} \cdot \mathbf{B}$$

Equation 20

Here, \mathbf{B} is the (spatially dependent) magnetic induction vector, and $\underline{\mu}$ is the magnetic moment of the neutron, where $\underline{\mu} = \mu_n \underline{\sigma}$, $\mu_n = -1.913 \mu_N$ (the negative sign indicates that the neutron moment and its spin are anti-parallel), and $\underline{\sigma}$ is a linear combination of the (2 x 2) Pauli matrices [29] directed along each of the three orthogonal spatial axes with the magnetic field direction taken to lie along the \hat{z} -axis (Figure 10). The “ \mp ”-sign in Equation 20 is taken to be negative (positive) if the neutron spin is parallel (anti-parallel) to the laboratory field of reference (\mathbf{H} in Figure 10). Since μ_n is negative, the quantity $-\mu_n B$ is positive, thus, adding to a normally positive nuclear scattering length—one for a repulsive potential (Mn, however, is an example of an atom

with a negative scattering length—an attractive potential). Fundamentally, the neutron spin interacts with magnetic induction, \mathbf{B} , so a materials-property that gives rise to \mathbf{B} , e.g., orbital and/or spin moments of atoms, or accumulation of spin in electronic devices, in principle can affect the neutron scattering process. The fact that the neutron spin interacts with magnetic induction and not magnetic field [40, 41, 42, 43] is fortunate, since were this not the case neutron scattering might not be a useful a tool in the study of magnetism.

Expressing the scattering potential V in matrix notation, we obtain [28]:

$$\overline{\overline{V(y)}} = \frac{2\pi\hbar^2}{m_n} \begin{pmatrix} \rho_n & 0 \\ 0 & \rho_n \end{pmatrix} \mp \mu_n \begin{pmatrix} B_z & B_x - iB_y \\ B_x + iB_y & -B_z \end{pmatrix}$$

Equation 21

The elements of the matrices are understood to depend on position, i.e., the nuclear scattering length density term, $\rho_n = \rho_n(y)$, etc. (in principle, dependence on x and z is also possible to observe with off-specular reflectometry). It is important to recognize that while most often the nuclear scattering potential outside of the sample is zero, $\rho_n = 0$, this is not necessarily the case for the magnetic induction. For example, in a polarized neutron reflectometry experiment, some magnetic field (as little as a couple Oe may be needed) is nearly always applied to the sample, in order to maintain the polarization of the neutron beam. Since neutron reflection occurs across interfaces with different scattering length densities (nuclear or magnetic), the *field* applied to the sample and the *field* inside the sample being the same do not yield contrast across the interface. Setting $\mathbf{B} = \mu_0 \mathbf{H} + \mathbf{M}$, where \mathbf{M} is the intensity of magnetization, and for fields applied along \hat{z} , Equation 21 can be rewritten as:

$$\overline{\delta V(z)} = \frac{2\pi\hbar^2}{m_n} \begin{pmatrix} \rho_n & 0 \\ 0 & \rho_n \end{pmatrix} \mp \mu_n \begin{pmatrix} M_z & M_x - iM_y \\ M_x + iM_y & -M_z \end{pmatrix}$$

Equation 22

Equation 22 is a relation for the potential difference, $\overline{\delta V(z)}$, between the sample and the surrounding medium (here, assumed to be air, but for cases in which the sample is not surrounded by air, the nuclear scattering length density of the surrounding medium must also be removed from ρ_n). The neutron magnetic scattering length density can be defined in terms similar to those used to define the neutron nuclear scattering length density (Equation 4).

$$\rho_m = \sum_i^J N_i \mathbf{p}_i = C \sum_i^J N_i \boldsymbol{\mu}_i = C' \mathbf{m} = -\frac{m_n}{2\pi\hbar^2} \mu_n \sum_i^J \mathbf{M}_i$$

Equation 23

The units of the magnetic scattering length, \mathbf{p} , are Å. For the magnetic moment per formula unit, $\boldsymbol{\mu}$, expressed in units of μ_B , $C = 2.645 \times 10^{-5} \text{ Å}\mu_B^{-1}$. If, rather, the volume magnetization density, \mathbf{m} , is known in units of Tesla, then $C' = 2.9109 \times 10^{-5}/4\pi \text{ Å}^{-2}\text{T}^{-1}$; otherwise, for \mathbf{m} in units of emu/cm³, $C' = 2.853 \times 10^{-9} \text{ Å}^{-2}\text{cm}^3/\text{emu}$. Substituting Equation 23 into Equation 22 yields:

$$\overline{\delta V(z)} = \frac{2\pi\hbar^2}{m_n} \begin{pmatrix} \rho_n + \rho_{mz} & \rho_{mx} - i\rho_{my} \\ \rho_{mx} + i\rho_{my} & \rho_n - \rho_{mz} \end{pmatrix}$$

Equation 24

Finally, we associate the so-called non-spin-flip, ρ_{++} and ρ_{--} , and spin-flip scattering potentials, ρ_{+-} and ρ_{-+} , with the matrix elements in Equation 24.

$$\begin{aligned}
\rho_{++} &= \rho_n + \rho_{mz} \\
\rho_{--} &= \rho_n - \rho_{mz} \\
\rho_{+-} &= \rho_{mx} - i\rho_{my} \\
\rho_{-+} &= \rho_{mx} + i\rho_{my} \\
\overline{\overline{\delta V(z)}} &= \frac{2\pi\hbar^2}{m_n} \begin{pmatrix} \rho_{++} & \rho_{+-} \\ \rho_{-+} & \rho_{--} \end{pmatrix}
\end{aligned}$$

Equation 25

The “+” (“-”) sign is for the neutron spin parallel (anti-parallel) to the applied field, so the positive magnetic scattering potential adds to the normally positive (repulsive) nuclear scattering potential. So, for example, ρ_{++} is the element of the scattering potential attributed to the scattering of an incident neutron with spin-up that does not change the orientation of the neutron spin with respect to the magnetic field. Likewise, ρ_{+-} is the element of the scattering potential attributed to the scattering of an incident neutron that changes its spin from up to down, and so on.

We now desire a solution to Schrödinger’s equation—one that takes into account the spin dependence of the scattering potential (Equation 25) and the spin dependence of the neutron wave function:

$$\begin{aligned}
\Psi(y) &= U_+ \begin{pmatrix} 1 \\ 0 \end{pmatrix} \Psi_+(y) + U_- \begin{pmatrix} 0 \\ 1 \end{pmatrix} \Psi_-(y) \\
\Psi_+(y) &= e^{ik_+y} \\
\Psi_-(y) &= e^{ik_-y}
\end{aligned}$$

Equation 26

The value of k_{\pm} is for the \perp -component (or y-component in Figure 10) of the wavevector for the different neutron spin states. The spin dependence of k_{\pm} arises from the energy dependence of the neutron spin in the magnetic field. In the field, the refractive index becomes spin-dependent (i.e., birefringent).

$$k_{\pm} = n_{\pm} k_0 = \sqrt{1 - \frac{4\pi(\rho_n \pm |\rho_m|)}{k_0^2}} k_0$$

Equation 27

The spin dependence of the incident neutron wave function contained in U_+ and U_- is determined by the polarization of the incident neutron beam.

Theoretical Example 4: Reflection of a polarized neutron beam from a magnetic film

In this example, we consider the reflection of a polarized neutron beam from a magnetic thin film in which the direction of magnetic induction is uniform. This example illustrates how the Parratt formalism developed earlier for unpolarized neutron reflection can be straightforwardly applied to a (saturated) magnetic thin film. Since the direction of magnetic induction is assumed to be parallel to the applied field, and the direction is uniform throughout the film (though the magnitude of the induction need not be uniform), the off-diagonal entries in the matrix of Equation 25 are zero. We now imagine performing an experiment involving two measurements of the sample reflectivity; first with spin-up neutrons (so $U_+ = 1$ and $U_- = 0$), and then later with spin-down neutrons (so $U_+ = 0$ and $U_- = 1$). A device called a spin-flipper (discussed later) flips the neutron spins from one state to the other. Equation 18 is easily generalized to account for the spin dependence of the neutron scattering potential [28].

$$\prod_{j=n-1}^0 \overline{M_j^{\pm}(\delta_j)} \begin{pmatrix} 1 + r_{\pm} \\ ik_0(1 - r_{\pm}) \end{pmatrix} = \begin{pmatrix} t_{\pm} \\ ik_{\pm n} t_{\pm} \end{pmatrix} \prod_{j=n-1}^0 e^{ik_{\pm n} \delta_j} = \begin{pmatrix} t_{\pm} \\ ik_{\pm n} t_{\pm} \end{pmatrix} e^{ik_{\pm n} \Delta}$$

$$\overline{M_j^{\pm}(\delta_j)} = \begin{pmatrix} \cos(k_{\pm j} \delta_j) & \frac{1}{k_{\pm j}} \sin(k_{\pm j} \delta_j) \\ -k_{\pm j} \sin(k_{\pm j} \delta_j) & \cos(k_{\pm j} \delta_j) \end{pmatrix}$$

Equation 28

In the previous example of a thin Fe layer on Si, we had considered the 20 nm thick layer to be a non-magnetic material with the nuclear scattering length density of Fe. Now, we consider the Fe to be fully saturated with magnetization parallel to the field as shown in Figure 10. The magnetic moment of an Fe atom is $\mu_{\text{Fe}} = 2.219 \mu_{\text{B}}$, so the neutron magnetic scattering length density is $\rho_m = N_{\text{Fe}} C \mu_{\text{Fe}} = 4.97 \times 10^{-6} \text{ \AA}^{-2}$ (Table 1). The scattering length density profiles for spin-up and spin-down neutrons are shown in Figure 11(a), as is the profile of the nuclear scattering length density [Figure 7(a)] alone for the sake of comparison. Depending upon whether the polarization of the neutron beam is parallel or anti-parallel to \mathbf{H} , ρ_m either adds or subtracts from ρ_n . The reflectivities for spin-up neutrons, R^{++} [for which the blue curve in Figure 11(a) is appropriate], and spin-down neutrons, R^{-} , [for which the red curve in Figure 11(a) is appropriate] are shown in Figure 11(b). The dotted curve in Figure 11(b) is the reflectivity of a non-magnetic film with the nuclear scattering length density of Fe (Figure 7), and would not be measured from a magnetized film of Fe with polarized neutron beams. In this example, the splitting between the R^{++} and R^{-} is a measure of the depth profile of the sample magnetization projected onto the applied field direction.

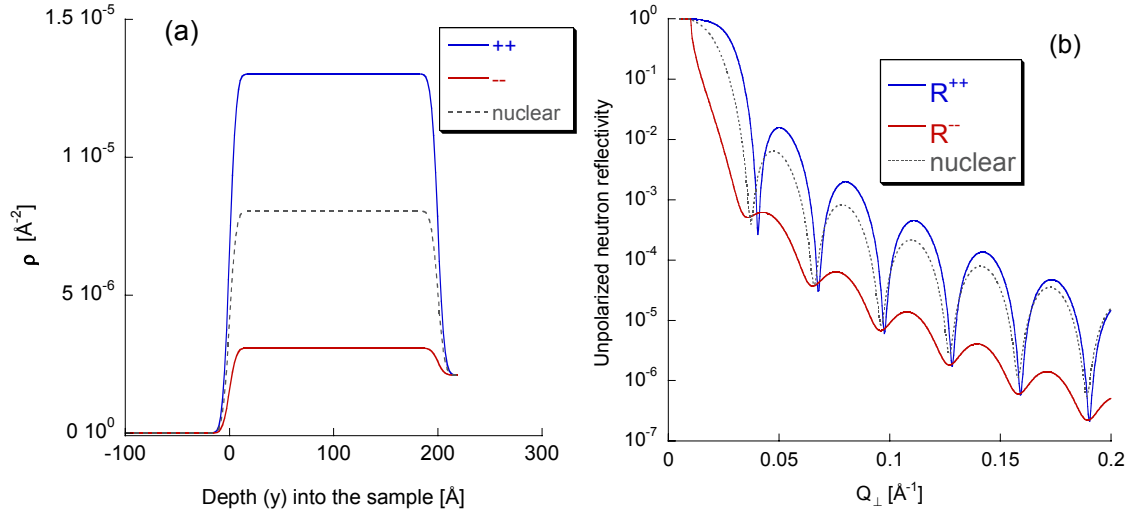


Figure 11 (a) Bifurcation of the magnetic scattering length densities profiles depending upon whether the neutron spin is parallel ($++$, blue curve) or anti-parallel ($--$, red curve) to the direction of the applied magnetic field. The dotted curve is the nuclear scattering length density profile. (b) The R^{++} and R^{--} reflectivity of the sample is shown as the blue and red curves, respectively. The dashed curve is the reflectivity curve for the case of a film with the nuclear scattering length density of Fe (and not magnetic).

Influence of imperfect polarization on reflectivity curves

In the preceding discussions, reflectivity curves were calculated for neutron beams that were assumed to contain only spin-up neutrons or spin-down neutrons. In other words the neutron beams were ideally polarized. In practice, the polarization of a neutron beam,

$$P = \frac{I_+ - I_-}{I_+ + I_-}$$

Equation 29

where I_+ and I_- represent the numbers or fractions of spin-up and spin-down neutrons, respectively, is not 100%. Typically, polarizations of order 90+ % are available for reflectometry experiments.

In order to produce a polarized neutron beam, polarization devices (discussed later) are inserted into the beam line before and sometimes after the sample. A

polarization device acts to suppress one spin state by either absorbing the undesired spin state (such a device is often called a polarization filter), or by spatially separating the two spin states through reflection from magnetized materials. Nearly all polarized neutron beams contain some fraction of undesired spins. Assume the desired spin state is the spin-up state. The contamination of the polarized neutron beam is attributed to spin-down neutrons. The polarization of the neutron beam approaches 100%, when the ratio, called the flipping ratio $F = \frac{I_+}{I_-}$, of desired neutron spins to undesired neutrons spins becomes large, in fact:

$$P = \frac{F - 1}{F + 1}$$

Equation 30

Since the transmission of a neutron beam through polarizing supermirrors is typically reduced by about 30% due to absorption of the beam by the Si substrates and Co in the coatings, experimentalists are best served by neutron beams with just enough polarization to obtain the data needed to solve a problem. Somewhat counter-intuitively, it may sometimes be more advantageous to study highly magnetic materials with higher neutron polarizations than used for materials that are only slightly magnetic. To understand this point, we assume that rather than using the perfectly polarized neutron beam in Theoretical Example 4, we use one having a flipping ratio of 10 (i.e., 1 in 10 neutrons has the wrong spin state, $P = 82\%$). The as-measured spin-up reflectivity will be composed of $0.9R^{++}$ [Figure 11(b)] and $0.1R^{--}$ [Figure 11(b)], which hardly changes the result (compare the solid and dashed blue curves in Figure 12). However, since the spin-up reflectivity is so much larger than the spin-down reflectivity (in this example),

the as-measured spin-down reflectivity will consist of $0.1R^{++}$ (a large source of contamination) and $0.9R^{-}$ (compare the solid and dashed red curves in Figure 12). Failure to account for imperfection of the polarized neutron beam would lead one to mistakenly conclude that the Fe film was less magnetic than it actually is. Provided the polarization of the neutron instrument is known, the true reflectivity curves can be obtained from reflectivity measurements using neutron beams with less than 100% polarization [44].

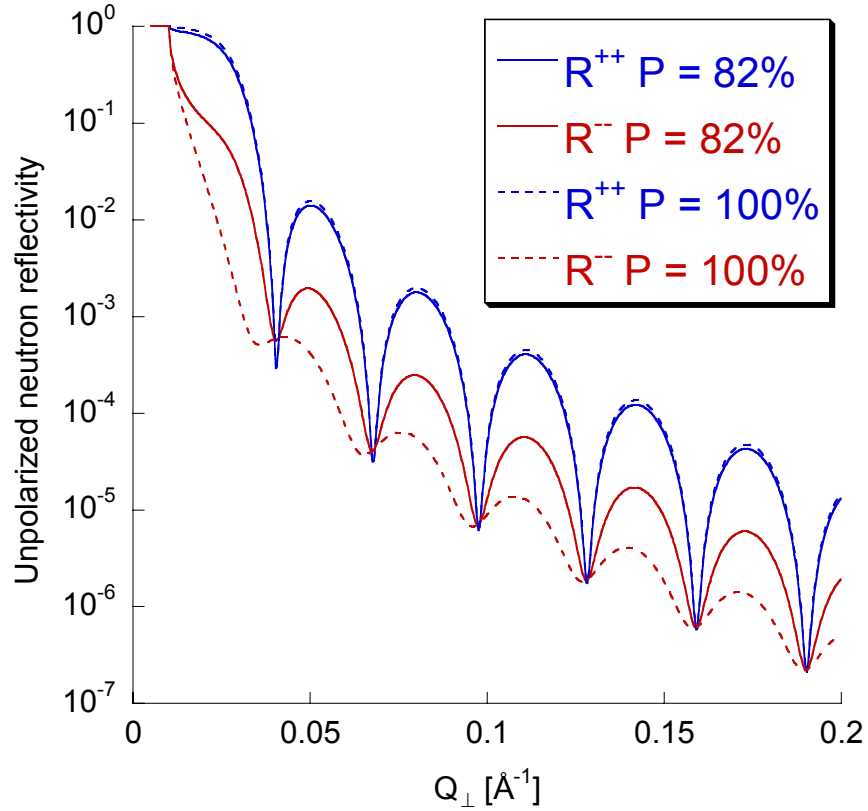


Figure 12 Reflectivity curves calculated for an ideally polarized neutron beam (dashed curves) are compared to those calculated for a neutron beam with 82% polarization (solid curves). The large spin-up reflectivity (blue curve) is hardly affected by a poorly polarized neutron beam. On the other hand, the contamination in the poorly polarized neutron beam greatly perturbs the much weaker spin-down reflectivity (red curve), because the contamination when measuring spin-down is spin-up and the spin-up reflectivity is much larger than the spin-down reflectivity.

In contrast, for the case of a material that is only weakly magnetic, e.g., a magnetic semiconductor with magnetization ~ 30 emu/cm³, R^{++} and R^{-} will be little

different, so the contamination posed by having $1/10^{\text{th}}$ of the wrong spin state in the as-measured reflectivity might be negligible. In this situation, a relatively poorly polarized neutron beam might be preferred over a highly polarized neutron beam, especially if the intensity of the poorly polarized neutron beam is larger than that of the highly polarized beam.

“Vector” magnetometry with polarized neutron beams

In the previous discussions, the neutron spin and magnetic induction have been treated as if they were always parallel (or anti-parallel) to the neutron spin direction. However, this constraint does not always exist. For example, a material with strong uniaxial anisotropy could be oriented with \mathbf{M} at an angle of ϕ to \mathbf{H} (Figure 13). Classically, when a neutron whose spin enters a region in which its spin is not parallel to the induction, the neutron spin begins to precess. Depending upon the time the neutron spends in this region and the strength of the induction, the neutron spin may flip 180° —the intentional rotation of a neutron spin by 180° is the basis for operation of a so called Mezei spin-flipper [45]. Likewise, the magnetization of a material can rotate the spin of a neutron such that a beam with one polarization scatters from the sample with diminished polarization, i.e., some of the spin-up neutrons may be flipped to spin-down—so-called spin-flip scattering. In this situation, the scattering potential, $\overline{\delta V(z)}$, is not simply birefringent: in other words the off-diagonal elements in Equation 25 are non-zero.

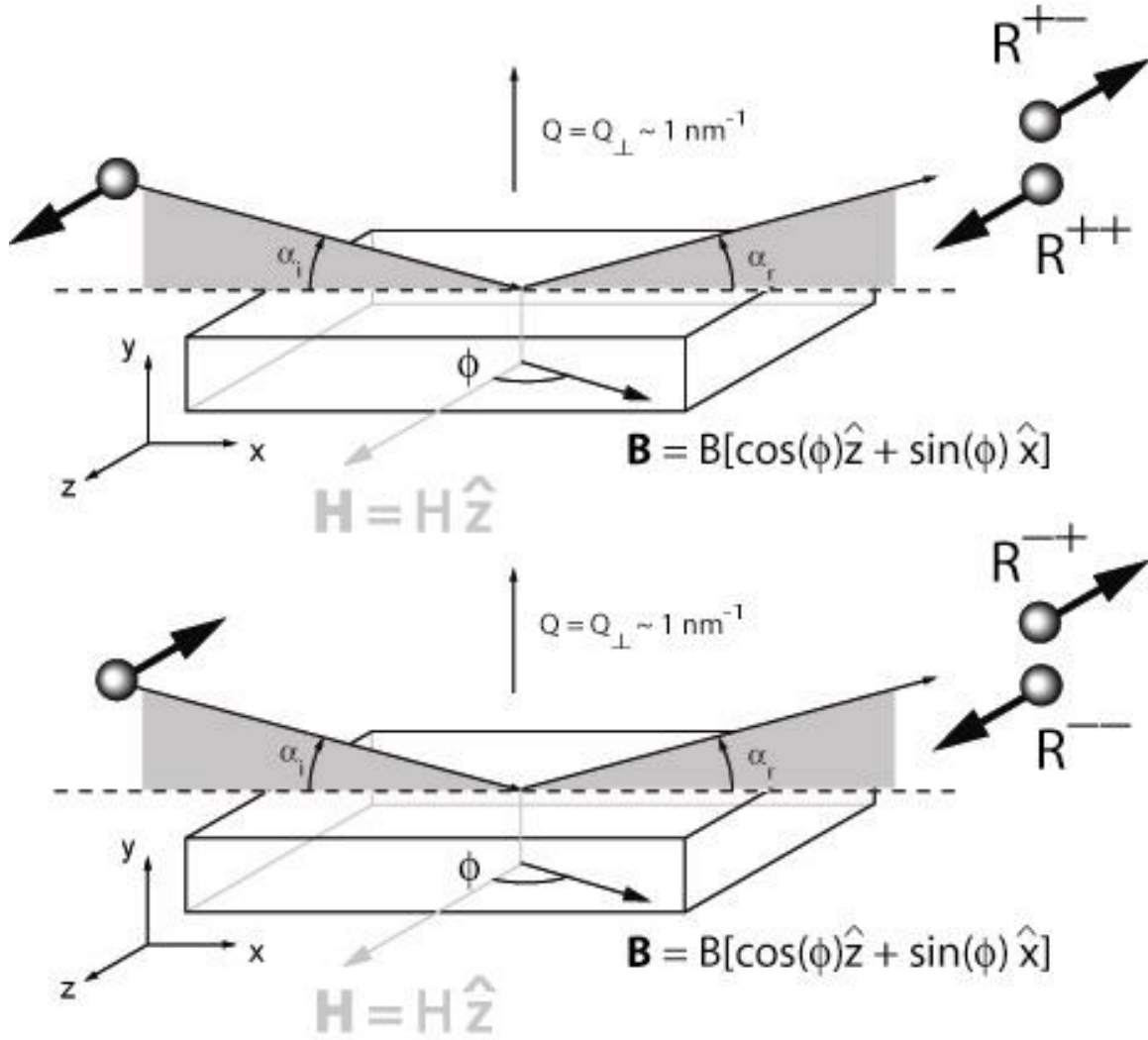


Figure 13 Schematic diagram showing (top) a spin-up polarized neutron beam reflecting from a sample with magnetic induction at an angle of ϕ from the applied field. The reflected beam has two components—the (R^{++}) non-spin-flip and (R^{+-}) reflectivities. (lower) The case is shown when the polarization of the incident neutron beam is spin-down.

For the geometry of the neutron reflectometry experiment shown in Figure 13, a further simplification to the off-diagonal elements of Equation 22 can be made. One of Maxwell's equations (specifically $\nabla \cdot \mathbf{B} = 0$ [46]) requires the out-of-plane component of \mathbf{B} across the interface to be continuous, so the component of \mathbf{B} parallel to \mathbf{Q} or \hat{y} will not yield a change in contrast across the interface; therefore, $\rho_{+-} = \rho_{-+} = \rho_{mx} \equiv \rho_{SF}$. The

important consequence of the dipolar interaction between neutron and magnetic moments is that magnetic scattering of the neutron is only produced by the component of the magnetization perpendicular to wavevector transfer. In the case of a (specular) neutron reflection experiment (Figure 13), this requirement means that spin-dependence of the neutron reflectivity arises from the components of the sample magnetization projected onto the reflection (or sample) plane.

Theoretical Example 5: Reflection from a magnetic medium in which the direction of magnetic induction is perpendicular to the applied field and parallel to the plane of the sample

We now calculate the scattering from the Fe film for the case when the Fe magnetization is rotated through an angle ϕ about the surface normal from the applied field direction (see Figure 13). In order to account for the possibility that the sample changes the spin state of a neutron, a generalization of Equation 28 to include spin-flip scattering, is required [19, 20, 28].

$$\prod_{j=n-1}^0 \overline{\overline{A_j}} \begin{pmatrix} I_+ + r_+ \\ I_- + r_- \\ ik_0(I_+ - r_+) \\ ik_0(I_- - r_-) \end{pmatrix} = \begin{pmatrix} t_+ \\ t_- \\ ik_n t_+ \\ ik_n t_- \end{pmatrix}$$

Equation 31

where the elements of $\overline{\overline{A_j}}$ are:

$$\begin{aligned}
A_{11} &= 2\eta[\gamma_3 \cosh(S_+ \delta_j) - \gamma_1 \cosh(S_- \delta_j)] \\
A_{21} &= 2\eta[\gamma_1 \gamma_3 \cosh(S_+ \delta_j) - \gamma_1 \gamma_3 \cosh(S_- \delta_j)] \\
A_{31} &= 2\eta[S_+ \gamma_3 \cosh(S_+ \delta_j) - S_- \gamma_1 \cosh(S_- \delta_j)] \\
A_{41} &= 2\eta[S_+ \gamma_1 \gamma_3 \cosh(S_+ \delta_j) - S_- \gamma_1 \gamma_3 \cosh(S_- \delta_j)] \\
A_{12} &= 2\eta[-\cosh(S_+ \delta_j) + \cosh(S_- \delta_j)] \\
A_{22} &= 2\eta[-\gamma_1 \cosh(S_+ \delta_j) + \gamma_3 \cosh(S_- \delta_j)] \\
A_{32} &= 2\eta[-S_+ \sinh(S_+ \delta_j) + S_- \sinh(S_- \delta_j)] \\
A_{42} &= 2\eta[-S_+ \gamma_1 \sinh(S_+ \delta_j) + S_- \gamma_3 \sinh(S_- \delta_j)] \\
A_{13} &= 2\eta\left[\frac{\gamma_3}{S_+} \sinh(S_+ \delta_j) - \frac{\gamma_1}{S_-} \sinh(S_- \delta_j)\right] \\
A_{23} &= 2\eta\left[\frac{\gamma_1 \gamma_3}{S_+} \sinh(S_+ \delta_j) - \frac{\gamma_1 \gamma_3}{S_-} \sinh(S_- \delta_j)\right] \\
A_{33} &= A_{11} \\
A_{43} &= A_{21} \\
A_{14} &= 2\eta\left[-\frac{1}{S_+} \sinh(S_+ \delta_j) + \frac{1}{S_-} \sinh(S_- \delta_j)\right] \\
A_{24} &= 2\eta\left[-\frac{\gamma_1}{S_+} \sinh(S_+ \delta_j) + \frac{\gamma_3}{S_-} \sinh(S_- \delta_j)\right] \\
A_{34} &= A_{12} \\
A_{44} &= A_{22}
\end{aligned}$$

and

$$\begin{aligned}
S_{\pm} &= in_{\pm} k_0 \\
\gamma_1 &= \frac{|\boldsymbol{\rho}_m| - \rho_{mz} + \rho_{mx} + i\rho_{my}}{|\boldsymbol{\rho}_m| + \rho_{mz} + \rho_{mx} - i\rho_{my}} \\
\gamma_3 &= \frac{|\boldsymbol{\rho}_m| + \rho_{mz} - \rho_{mx} - i\rho_{my}}{|\boldsymbol{\rho}_m| - \rho_{mz} - \rho_{mx} + i\rho_{my}} \\
2\eta &= \frac{1}{\gamma_3 - \gamma_1}
\end{aligned}$$

Equation 32

To calculate the four neutron spin reflectivities, R^{++} , R^{+-} , R^{-+} and R^{--} , the nuclear (ρ_n) and magnetic (ρ_m , a vector) scattering length density profiles for the sample are computed. Examples of these profiles are shown in Figure 14, where $\rho_m = C'm_{Fe}(\cos(\phi)\hat{z} + \sin(\phi)\hat{x})$.

Next, we assume the sample is illuminated by a spin-up polarized neutron beam, so $I_+ = 1$ and $I_- = 0$, and use Equation 31 to compute R^{++} and R^{+-} ($\equiv |r_+|^2$ and $|r_-|^2$; the probabilities that a neutron with up-spin is reflected with up-spin or down-spin, respectively). Then, the calculation is repeated for a spin-down polarized neutron beam ($I_+ = 0$ and $I_- = 1$) to obtain R^{-+} and R^{--} ($\equiv |r_+|^2$ and $|r_-|^2$; the probabilities that a neutron with down-spin is reflected with up-spin or down-spin, respectively). The result is plotted in Figure 15, where $R^{SF} = \frac{R^{+-} + R^{-+}}{2}$, for the cases (a) $\phi = 90^\circ$ and (b) $\phi = 45^\circ$. For the case $\phi = 90^\circ$, the net magnetization of the sample along the applied field is zero, so there is no splitting between the two non-spin-flip cross-sections (and a strong signal in the spin-flip cross-section). On the other hand, for $\phi = 45^\circ$, the net magnetization of the sample along the applied field is non-zero, so splitting between R^{++} and R^{--} is observed along with a lower magnitude for R^{SF} .

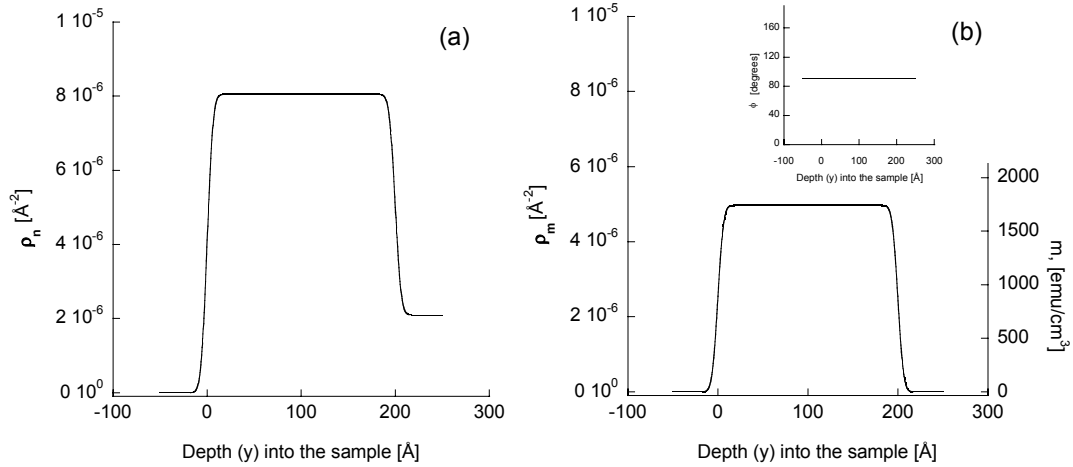


Figure 14 Plot of the nuclear (a) and magnetic (b) scattering length densities profiles. Inset: The angle about the surface normal of the magnetization from the applied field is 90° .

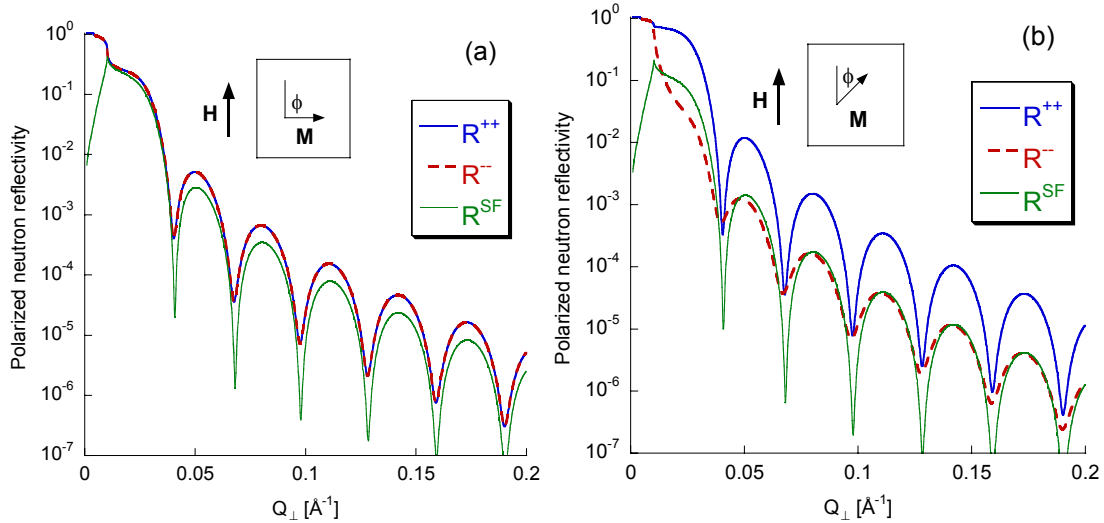


Figure 15 Polarized neutron reflectivity curves for the Fe/Si sample (inset) with Fe magnetization rotated (a) $\phi = 90^\circ$ and (b) $\phi = 45^\circ$ from the applied field and polarization axis of the neutron beam.

A qualitative (and intuitive) understanding of “vector” magnetometry

An intuitive understanding of spin-dependent reflection is most easily obtained by considering the kinematical equations that describe reflection, which so far has been treated using the exact dynamical formalism. By kinematical, we mean that effects such as the evanescence of the wave function below the critical edge, which greatly perturb the wave function inside the sample, are negligible. These effects are neglected when the

transmitted wave function in Equation 1 is replaced with the incident wave function. Within the Born approximation, the spin-dependent reflection amplitudes for the scattering geometry shown in Figure 13 are [28]:

$$r_{BA}^{\pm\pm}(Q_{\perp}) \propto \int_0^{\Lambda} [\rho_n(y) \pm \rho_m(y) \cos \phi(y)] e^{iQ_{\perp}y} dy$$

$$r_{BA}^{\pm\mp}(Q_{\perp}) \propto \int_0^{\Lambda} \rho_m(y) \sin \phi(y) e^{iQ_{\perp}y} dy$$

Equation 33

The reflectivities for the non-spin-flip processes are a sum of the squares of the nuclear and magnetic structure factors (given in Equation 33) plus a term resulting from the interference between nuclear and magnetic scattering. The interference term is observed with polarized neutron beams. The spin-flip reflectivity is purely magnetic in origin. Note for the special case where $\phi = 90^\circ$, as can be realized for samples with uniaxial anisotropy, the non-spin-flip reflectivities are purely nuclear (or chemical) in origin. In this special case, the magnetic and chemical profiles of the sample can be isolated from one another. By measuring both the non-spin-flip and spin-flip reflectivities as a function of Q_{\perp} , Equation 33 suggests that the variation of the magnetization vector, in amplitude and direction in the sample plane, can be obtained as a function of depth. This capability is an important reason why polarized neutron reflectometry complements conventional vector magnetometry, which is a technique that measures the net (or average) magnetization vector of a sample.

A second important example of the power of polarized neutron reflectometry is for detecting and isolating magnetism of weakly magnetic materials from that of strongly magnetic materials through analysis of the Fourier components in the reflectivity curves.

Situations in which this capability may be valuable include detecting coerced or proximal magnetism in materials that are normally non-magnetic in the bulk, e.g., Pd that becomes magnetic in proximity to Fe [47]. Polarized neutron reflectometry is also valuable in studies of weakly ferromagnetic thin films, e.g., (Ga, Mn)As [48], grown on substrates that contribute a strong diamagnetic or paramagnetic background to the signal measured in a conventional magnetometer.

For studies of films whose magnetization does not change with depth, but instead the magnetization changes along the film plane, as realized for example in films composed of magnetic domains, the sizes of the magnetic domains in relation to the coherence of the neutron beam (which is typically microns in size) determine whether off-specular or diffuse scattering of the neutron beam, in addition to specular scattering, is observed. Diffuse scattering can be observed when the lateral variation of the magnetization is small in comparison to the coherence of the neutron beam. On the other hand, if the domains are much bigger than the coherence of the beam, then information about the magnetism of the sample will be observed in the specular reflectivity.

Consider reflection of a neutron beam from a single domain with uniform magnetization and having a lateral size that is large in comparison to the coherent region of the neutron beam. In this example, the reflectivity of the domain is straightforwardly calculated using Equation 33.

$$R_{BA}^{\pm\pm}(Q_{\perp}) \propto (\rho_n^2 + \rho_m^2 \cos^2 \phi \pm 2\rho_n \rho_m \cos \phi)(1 - \cos Q_{\perp} \Delta)$$

$$R_{BA}^{SF}(Q_{\perp}) = R_{BA}^{\pm\mp} \propto \rho_m^2 \sin^2 \phi (1 - \cos Q_{\perp} \Delta)$$

Equation 34

Using the relation between ρ_m and \mathbf{m} provided by Equation 23 we resolve \mathbf{m} into components parallel and perpendicular to the applied field such that $m_{\parallel} \propto \rho_m \cos \phi$ and $m_{\perp} \propto \rho_m \sin \phi$, respectively. Then, using Equation 34 we obtain a physical meaning for the difference (or splitting) between the non-spin-flip reflectivities, Δ_{NSF} , and R^{SF} .

$$\begin{aligned}\Delta_{NSF}(Q_{\perp}) &= R_{BA}^{++}(Q_{\perp}) - R_{BA}^{--}(Q_{\perp}) \propto m_{\parallel}(1 - \cos Q_{\perp} \Delta) \\ R_{BA}^{SF}(Q_{\perp}) &\propto m_{\perp}^2(1 - \cos Q_{\perp} \Delta)\end{aligned}$$

Equation 35

That is, the splitting between the non-spin-flip reflectivities is proportional to the projection of the domain magnetization onto the applied field, and the spin-flip reflectivity is proportional to the *square* of the domain magnetization perpendicular to the applied field.

Owing to the fact that neutron scattering is a statistical probe of a sample's potentially non-uniform distribution of magnetization, rather than a scanning probe of the magnetization at the atomic scale (which could be non-representative), there is an important complication to the interpretation of the neutron scattering results. The complication stems from, as discussed earlier, whether the non-uniformity of magnetization varies on a length scale that is small or large compared to the coherent region [49] of the neutron beam. If the fluctuations of magnetization are small compared to the coherent region of the neutron beam, then the reflectivity is obtained from the reflection amplitude of an ensemble of domains. Depending upon the details of the fluctuations, the scattering may consist of specular and off-specular (or diffuse scattering) components. On the other hand, if the fluctuations occur on a length scale larger than the

coherent region of the neutron beam, then the reflectivity is the sum of the reflectivity of each component and the reflectivity is specular.

It is the second case, one composed of domains that are large in comparison to the coherent region of the neutron beam that is easiest to treat. In this case, $\Delta_{NSF} \propto \langle m_{\parallel} \rangle$ and $R_{BA}^{SF} \propto \langle m_{\perp}^2 \rangle$, where $\langle \rangle$ denotes the average value of the ensemble. The first term, Δ_{NSF} , provides a measure of the Fourier components of the net sample magnetization projected onto the applied field and is similar to the net magnetization of the sample as measured by a magnetometer (in a sense a magnetometer measures Δ_{NSF} corresponding to $Q_{\perp} = 0$). The second term contains qualitatively different information than that which can be measured by a vector magnetometer. Specifically, R^{SF} is a measure of the *mean square deviation* of the magnetization away from the applied field. For the examples of magnetic domain distributions shown in Figure 16, the net sample magnetization in any direction is zero. In this situation, a vector magnetometer would measure the zero-vector, yet, provided the domains are large in comparison to the coherence of the neutron beam, the mean square deviation of the magnetization away from the applied field is a (non-zero) quantity obtained from polarized neutron scattering as R^{SF} [50]. Note, $f_1, f_{\perp} = f_2 + f_4$, and f_3 [Figure 16(left)] and ϕ [Figure 16(right)] can be chosen such that $\langle m_{\perp}^2 \rangle$ is the same for both models, so polarized neutron reflectometry cannot distinguish between these two particular domain distributions, nevertheless the technique does provide information about magnetic properties, e.g., anisotropy [51] that are related to $\langle m_{\perp}^2 \rangle$.

Extreme cases of domain distributions—ones that yield no net magnetization along the applied field (as realized when the magnitude of the applied field is equal to the

coercive field) are shown in Figure 17, along with the features of the *specular* reflectivity curves that are unique to the particular domain structure. In the first case, the non-spin-flip reflectivities would be superimposed with amplitudes that contain nuclear and magnetic contributions [the reflectivity curve would not be the same as the purely nuclear case shown in Figure 5(b)]. The period of the non-spin-flip reflectivities would be $2\pi/\Delta$, and the spin-flip reflectivity would be zero. In the second case, the non-spin-flip reflectivities would be purely nuclear in origin, and the spin-flip reflectivity would be non-zero with a period equal to the $2\pi/\Delta$. In the third case, the two non-spin-flip reflectivities would be different and have a period of $2\pi/(\Delta/2)$. The spin-flip reflectivity would be zero for this case. For the last case, the non-spin-flip reflectivities would be purely nuclear in origin (as in the second case) and the spin-flip reflectivity would be non-zero with a period of $2\pi/(\Delta/2)$.

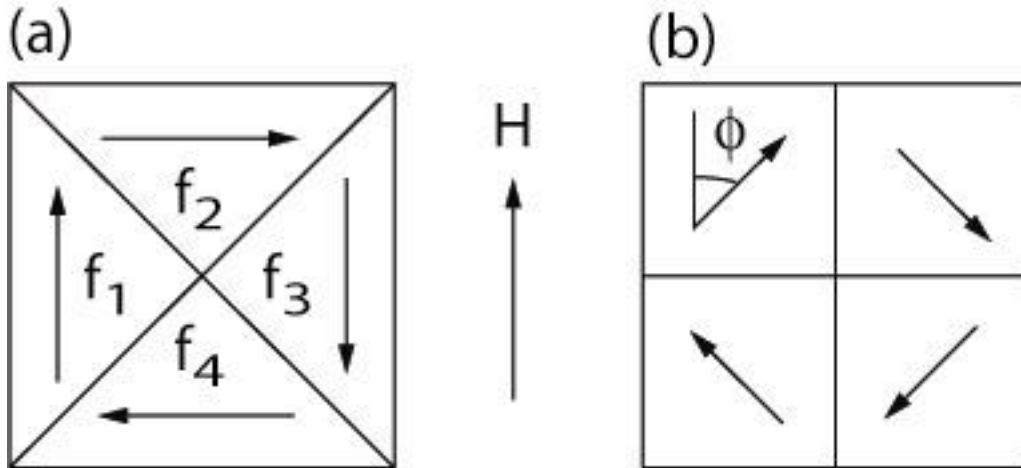


Figure 16 Examples of magnetic domains with magnetization directed as shown by the arrows. (a) In this closure domain model f_i represents the area fraction of the i -th domain, and the magnetization of the material reverses by changing the value of f_i . (b) In this model, the area fractions of the domains are equal and the magnetization of the material reverses as the angle between the magnetization and the applied field direction changes from 0 to 180° .

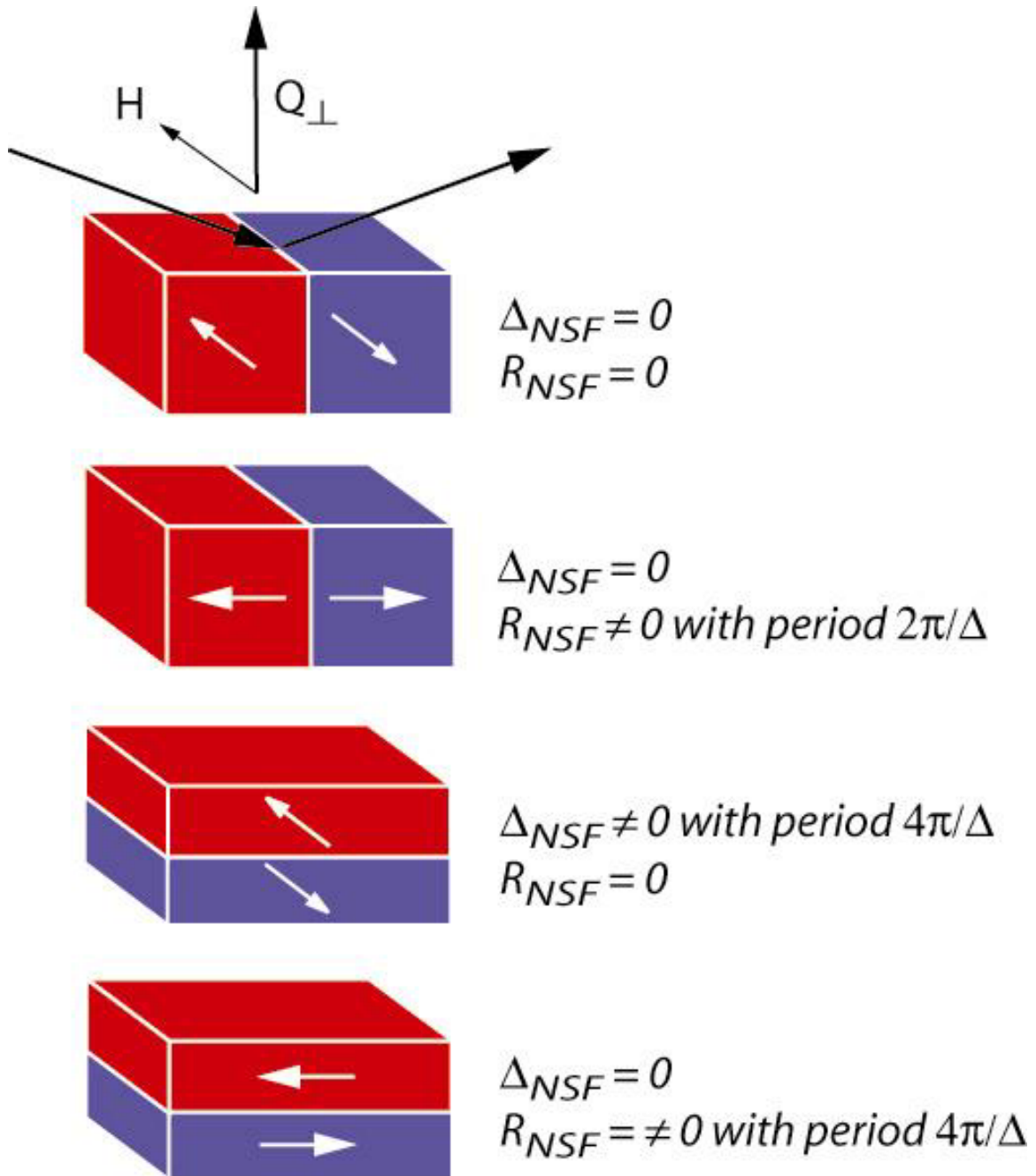


Figure 17 Four examples of a magnetic material whose net magnetizations along the applied field, H , (or any direction) are all zero (the volume fractions of red and blue domains are equal, and the domain sizes are assumed to be large in comparison to the coherent region of the neutron beam). The neutron scattering signature in the specular reflectivities from each model is unique.

Description of a polarized neutron reflectometer

Three essential requirements for any polarized neutron reflectometer are:

- (1) an a priori knowledge of the polarization of the neutron beam illuminating the sample;
- (2) the capability to measure the intensity and polarization of the neutron beam reflected by a sample;
- (3) and the ability to make these measurements as a function of wavevector transfer parallel and perpendicular to the sample surface.

The first feature requires a device to polarize the neutron beam (a polarizer) and to flip the neutron beam polarization (a spin-flipper). The second feature requires a neutron detector and a device(s) to flip and measure the neutron beam polarization after reflection from the sample. Finally, wavevector transfer is obtained from measurements of the neutron wavelength and the angle through which the neutron has been scattered. Angles are measured using slits to define the path of the neutron beam that is allowed to strike a neutron detector, or by using a position sensitive neutron detector.

Preparation of the cold neutron beam for a reflectometer at a pulsed neutron source

We briefly describe a reflectometer/diffractometer (Figure 18) designed for studies of magnetic materials at a source of pulsed neutrons. Sources of pulsed neutrons (e.g. LANSCE at Los Alamos National Laboratory) provide neutron pulses that are typically very short, on the order of 100-300 μs , and periodic—with periods ranging between $\tau \sim 10 - 100 \text{ ms}$.

For neutron scattering measurements in the small-Q or large d-spacing regimes (neutron scattering measurements of magnetic materials are often in these regimes), neutrons with very low energies (long wavelengths) are desirable because the sine of the

critical angle, $\sin(\theta_c) = \frac{\lambda Q_c}{4\pi}$, is proportional to neutron wavelength. Since the relative influence of systematic or alignment errors decreases with increasing angle, Q_\perp can be more accurately measured with long wavelength neutrons than with short wavelength neutrons. Also, by measuring relevant values of Q_\perp at large angles, we can take advantage of the intrinsically large and divergent neutron beam (in comparison to X-ray beams which can be very small and highly collimated). Even though the wavelength of a cold neutron beam might be an order of magnitude larger than X-ray beams, the specular reflectivity is still measured through angles on order of 1° (as in X-ray reflectometry) because Q_c probed with neutrons is typically an order of magnitude smaller than that for X-rays. Cold neutron beams are obtained by viewing the neutron source through a material like $l\text{-H}_2$ that absorbs neutron energy through collisions with hydrogen atoms. This so-called moderator changes the energy of the neutron beam from MeV to meV energies. The spectrum of a cold neutron beam is shown in Figure 19.

In order to preserve the intensity of a neutron beam, the beam may travel through a glass pipe, called a neutron guide, whose inside surfaces are coated with a highly reflecting material, e.g., ^{58}Ni . Neutrons striking the sides of the guide at sufficiently small wavevector transfer, i.e., $Q_\perp < Q_c$, ($= 0.026 \text{ \AA}^{-1}$ for ^{58}Ni) are reflected and stay confined within the guide. The angular divergence of neutron trajectories emanating from the end of the guide is $2\alpha_c = \frac{2\lambda Q_c}{4\pi}$; thus, neutrons with trajectories within $\pm\alpha_c$ of the centerline of the neutron guide can, in principle, interact with a sample. Note, the divergence of the neutron beam from a guide increases linearly with wavelength.

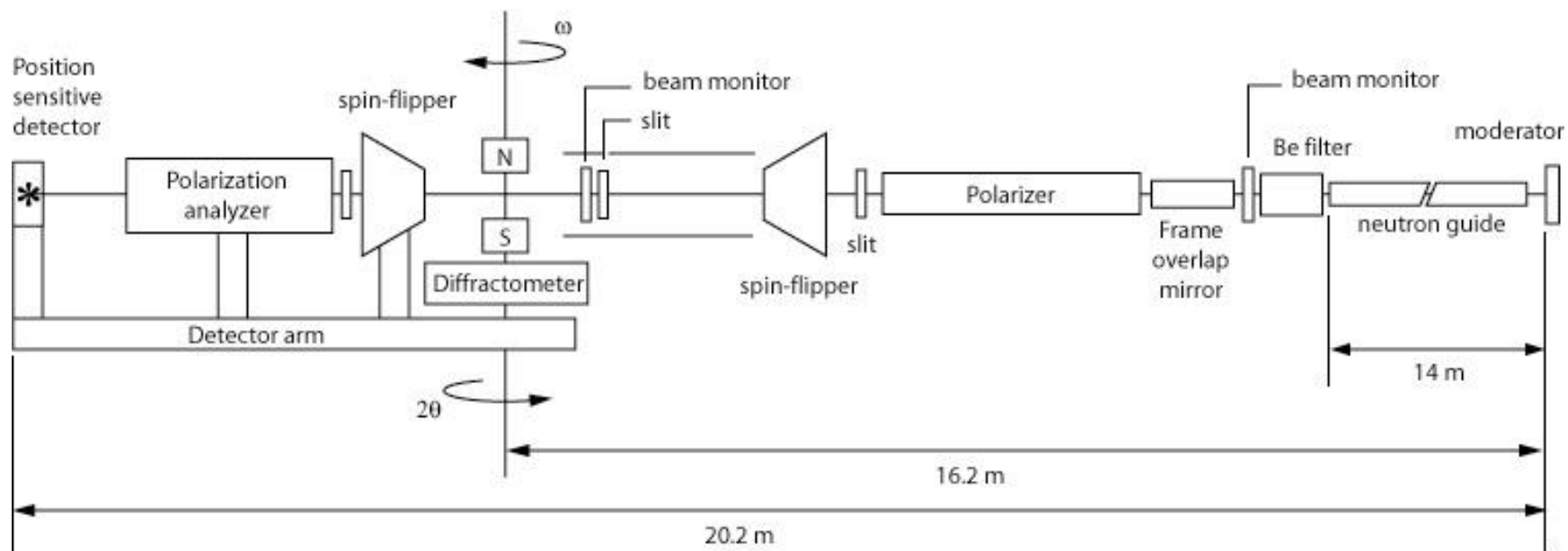


Figure 18 Schematic diagram of a polarized neutron reflectometer/diffractometer at a pulsed neutron source (LANSCE).

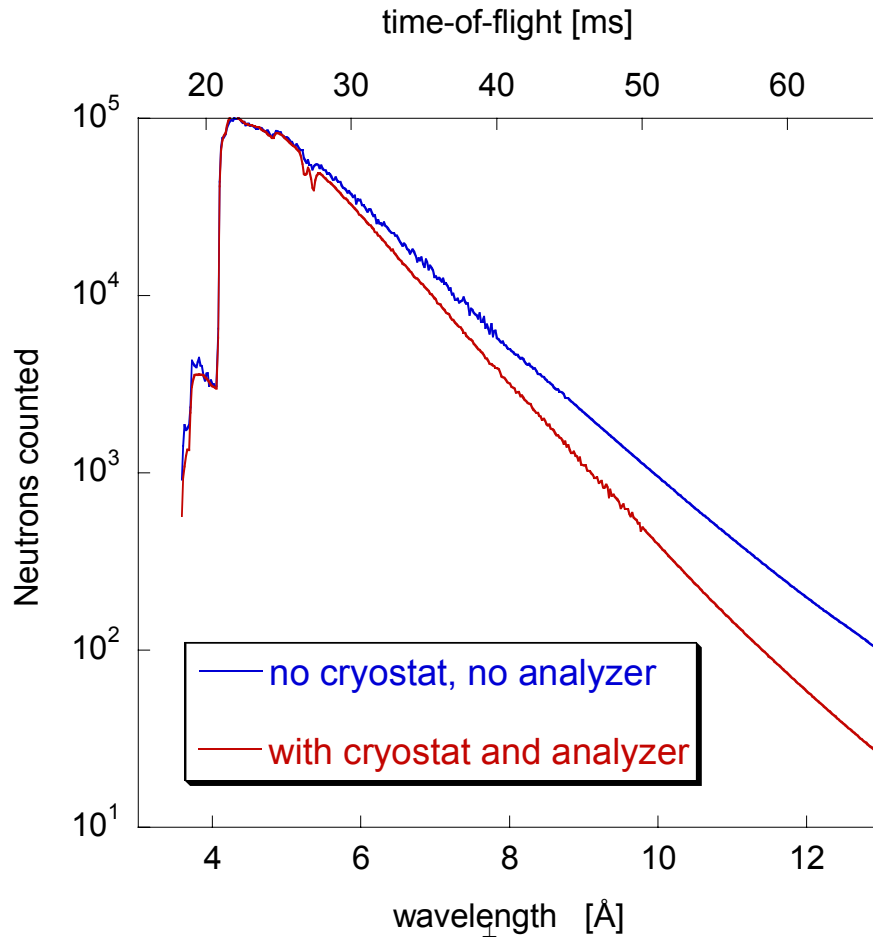


Figure 19 Neutron spectrum measured from a coupled I-H₂ moderator (blue curve) without a cryostat and without polarization analysis and (red curve) with a cryostat and polarization analyzer inserted. The spectrum is plotted for neutron events counted in wavelength increments of constant size. The Be filter is mostly transparent above ~ 4 Å. The decay of the spectrum with wavelength is reminiscent of that from a black-body radiator.

While the moderator greatly reduces the energy of the neutron beam, there still remain some highly energetic neutrons that may interact with components of the instrument and consequently lose energy through the interaction. Thermalization of energetic neutrons is an important source of instrumental background. In order to suppress this source of background, a filter is required, i.e., a device that is nearly opaque to high energy neutrons and transparent to low energy neutrons. One such device, called

a Be filter, consists of a cryogenically cooled block of polycrystalline Be through which the neutron beam passes. Since, the lowest order Bragg reflection of Be corresponds to a d-spacing of approximately 4 Å, the portion of the neutron beam with $\lambda < 4$ Å will be scattered by the Be block thereby reducing the high energy content of the transmitted neutron beam. The spectrum shown in Figure 19 was measured after the neutron beam passed through a Be filter (Figure 18).

A second source of instrumental background arises from very slow (i.e., very long wavelength) neutrons that require more than one period of the neutron source to reach the detector. As mentioned earlier, neutron wavelength is measured at pulsed neutron sources by recording the time-of-flight of a neutron to travel a known distance. The velocity of a neutron is the slope of its trajectory in Figure 20. Ambiguity in the time-of-flight exists, since the neutron detector can not distinguished between a neutron whose time-of-flight is t (e.g., t corresponding to a neutron with $\lambda = 9$ Å, Figure 20, solid line) compared to one with $t + \tau$ (e.g., t corresponding to a neutron with $\lambda = 18$ Å, Figure 20, dashed line). At first glance, the contamination of the neutron beam by very long wavelength neutrons might seem unimportant because there are few of these neutrons. However, their probability of reflection from a sample is very great (because Q_{\perp} is so small when λ is so large). In fact, it is a happy coincidence that the decay of the spectrum with wavelength is approximately counteracted by the approximate λ^4 increase (Fresnel) of the reflectivity curve, so the measured intensity of the sample reflectivity is reasonably comparable (within an order of magnitude or so) for all wavelengths.

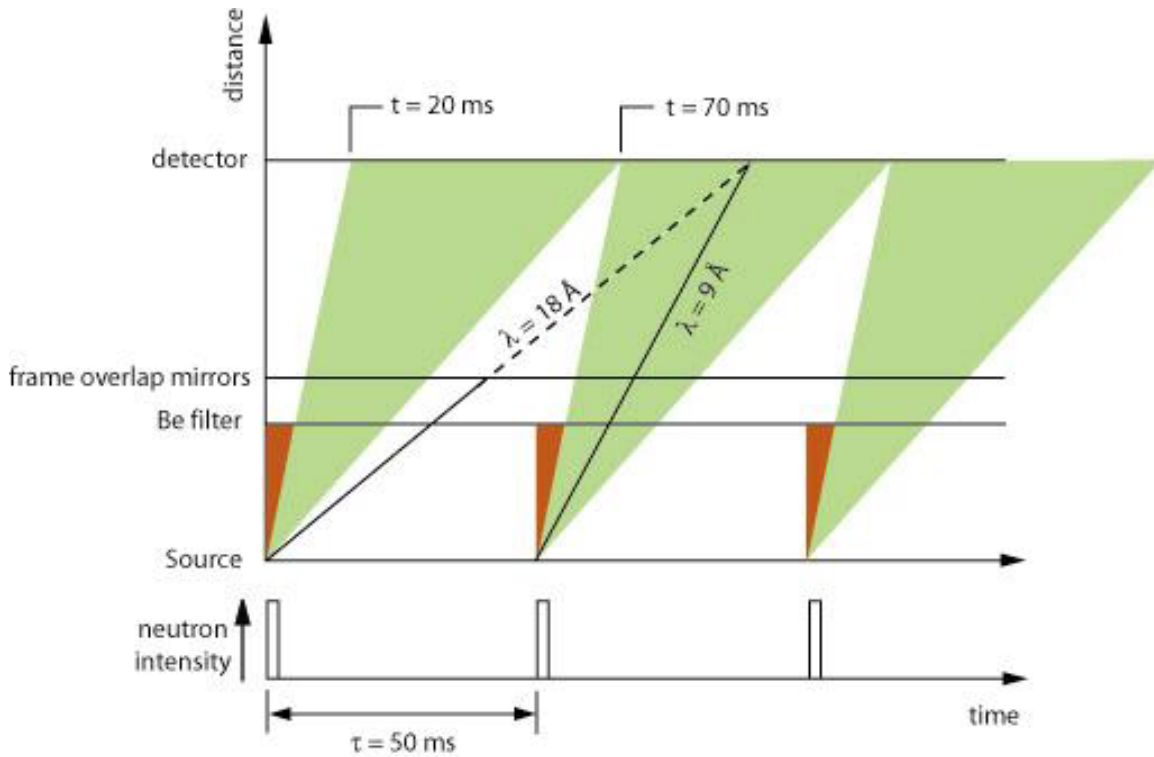


Figure 20 Distance vs. time graph of trajectories corresponding to neutrons with different velocities (or wavelengths). Since a detector can only distinguish times-of-flight within one source period, neutrons with $\lambda = 9 \text{ \AA}$ and 18 \AA are assigned the same times-of-flight; therefore, their wavelengths can not be distinguished. Fortunately, mirrors, called frame overlap mirrors, can be placed in the neutron beam line to reflect the $\lambda = 18 \text{ \AA}$ neutrons out of the beam while allowing the $\lambda = 9 \text{ \AA}$ neutrons to pass through (to the detector).

Fortunately, the possibility of an elevated instrumental background due to very long wavelength (i.e., the frame overlap) neutrons is easily addressed by placing a mirror in the neutron beam at a large angle such that neutrons with very long wavelengths (for example greater than 14 \AA) are reflected out of the neutron beam, while the remaining neutrons are transmitted through the mirror. In the case of the instrument discussed here, so-called $3\theta_c$ (unpolarizing) supermirrors, consisting of a multilayer metallic coating whose critical edge is three times larger than that of Ni are deposited onto relatively transparent Si substrates. Extension of the critical edge is accomplished by arranging a variation in the thickness of the layers in the mirror such that a series of Bragg reflections are produced starting at Q_c (for a thick Fe film) out to large wavevector transfer [52, 53].

After traveling through the neutron guide, Be filter and frame overlap mirrors, an intense beam of unpolarized neutrons with large cross-section (for the instrument whose schematic is shown in Figure 18, the cross-section is 6 cm by 6 cm) and having a large wavelength band from 4 to 13 Å, is ready for polarization.

Polarization of cold neutron beams

Production of cold neutron beams with polarization in excess of 90% is primarily accomplished using polarizing supermirrors. Much like the supermirror discussed previously, a polarizing supermirror consists of hundreds of layers of alternating non-magnetic and magnetic materials [52, 53]. The key to a good polarizing mirror is to maximize the magnitude of the spin-up potential, while matching the spin-down potential to that of the substrate, typically Si. The spin-dependent reflectivity for such a polarizing supermirror is shown in Figure 21(a). Spin-up neutrons are reflected from the mirror, while spin-down neutrons are transmitted through it. In the case of the instrument illustrated in Figure 18, the transmitted spin-down neutron beam is used for experiments, and the spin-up beam is discarded (or absorbed). The polarization of the transmitted neutron beam is shown in Figure 21(b) [54, 55]. An important reason for using the transmitted polarized neutron beam is that the same beam line can be used for experiments that use polarized and unpolarized neutrons (e.g., an unpolarized neutron beam is obtained by simply translating the polarizer out of the beam line).

The range in wavelength, $\Delta\lambda$, and angular divergence, $\Delta\theta$, for which the neutron beam is well-polarized is determined by the locations of the critical edge of the spin-down neutrons (below this edge the transmitted neutron beam has little intensity) and the critical edge for spin-up neutrons (above this edge both spin-down and spin-up neutrons

are transmitted through the polarizer). The range in ΔQ_{\perp} over which the neutron beam is well-polarized is 0.055 \AA^{-1} (Figure 21)—a typical range for a supermirror. For an instrument using monochromatic radiation $\Delta\lambda/\lambda_0 = \delta\lambda/\lambda_0 \sim 2\%$ (rms), so the contribution to $\Delta Q/Q$ from the range in neutron wavelength is correspondingly small. Consequently, monochromatic neutron beams with relatively large divergence, $\Delta\theta$, can be easily polarized. For example, if $\lambda_0 = 5 \text{ \AA}$, a neutron beam with divergence of order $\Delta\theta = 1.25^\circ$ can be polarized. However, for instruments which use the time-of-flight technique and therefore use a large wavelength band, e.g., $\Delta\lambda \sim 10 \text{ \AA}$, a challenging situation is encountered in that the techniques used to polarize a monochromatic neutron beam can not efficiently polarize a neutron beam with a large wavelength band *and* achieve the large divergence of a monochromatic polarized neutron beam (within one period of the neutron source).

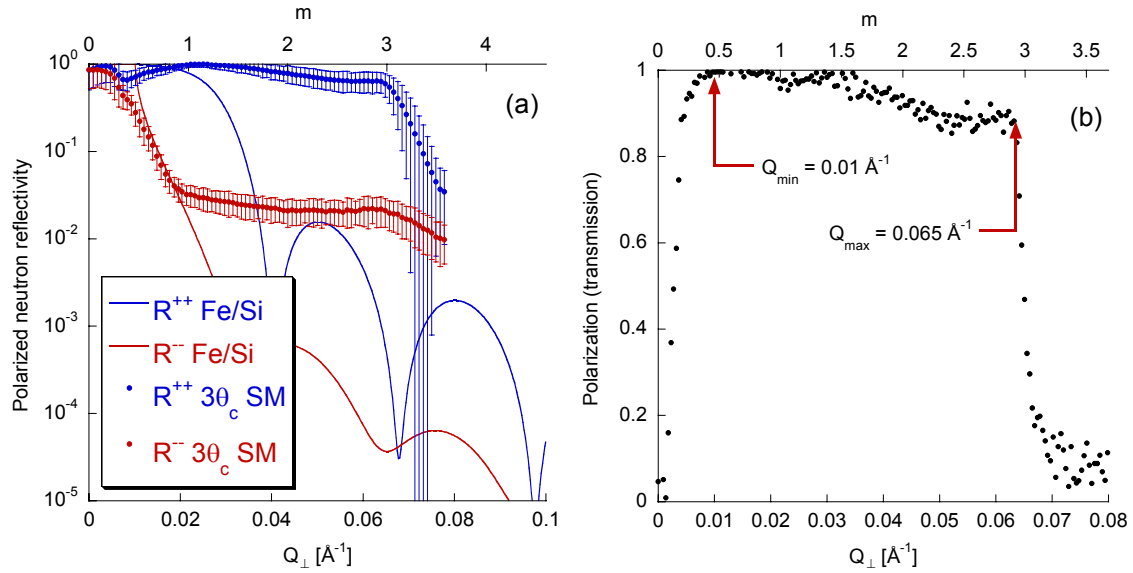


Figure 21 (a) Reflectivity from one of the polarizing supermirrors used in the Mezei polarization cavity. The error bars represent the 1- σ standard deviations of reflectivities measured from 192 of the 196 mirrored-surfaces comprising the polarizing supermirror wedge in the polarization cavity (see text). The calculated reflectivity curves from the Fe/Si example in Figure 11 are shown for

comparison. (b) The polarization obtained from the spin dependence of the neutron beam transmitted through the polarizing supermirror whose reflectivity is shown in (a).

For example, say $3\theta_c$ polarizing supermirrors are placed at an angle of $\theta = 0.9^\circ$ relative to the neutron beam, so as to polarize $\lambda = 5 \text{ \AA}$ neutrons (see Figure 22). Provided the neutron beam is collimated so that neutrons strike the mirror with angles ranging from 0.25° to 1.5° the neutron beam will be polarized (for $\lambda = 5 \text{ \AA}$). Since collimation of the neutron beam is usually achieved with mechanical slits, neutrons with $\lambda = 15 \text{ \AA}$ will also strike the mirror with angles ranging from 0.25° to 1.5° . For these longer wavelength neutrons, Q_\perp ranges from 0.004 to 0.022 \AA^{-1} ; thus, when using the beam transmitted through a polarizer, the neutron beam will remain polarized (neutrons with $Q_\perp < Q_{\min} = 0.01 \text{ \AA}^{-1}$, will be reflected out of the neutron beam regardless of their spin direction), but only a small fraction of the long wavelength neutrons (those satisfying $0.01 \text{ \AA}^{-1} < Q_\perp < 0.022 \text{ \AA}^{-1}$) will be transmitted through the polarizer (about 20% of long wavelength neutrons are transmitted in comparison to short wavelength neutrons). In this configuration, neutrons with $\lambda > \lambda_{\min}$ are inefficiently polarized since $\Delta\theta$ and θ could have been larger. What is needed is a method to achieve the optimum values of $\Delta\theta$ and θ *within one period of the neutron source* for $\lambda > \lambda_{\min}$.

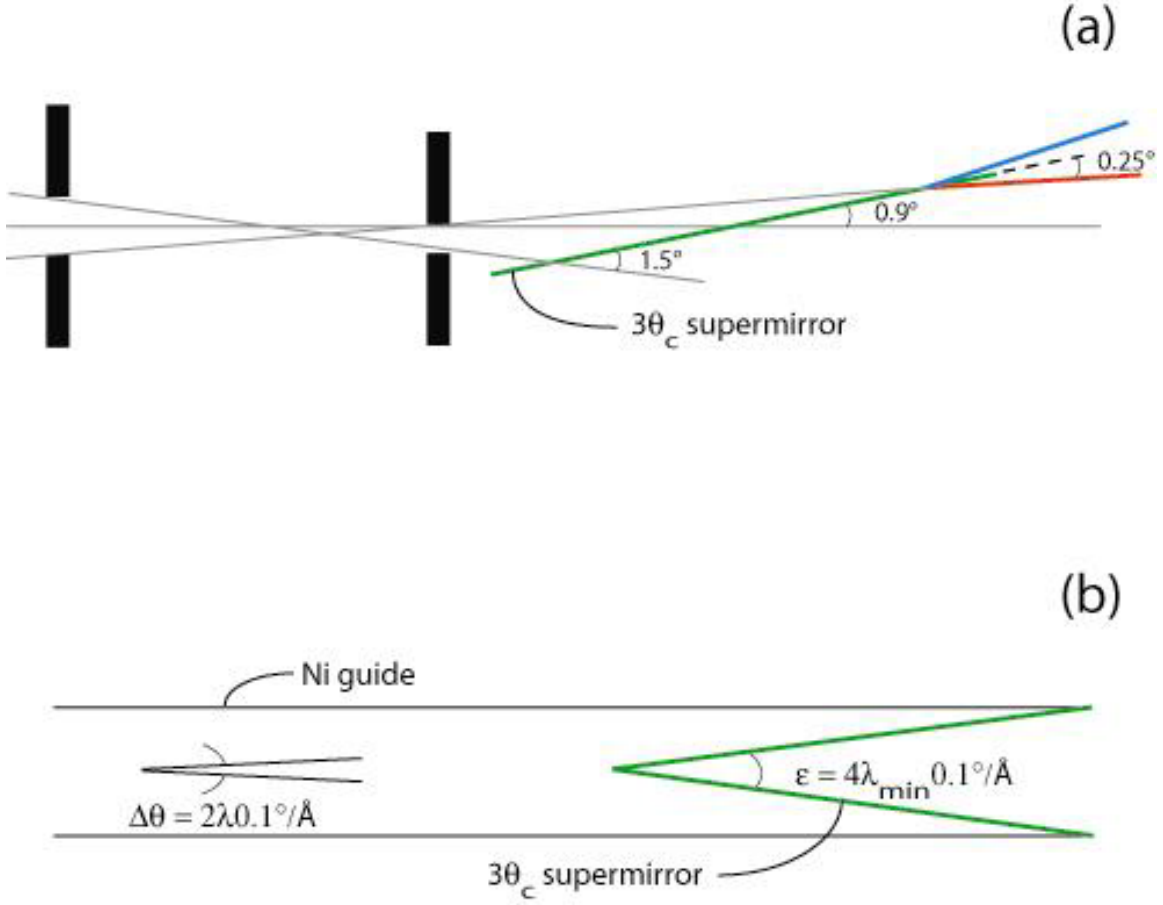


Figure 22 (a) A conventional arrangement for polarizing a neutron beam. Mechanical slits limit the range of trajectories that impinge on a $3\theta_c$ polarizing supermirror. The transmitted neutron beam is polarized spin-down. The minimum and maximum angles have been chosen to assure that the transmitted neutron beam with $\lambda = 5 \text{ \AA}$ is polarized spin-down. Some spin-down neutrons with $\lambda = 15 \text{ \AA}$ (the blue colored trajectory) will nevertheless reflect from the supermirror and be lost from the transmitted polarized beam, thus, reducing the efficiency of this polarization device for multi-wavelength applications. The spatial and angular intensity distributions across the polarized neutron beam will also exhibit undesirable wavelength dependence. (b) A polarization cavity consists of a wedge-shaped arrangement of polarizing supermirrors placed inside a Ni-coated neutron guide (at its end). The divergence of the neutron beam impinging upon the supermirrors is limited by the neutron guide and has a favorable linear dependence upon λ . The angle subtended by the supermirrors, ϵ , is chosen such that only spin-down neutrons with wavelengths greater than a minimum value, λ_{\min} , are transmitted through the cavity.

One solution that achieves these requirements is the so-called polarization cavity [illustrated in Figure 22(b)] [56, 57, 58]. Transmission polarizing supermirrors are placed inside a neutron guide to form the shape of a wedge [Figure 22(b)]. The angle of the wedge, ϵ , is chosen such that $\epsilon = 2(\theta_c^{\text{mirror}} - \theta_c^{\text{guide}})$ where θ_c is the critical angle for

the shortest wavelength, λ_{\min} , in the neutron beam whose polarization is desired. In this scheme, the divergence of the neutron beam illuminating the polarization cavity is that of the neutron guide, and as noted earlier, the divergence increases linearly with wavelength. So, the polarization cavity has the property that any spin-up neutron with $\lambda > \lambda_{\min}$ will be reflected out of the cavity by the supermirrors and escape the neutron guide (to be absorbed by boron in the glass or in the polyethylene surrounding the guide), because after reflection from the supermirrors, the angle of incidence between the neutron and the guide exceeds the critical angle of the guide. On the other hand, spin-down neutrons will travel straight through the wedge mirrors; thus, for $\lambda > \lambda_{\min}$, the neutron beam is polarized spin-down with divergence that increases linearly with λ . Pictures of the interior and exterior of a polarization cavity are shown in Figure 23. The cross-section of the polarized neutron beam produced by the cavity is 130 mm tall by 25 mm wide. The length of the cavity is about 1.2 m.

The mirrors in the polarization cavity are magnetized in a 315 Oe field produced by a solenoid in which the cavity resides [Figure 23(b)]. The polarization axis of the neutron beam at the exit of the cavity is initially directed along the neutron beam line (the x-axis). At the exit of the solenoid, the magnetic field is about 200 Oe (along the x-axis) and decays with distance (Figure 24). Permanent magnets after the solenoid generate a magnetic field transverse to the neutron beam (Figure 24, inset). The variation of the angle, ϕ , of the magnetic field with respect to the neutron beam line with distance from the exit of the guide is shown in the inset of Figure 24. The rate of change in ϕ with time, $d\phi/dt$, is shown in Figure 25 (open symbols) for the case of a neutron with wavelength of $\lambda = 4 \text{ \AA}$. Provided $|d\phi/dt|$ is less than 1/4 of the Larmor precession frequency $\omega_L = \gamma|\mathbf{B}|$,

where $\gamma = -1.833 \times 10^4$ rad/Gs, (i.e., $\left| \frac{d\phi}{dt} \right| < \frac{1}{4} |\varpi_L|$, equivalent to a 3% loss in polarization)

the neutron beam polarization will follow the change in the direction of the magnetic field—the neutron spin changes direction approximately adiabatically [59, 60, 61]. Specifically, the neutron spin precesses on the surface of a cone with frequency equal to ω_L . The axis of the cone changes direction at the rate of $d\phi/dt$. Since the condition for adiabatic rotation of spin is fulfilled for neutrons with wavelength λ_{\min} (see Figure 25) (and therefore for $\lambda > \lambda_{\min}$), the polarization of the neutron beam rotates from the beam axis to one perpendicular to the beam axis with negligible (<3%) loss in polarization [62].



Figure 23 (a) The polarization cavity consisting of a length of neutron guide containing a wedge-shaped arrangement of polarizing transmission supermirrors. (b) The polarization cavity is visible through the end of a solenoid used to magnetize the mirrors. The polarization cavity assembly is supported on a translation stage so that it can be reproducibly slid into and out of the neutron beam as needed.

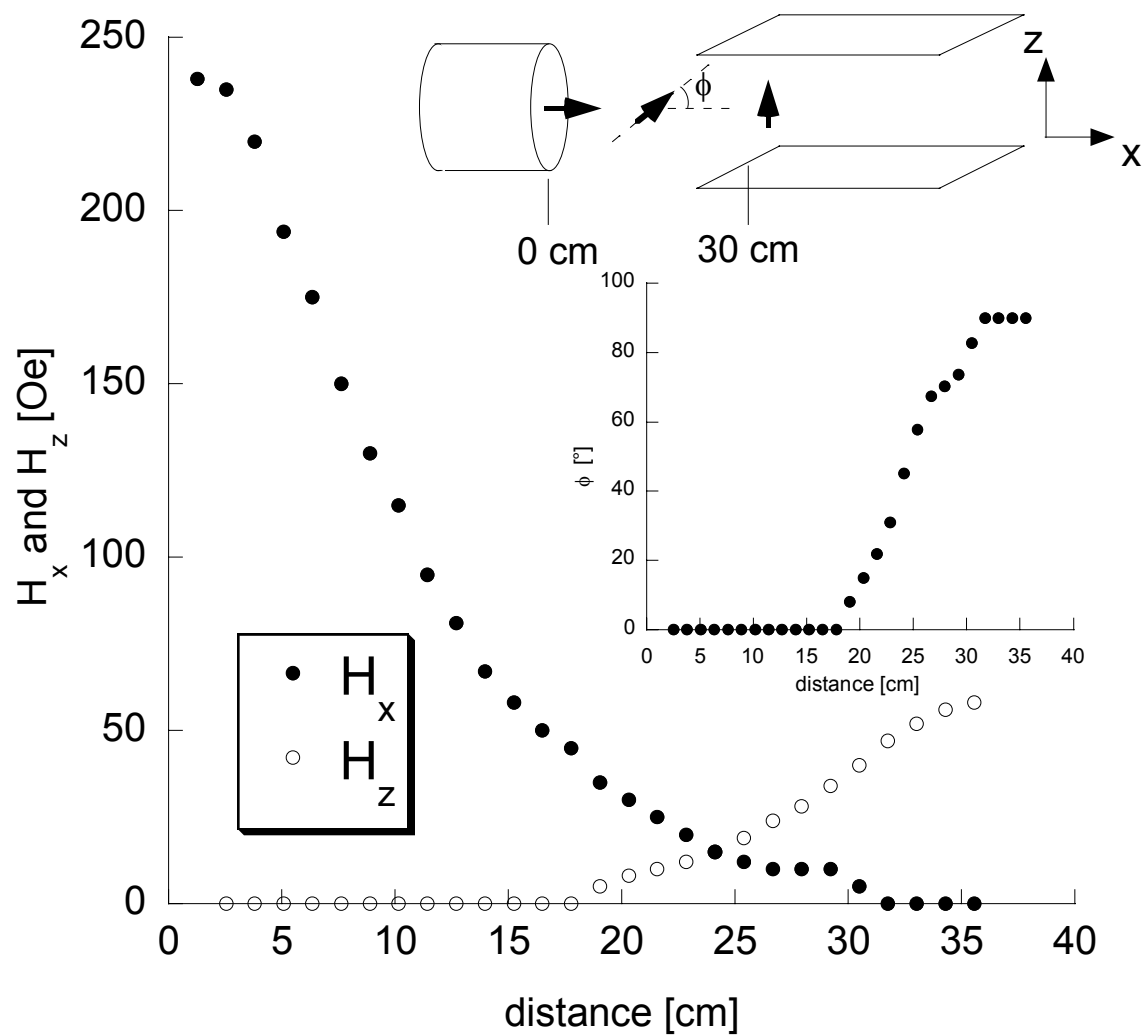


Figure 24 The variation of the x (along the beam axis) and z (in the vertical direction) –components of the magnetic guide field in the region (picture inset) between the exit of the cavity and the beginning of the guide plates is shown. (Graph inset) The angle between the magnetic field and the beam axis is ϕ .

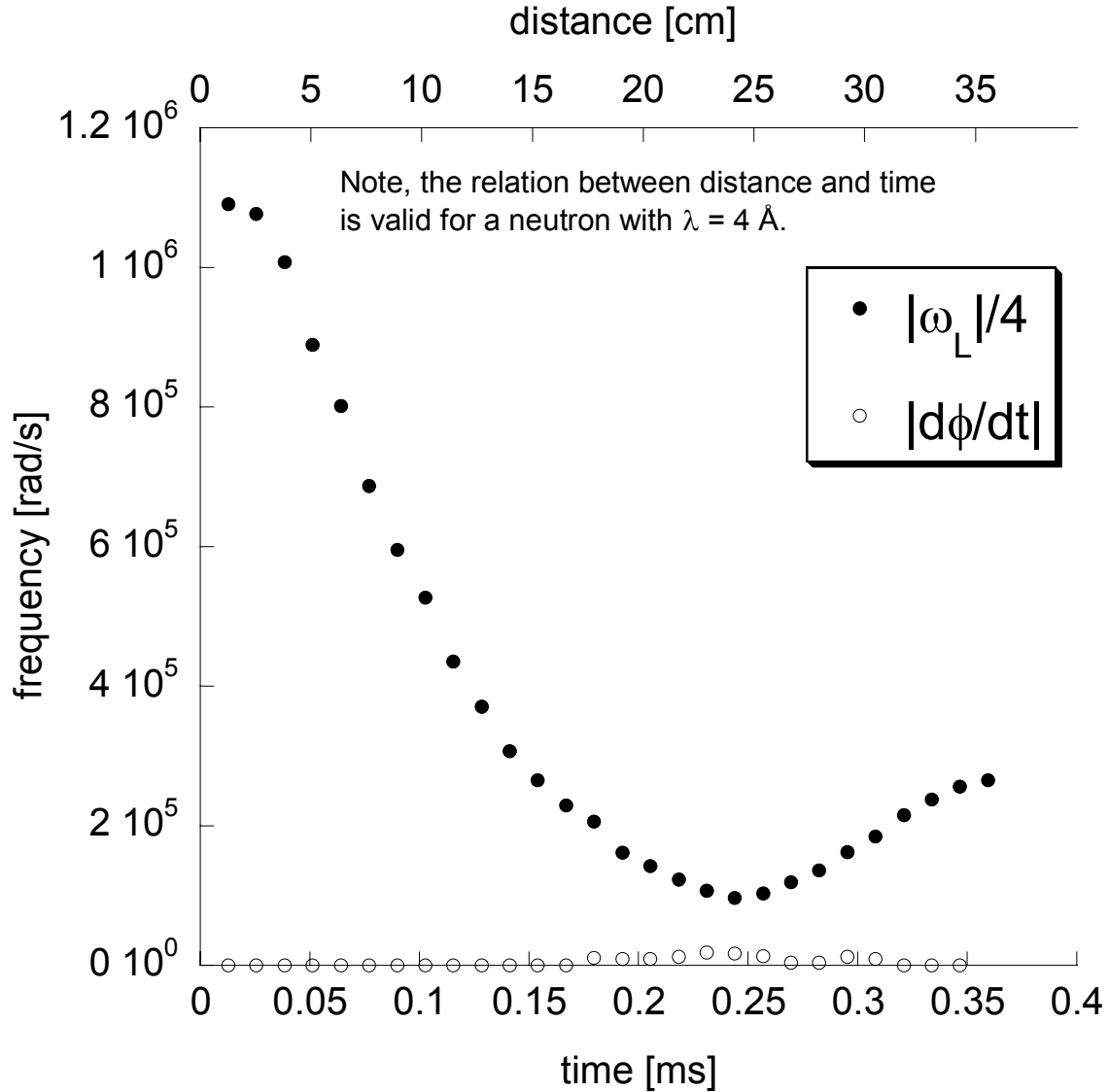


Figure 25 Rate of change in the angle between the magnetic field and the neutron beam line as a neutron with $\lambda = 4 \text{ \AA}$ travels from the exit of the polarization cavity to the beginning of the magnetic guide. Provided $|d\phi/dt|$ (open symbols) $< |\omega_L|/4$ (solid symbols), the neutron spin will follow the magnetic field.

Spin-flippers

In order to separate nuclear and magnetic scattering, at least two measurements are needed—one with spin-up neutrons and the other with spin-down neutrons. Thus, a method of flipping the neutron beam polarization is required. A device that flips the neutron spin is called a spin-flipper. An example of such a flipper—a radio-frequency gradient field spin-flipper [63, 64], is shown in Figure 26 and Figure 27. The flipper

consists of a pair of permanent magnets that are tilted from front to back. The tilt introduces a gradient in the strength of the vertical field (a field that is parallel to the laboratory reference field) along the neutron beam line (x-axis) with a value of about 95 G (large in comparison to stray fields) in the center of the flipper. A magnetic shield consisting of μ -metal sandwiched between layers of steel surrounds the flipper [Figure 27(b)]. The inner steel layer helps return the magnetic field lines created by the permanent magnets inside the flipper; thus, assuring the field, $B_0(x)$, changes linearly with position inside the flipper (Figure 28). The outer steel shield shunts some of the stray field that may be produced by high field magnets (e.g., superconducting magnets) used to magnetize samples. The μ -metal decouples the fields inside the flipper from those outside it. The Larmor precession frequency is shown in Figure 29 as a function of position and time-of-flight (for a neutron with $\lambda = 4 \text{ \AA}$).

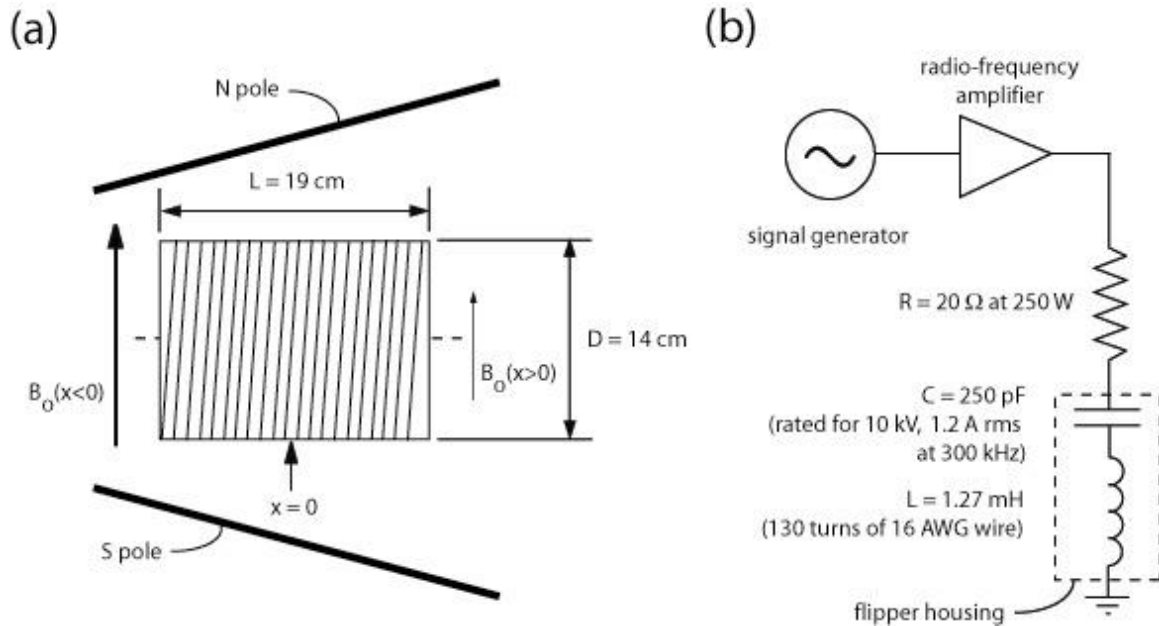


Figure 26 Schematic (a) mechanical and (b) electrical diagrams of the radio-frequency gradient field spin-flipper. The neutron beam line is shown by the dashed line in (a).

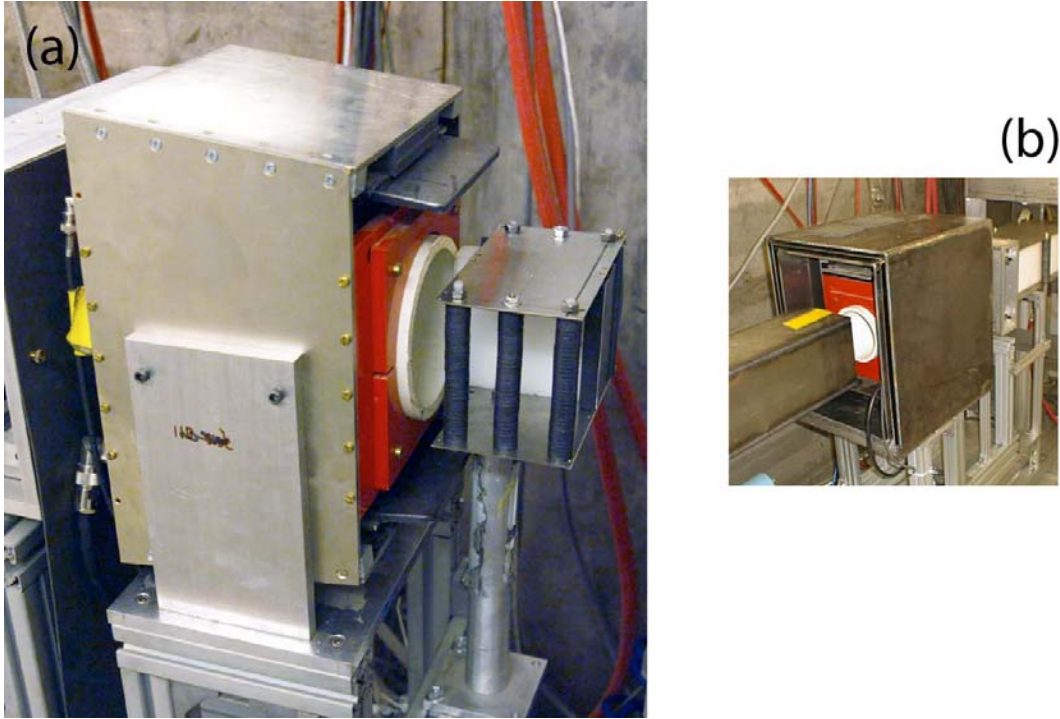


Figure 27 Photograph of a radio-frequency gradient field spin-flipper (a) without and (b) with magnetic shields installed.

By itself, a gradient *in the magnitude* of the field through the flipper will not change the polarization of the neutron beam; rather, a slow (adiabatic) change in direction is needed. The second part of the flipper (the part responsible for the change in direction of the field) is the radio-frequency coil that consists of copper wire wrapped around a ceramic (Al_2O_3) tube. Since the ceramic tube is an insulator, eddy currents (a source of loss) induced by the radio-frequency field are minimized. Connected to the coil are high power capacitors that form a resonance circuit [see Figure 26(b)]. When radio-frequency power (~ 70 W) is applied to the flipper, the resultant magnetic induction inside the flipper consists of a time independent (static) component (from the permanent magnets) transverse to the beam line (i.e., parallel to the z-axis), and a component that rotates with frequency ω_0 in the x-y plane. In the rotating frame of reference (one that rotates with the radio-frequency field about the z-axis), the effective field is a combination of two

fields whose orientations are fixed in the rotating frame: one is the peak amplitude of the radio-frequency field ($B_I \sim 13$ G) (Figure 28), and the other is the spatially changing component in the vertical direction with a constant offset removed [60]. The effective induction, \mathbf{B}_{eff} , is given by:

$$\mathbf{B}_{eff}(x) = \left(B_0(x) - \frac{\varpi_0}{|\gamma|} \right) \hat{z} + B_1 \hat{x}$$

Equation 36

In the rotating frame of reference, \mathbf{B}_{eff} changes direction smoothly with position (see Figure 28, inset)—first directed up, then down from the front to the back of the flipper. The rate of change in angle of \mathbf{B}_{eff} , $d\phi/dt$, and $1/4\omega_L$ (for $\lambda = 4$ Å) with position along the beam line is shown in Figure 29. Since $\left| \frac{d\phi}{dt} \right| < \frac{1}{4} |\varpi_L|$, the polarization of the neutron beam rotates 180° adiabatically, provided the flipper is energized. By choosing $\varpi_0 = |\gamma B_0(x=0)|$, which corresponds to about $2\pi \cdot 297$ kHz, the midpoint in the 180° rotation of the polarization occurs in the center of the flipper.

The measured flipping efficiency of the radio-frequency gradient field spin-flipper is shown in Figure 30. This flipper performs nearly ideally approaching flipping efficiencies of 100% over a broad range of wavelengths ($\lambda > \lambda_{min}$). Besides efficiently flipping neutron spin, the flipper also has two other attractive properties: first, tuning, e.g., optimization of currents etc., is never required even if the stray field environment changes, and secondly, no material is introduced into the beam line (i.e., the flipper is hollow) that might otherwise increase the background of the instrument or absorb neutrons.

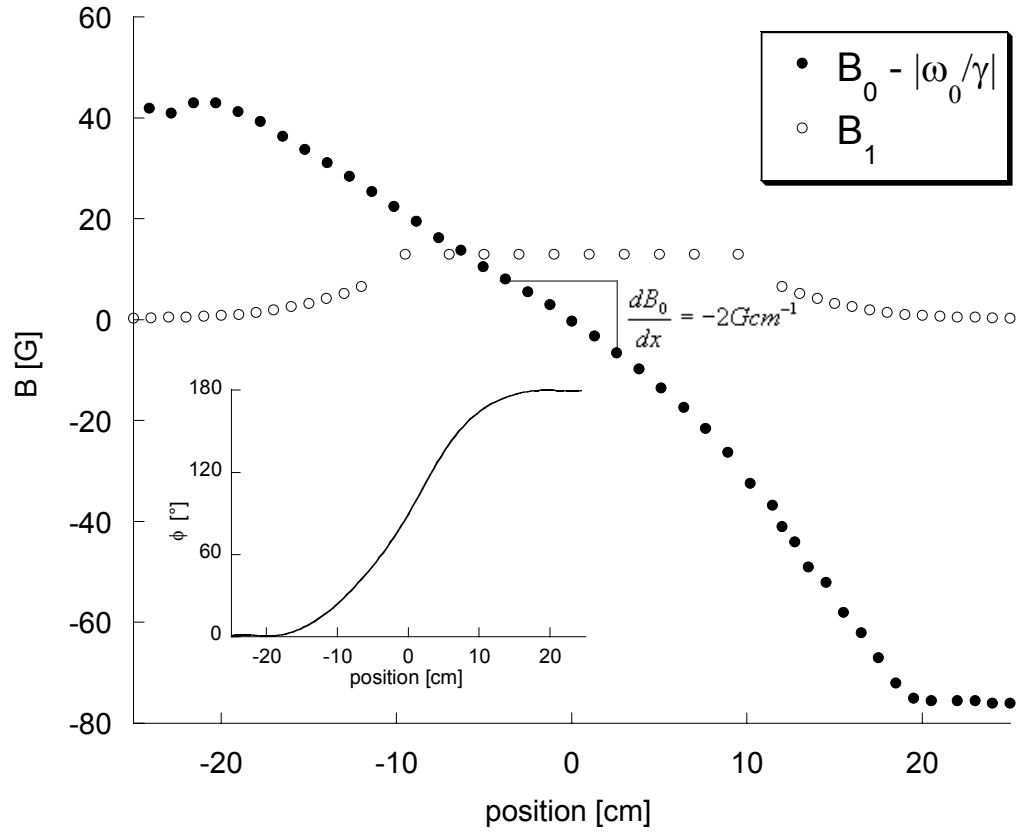


Figure 28 Plot of the variation in the static field component, B_0 , and the amplitude (when the spin-flipper is turned on) of the radio-frequency field component, B_1 with position along the centerline of the spin-flipper. Inset: The angle, ϕ , between the effective field, B_{eff} , and the z-axis, corresponding to the direction of the magnetic field applied to the sample (and the laboratory frame of reference). For the case when the spin-flipper is off, $B_1 = 0$, so $\phi = 0$ for all positions through the flipper.

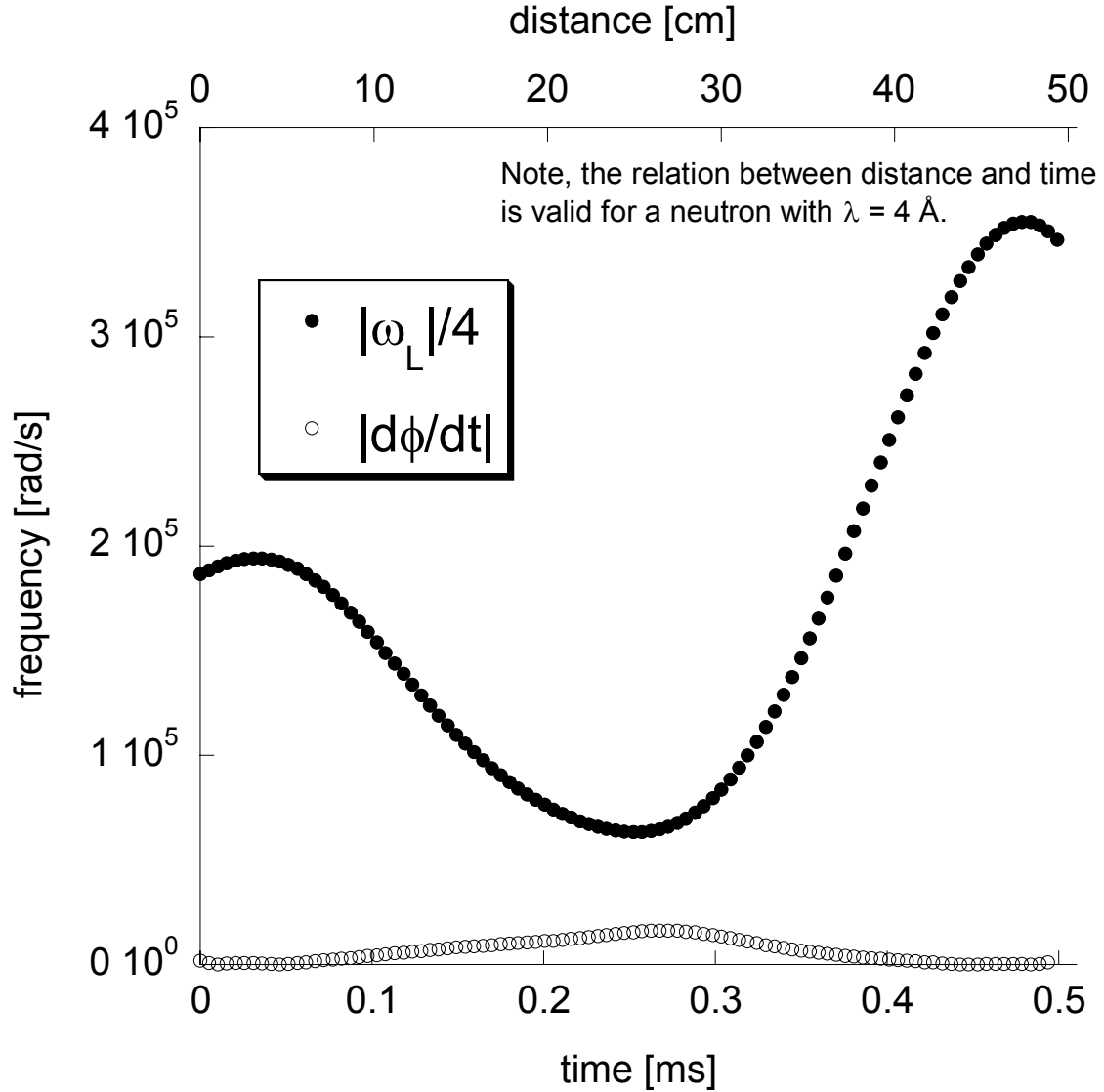


Figure 29 Rate of change in the angle between the magnetic field and the z-axis as a neutron with $\lambda = 4 \text{ \AA}$ travels from the exit of the polarization cavity to the beginning of the magnetic guide. Provided $|d\phi/dt|$ (open symbols) $< |\omega_L|/4$ (solid symbols), the neutron spin will follow the effective magnetic field.

During an experiment, the radio-frequency coil is energized (de-energized) to obtain spin-up (down) neutrons, for example the coil might be cycled on and off every couple minutes. For experiments requiring measurements of the four spin-dependent neutron cross-sections a second flipper (Figure 18) and another polarizing device (Figure 18, though this device is usually a simple polarizing supermirror or stack of polarizing

supermirrors) are required. For these experiments, the two flippers are cycled on and off in the four possible combinations. Figure 31 shows the detector arm on which the second spin-flipper, polarization analyzer and detector rests.

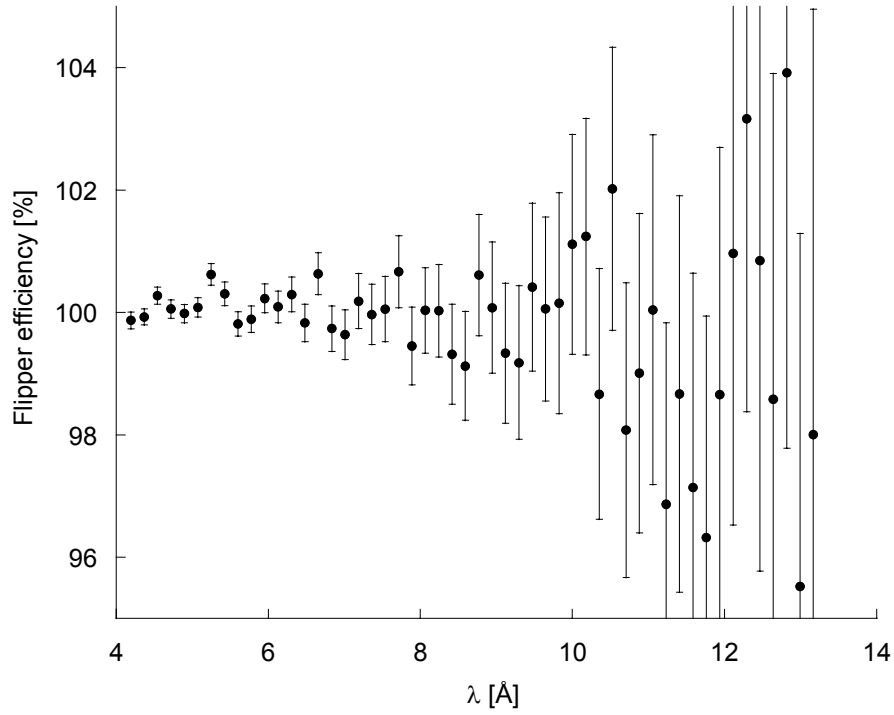


Figure 30 Variation of the efficiency of the flipper to flip a polarized neutron beam while maintaining good polarization is shown as a function of wavelength. The average flipper efficiency is 99.8%.



Figure 31 (a) View from the detector-end of the reflectometer. An 11-T superconducting magnet is visible in the background. (b) View from the sample position towards the detector.

Applications of polarized neutron reflectometry

In this section we describe two applications of polarized neutron reflectometry to the study of a simple magnetic system. In the first example, X-ray and polarized neutron reflectivity data are analyzed separately, and then jointly, to obtain the magnetic structure of a sample of FeCo on GaAs [65]. This example illustrates how the reflectivity obtained from a model of the chemical composition of a sample is fitted to X-ray data using the computer routine CO_REFINE. From this analysis, parameters for surface and interface roughness and film thickness are obtained. These parameters serve as initial guesses in the refinement of a second model to the neutron data that also uses CO_REFINE. Finally, the X-ray and neutron models are compared, and a new model—one that includes a reacted layer between the magnetic film and substrate, is fitted to the X-ray and neutron data at the same time using CO_REFINE to achieve a consistent explanation for all the data.

In the second example, we illustrate application of vector magnetometry using neutron scattering to isolate the magnetic scattering from the nuclear scattering of the same sample. In this example, a nuclear model is fitted to the non-spin-flip scattering and a magnetic model to the spin-flip scattering. Again, the magnetic and nuclear layer thicknesses of the film differ and are reconciled by the addition of a non-magnetic reacted layer between the magnetic layer and substrate.

Magnetic vs. chemical structures identified through X-ray and polarized neutron reflectometry

In this example, a detailed understanding of the magnetic structure of the interface in one prototypical spin injection heterostructure comprised of an alloy of FeCo on one side (the spin source) and GaAs(100) on the other side (the spin sink) is obtained using a

combination of X-ray and polarized neutron reflectometry. The example demonstrates use of the computer routine CO_REFINE to obtain a magnetic and nuclear model whose X-ray and polarized neutron (non-spin-flip) reflectivities fit the data. In fitting the model to the data, we find evidence for a 5.5 Å thick non-ferromagnetic region, containing FeCo, near the FeCo/GaAs interface, in a 20-nm thick FeCo film.

The sample consists of an Fe₄₈Co₅₂ film epitaxially grown onto semi-insulating GaAs(100) (2x4)/c(2x8)β2 –As rich surface [66] by molecular beam epitaxy under ultra high vacuum and characterized by *in situ* electron diffraction and *ex situ* X-ray diffraction, Rutherford backscattering spectrometry, transmission electron microscopy and magnetometry. The 20-nm thick FeCo layer was grown at 95°C, and a 3 nm thick Al capping layer was subsequently deposited to prevent oxidation during *ex situ* characterization. The detailed sample preparation and structural characterization results are described elsewhere [67]. The magnetization hysteresis loops of FeCo alloy grown on GaAs(100) (2x4)/c(2x8)β2 with magnetic fields applied along two perpendicular directions in the sample plane are shown in Figure 32. The magnetization measured along the [011] direction (solid curve) indicates this axis is an easy axis, while the sheared hysteresis loop measured along the [01 $\bar{1}$] direction (dashed curve) suggests this direction is considerably harder.

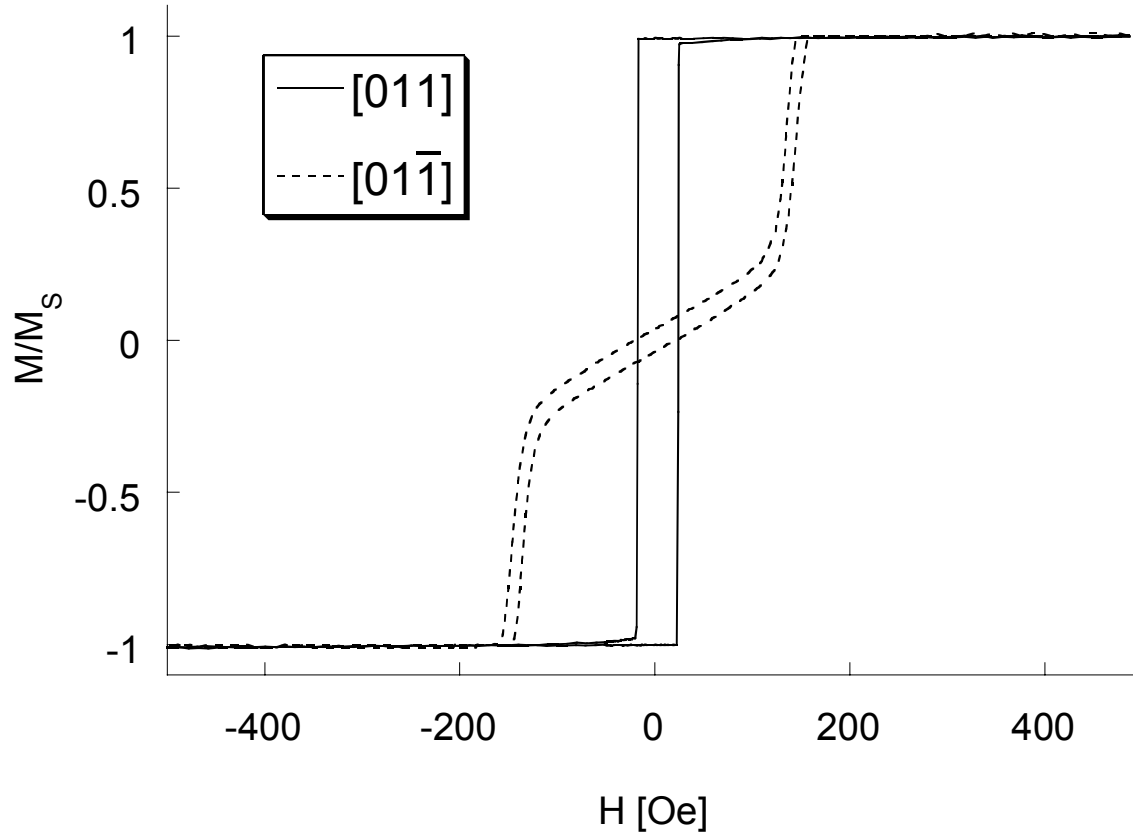


Figure 32 Magnetization of the FeCo/GaAs sample along the easy, $[011]$, and hard, $[01\bar{1}]$, axes. The sample magnetization has a large uniaxial anisotropy.

The specular X-ray reflectivity of the sample after removal of diffuse scattering (Figure 33) was measured at room temperature with a conventional rotating anode X-ray generator, producing $\text{CuK}\alpha$ radiation, and a position sensitive detector as described elsewhere [68]. One important distinction between how X-ray and neutron reflectivity data are collected involves the portion of the sample illuminated by the respective beam. Generally (with the exception of the very small Q_{\perp} region), the X-ray beam illuminates only a portion of the sample, whereas, in the case of neutron reflectometry, the sample is most often completely bathed in the neutron beam. When comparing the X-ray and neutron reflectivity data from the same sample it is important to be cognizant of the possibility that the two techniques are perhaps measuring different quantities, since the

sample may not be uniform over its entire surface. In order to minimize the influence of non-uniformity (if any) of the sample on the reflectivity data, the X-ray reflectivity of the sample was measured over several parts of the sample in order to make a more accurate comparison (by addition of the curves) with the neutron measurements.

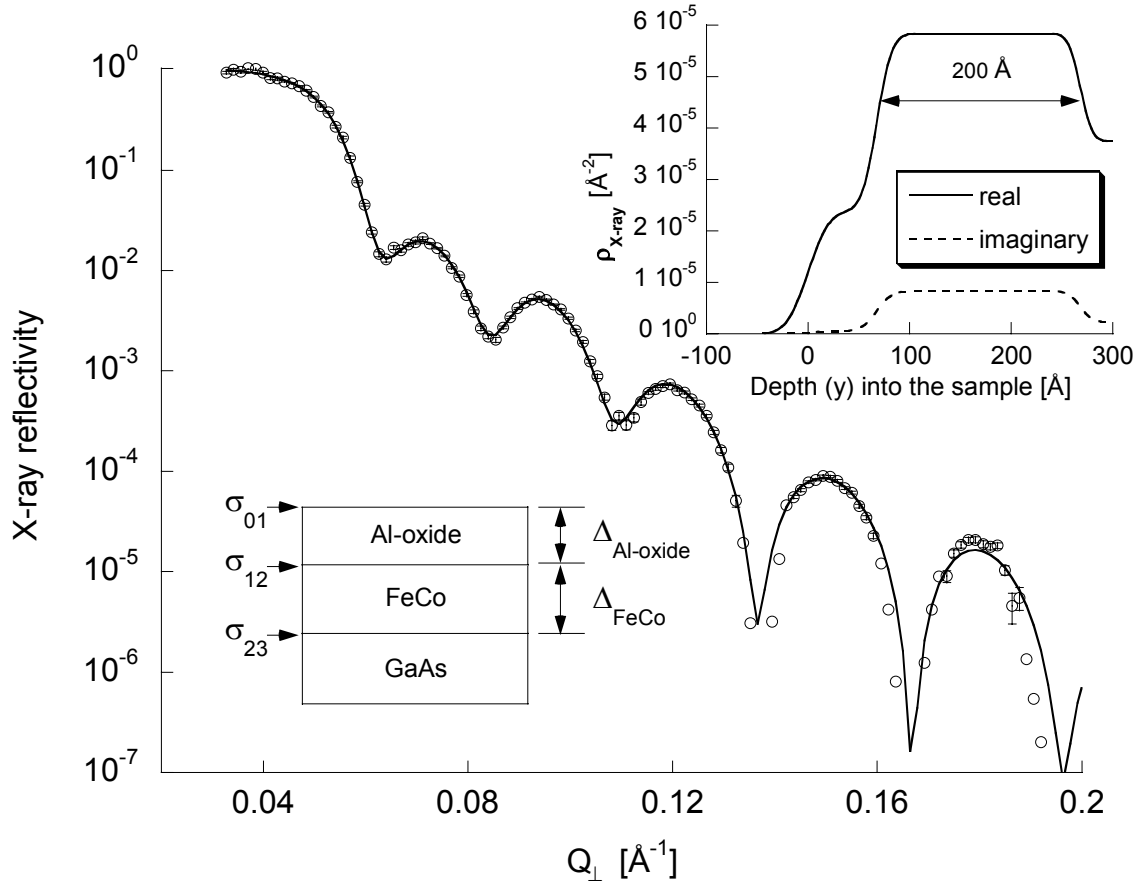


Figure 33 X-ray reflectivity (open symbols) of the FeCo/GaAs sample. The calculated reflectivity (solid curve) is from the model shown in the inset.

The X-ray reflectivity (solid curve, Figure 33) of a model structure [Figure 33, inset] was calculated using the optical formalism of Parratt [4]. The initial guesses for the parameters of the model from which the X-ray scattering length density profile was calculated, are given in Table 3. These values were chosen based on knowledge of the deposition process, and using literature values for the X-ray scattering length density,

$\rho_x = NZr_e$, where Z is the atomic number (per formula unit) and r_e is the Bohr radius of 2.82×10^{-5} Å. In principle, ρ_x is a complex number with the imaginary component related to the mass absorption length of the X-ray beam in the material. The imaginary component of ρ_x was initially assigned a value of zero; however, its value will be optimized (the imaginary component of ρ_x for FeCo will be significant for $\text{CuK}\alpha$ radiation).

The CO_REFINE routine optimized the parameters within the constraints of the lower and upper bounds listed in the Table 3 subject to the condition that χ^2 —a measure of error between the fitted and observed curves was minimized [69]. The optimized parameters of the model are shown in the second to last column of Table 3. The last column of Table 3 lists the perturbations to the optimized parameters such that the reduced χ^2 , $\chi_v^2 = \chi^2/v$ (where v is the number of data points minus adjustable parameters), is changed by one, i.e., the last column represents the perturbation to the optimized parameter that significantly worsens the fit by 1- σ [70]. The error bar is a measure of the sensitivity of the model function to yield a curve that represents the data. The error bar is not necessarily a representation of the uncertainty of the fitted parameter.

As a mechanism to understand the accuracy and precision of the optimized parameters, it is instructive to compare them with the initial guesses. In the case of the Al-oxide layer thickness, the initial guess of 30 Å was chosen based on the quantity of Al deposited in the growth chamber. Naturally, upon exposure to air, the Al will oxidize and thus its layer thickness can be expected to swell. In this case the swelling of a 30 Å thick film is roughly a factor of two. The X-ray scattering length density attributed to the Al-oxide layer is greater than that for Al [$\rho_x(\text{Al}) = 2.2 \times 10^{-5}$ Å⁻²], but less than that for Al_2O_3

$[\rho_x(\text{Al}_2\text{O}_3) = 3 \times 10^{-5} \text{ \AA}^{-2}]$. The intermediate value of $2.39 \times 10^{-5} \text{ \AA}^{-2}$ might indicate the oxide layer is composed of elemental Al and Al_2O_3 . Further support for this conclusion is found in the large value of surface roughness/diffusion (in comparison to the buried interfaces).

The FeCo layer thickness is certainly in good agreement with the thickness sought by the sample growers. The magnitude of $|\rho_x|$ is 90% of the initial guess for FeCo obtained from the lever-rule addition of ρ_x for bulk Fe and Co. The value of ρ_x obtained for GaAs, which has a small imaginary component, is very close to that obtained from the literature. The difference, $\Delta\rho_x = 0.25 \times 10^{-5} [\text{ \AA}^{-2}]$, can be related to misalignment of the sample (or measurement of α_i), by differentiating the relation

$$Q_c = 4\sqrt{\pi\rho} = \frac{4\pi \sin(\alpha_i)}{\lambda} \text{ with respect to } \alpha_i. \text{ A misalignment of the sample of by } \Delta\alpha_i =$$

0.03° could account for the difference between the measured and literature values of ρ_x

Next, we wish to combine the X-ray reflectivity study, from which information about the chemical or nuclear structure of the sample is learned, with polarized neutron reflectivity data taken from the sample in a large, 1 kOe, (saturating) magnetic field. The intent of the neutron study is to identify the Fourier components of the sample magnetization, in order to distinguish the magnetization of the FeCo/GaAs interface from the FeCo bulk.

The specular reflectivity (after removal of diffuse scattering) is shown in Figure 34. The SF reflectivity was also measured, but no SF reflectivity was observed. The lack of SF (specular) reflectivity is consistent with the sample being saturated, i.e., the entire sample magnetization was parallel to the 1-kOe field.

Table 3 Listing of initial guess values for the model, v_0 , lower, v_- , and upper, v_+ , bounds with which to limit the optimization, the optimal values that yield a minimum in χ^2 , and the perturbation, δv , of the value that produces an increase in χ^2 corresponding to a 1- σ error bar. The number of data points is 134.

Medium	Parameter	v_0	v_-	v_+	v_{opt}	δv
Vacuum	$\text{Re}(\rho_X) \times 10^{-5} [\text{\AA}^{-2}]$	0			0	
	$\text{Im}(\rho_X) \times 10^{-5} [\text{\AA}^{-2}]$	0			0	
	$\sigma_{01} [\text{\AA}^2]$	10	5	20	16.4	0.8
	$\Delta [\text{\AA}]$	0			0	
Al-oxide	$\text{Re}(\rho_X) \times 10^{-5} [\text{\AA}^{-2}]$	3	1	4	2.39	0.01
	$\text{Im}(\rho_X) \times 10^{-5} [\text{\AA}^{-2}]$	0	0	1	0.059	0.004
	$\sigma_{12} [\text{\AA}^2]$	10	5	20	11.75	0.03
	$\Delta [\text{\AA}]$	30	20	80	67.77	0.08
FeCo	$\text{Re}(\rho_X) \times 10^{-5} [\text{\AA}^{-2}]$	6.6	4	7	5.835	0.005
	$\text{Im}(\rho_X) \times 10^{-5} [\text{\AA}^{-2}]$	0	0	2	0.83	0.01
	$\sigma_{23} [\text{\AA}^2]$	10	5	20	9.21	0.05
	$\Delta [\text{\AA}]$	200	190	210	200.41	0.08
GaAs	$\text{Re}(\rho_X) \times 10^{-5} [\text{\AA}^{-2}]$	3.99	2	5	3.74	0.01
	$\text{Im}(\rho_X) \times 10^{-5} [\text{\AA}^{-2}]$	0	0	1	0.23	0.04
	$\chi^2 (v = 121)$	704614			382	

The model shown in the inset of Figure 34 was fitted to the neutron data. The initial guesses for this model were obtained from the X-ray analysis with the exception that values of ρ_n and ρ_m were calculated based on literature values of the neutron scattering lengths and magnetization of FeCo (see Table 4). The routine CO_REFINE was once again used to obtain the parameters of the model (listed in Table 4) such that the calculated reflectivities fitted the neutron data. The reflectivity curves obtained from the model are shown as the solid curves in Figure 34. Interestingly, the fitted chemical layer thickness of FeCo obtained from the analysis of the X-ray data is larger than that obtained from the analysis of the (neutron) *NSF* reflectivities. One explanation for the difference is that the X-ray fitting is one involving only the chemical structure of the sample, while the neutron fitting weights the magnetic and nuclear contributions roughly equally. The implication is the magnetic thickness of the FeCo layer is less than its chemical thickness.

In order to test this idea, a new model was developed—one that included an extra interface layer between the FeCo film and the GaAs substrate. The FeCo layer thickness was constrained to be the value obtained from neutron scattering, i.e., $\Delta_{\text{FeCo}} = 197 \text{ \AA}$, and the thickness of the “reacted” layer was constrained to be the difference between the values of Δ_{FeCo} determined separately by X-ray and neutron fitting, or 3 \AA . The new model was then fitted or co-refined to the X-ray and polarized neutron reflectivity data at the same time. Values intermediate between the optimized values in Table 3 and Table 4 were chosen as initial guesses for the new model. The initial guesses of ρ_x , ρ_n and ρ_m for the reacted layer were chosen to be ρ_x for the FeCo layer, and ρ_n and $\rho_m (= 0)$ for GaAs, respectively (see Table 5). The X-ray and neutron reflectivities obtained from the model

are shown in Figure 35. The magnetization refined for the reacted layer is not significantly different than zero; therefore, we conclude that the additional level of complexity achieved by adding a thin non-magnetic layer between the FeCo and GaAs, yields one model that explains the X-ray and neutron data in a self-consistent fashion.

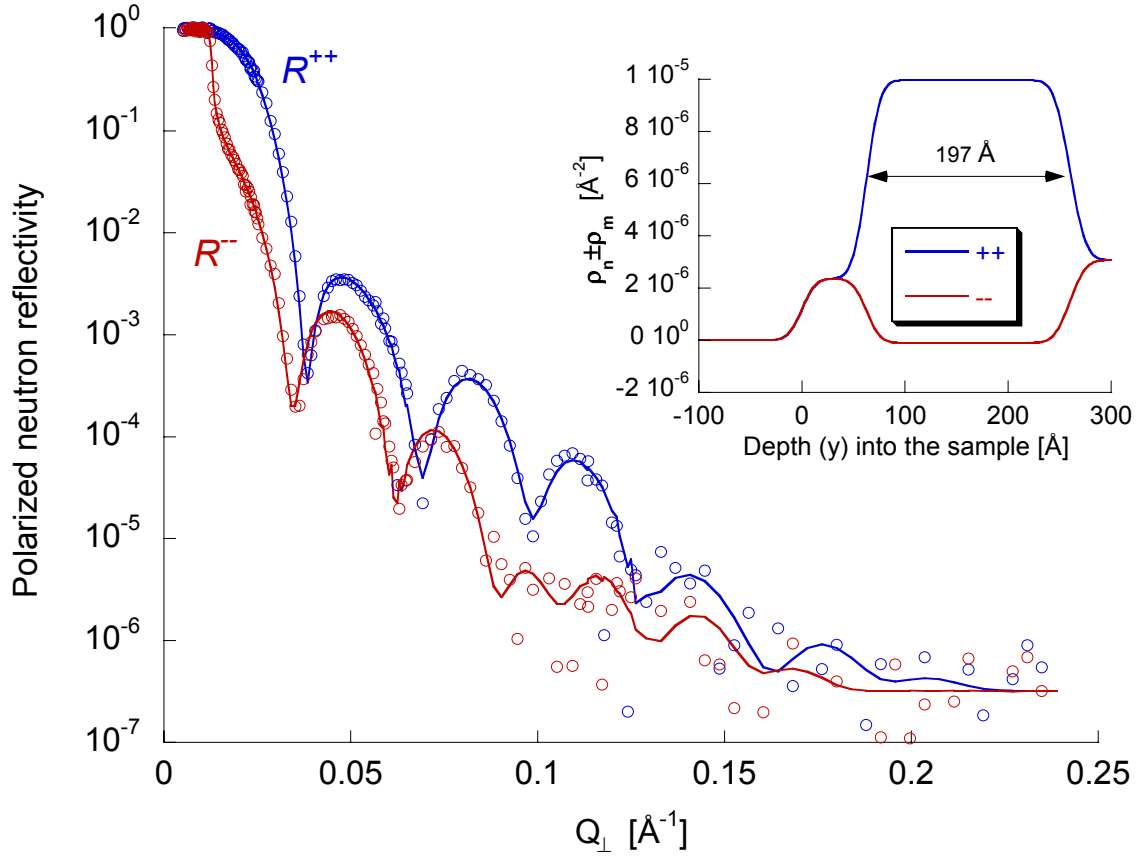


Figure 34 Polarized neutron reflectivity data (open symbols) for the FeCo/GaAs sample are shown along with reflectivity curves (solid curves) that best fit the data obtained from a model structure (inset). The initial guesses for the fitting procedure were those obtained from the fit to the X-ray data. This fit is to the neutron data only.

Table 4 Listing of guess and optimized parameters for a fit of the FeCo/GaAs model structure to the polarized neutron reflectivity data consisting of 348 measurements.

Medium	Parameter	v_0	v_-	v_+	v_{opt}	δv
Vacuum	$\rho_n \times 10^{-6} [\text{\AA}^{-2}]$	0			0	
	$\rho_m \times 10^{-6} [\text{\AA}^{-2}]$	0			0	
	$\sigma_{01} [\text{\AA}^2]$	16.4	5	20	10.6	0.3
	$\Delta [\text{\AA}]$	0			0	
Al-oxide	$\rho_n \times 10^{-6} [\text{\AA}^{-2}]$	5.21	2	6	2.36	0.02
	$\rho_m \times 10^{-6} [\text{\AA}^{-2}]$	0			0	
	$\sigma_{12} [\text{\AA}^2]$	11.75	5	20	10.8	0.1
	$\Delta [\text{\AA}]$	67.77	20	80	62.7	0.3
FeCo	$\rho_n \times 10^{-6} [\text{\AA}^{-2}]$	5.13	4	6	4.94	0.01
	$\rho_m \times 10^{-6} [\text{\AA}^{-2}]$	4.97	4	6	5.04	0.01
	$\sigma_{23} [\text{\AA}^2]$	9.21	5	20	12.0	0.1
	$\Delta [\text{\AA}]$	200.41	190	210	197.5	0.1
GaAs	$\rho_n \times 10^{-6} [\text{\AA}^{-2}]$	3.07	2	4	3.07	0.02
	$\rho_m \times 10^{-6} [\text{\AA}^{-2}]$	0			0	
	$\chi^2 (v = 337)$	26868			1102	

Table 5 Refinement of one model to X-ray and polarized neutron reflectivity data (consisting of 482 measurements) at the same time.

Medium	Parameter	v_0	v_-	v_+	v_{opt}	δv
Vacuum	$\text{Re}(\rho_x) \times 10^{-5} [\text{\AA}^{-2}]$	0			0	
	$\text{Im}(\rho_x) \times 10^{-5} [\text{\AA}^{-2}]$	0			0	
	$\rho_n \times 10^{-6} [\text{\AA}^{-2}]$	0			0	
	$\rho_m \times 10^{-6} [\text{\AA}^{-2}]$	0			0	
	$\sigma_{01} [\text{\AA}^2]$	13.6	5	20	15.6	0.08
	$\Delta [\text{\AA}]$	0			0	
Al-oxide	$\text{Re}(\rho_x) \times 10^{-5} [\text{\AA}^{-2}]$	2.39	2	3	2.17	0.01
	$\text{Im}(\rho_x) \times 10^{-5} [\text{\AA}^{-2}]$	0.06	0	1	0.08	0.01
	$\rho_n \times 10^{-6} [\text{\AA}^{-2}]$	2.36	2	6	2.68	0.02
	$\rho_m \times 10^{-6} [\text{\AA}^{-2}]$	0			0	
	$\sigma_{12} [\text{\AA}^2]$	11.2	5	20	11.82	0.02
	$\Delta [\text{\AA}]$	65.2	60	70	65.46	0.02
FeCo	$\text{Re}(\rho_x) \times 10^{-5} [\text{\AA}^{-2}]$	5.83	5	6	5.75	0.03
	$\text{Im}(\rho_x) \times 10^{-5} [\text{\AA}^{-2}]$	0.83	0	1	0.72	0.08
	$\rho_n \times 10^{-6} [\text{\AA}^{-2}]$	4.94	4	6	5.01	0.01
	$\rho_m \times 10^{-6} [\text{\AA}^{-2}]$	5.03	4	6	5.00	0.01
	$\sigma_{23} [\text{\AA}^2]$	10.5	5	20	10.8	0.1
	$\Delta [\text{\AA}]$	197.5			197.5	
Reacted	$\text{Re}(\rho_x) \times 10^{-5} [\text{\AA}^{-2}]$	5.83	3	6	5.13	0.02

	$\text{Im}(\rho_X) \times 10^{-5} [\text{\AA}^{-2}]$	0.83	0	1	0.31	0.02
	$\rho_n \times 10^{-6} [\text{\AA}^{-2}]$	3.08	3	7	6.1	0.3
	$\rho_m \times 10^{-6} [\text{\AA}^{-2}]$	0	0	6	0.00	0.02
	$\sigma_{23} [\text{\AA}^2]$	10.5	5	20	7.63	0.04
	$\Delta [\text{\AA}]$	2.9			2.9	
GaAs	$\text{Re}(\rho_X) \times 10^{-5} [\text{\AA}^{-2}]$	3.74	3	4	3.84	0.01
	$\text{Im}(\rho_X) \times 10^{-5} [\text{\AA}^{-2}]$	0.23	0.2	0.3	0.23	0.02
	$\rho_n \times 10^{-6} [\text{\AA}^{-2}]$	3.08	2	4	3.10	0.02
	$\rho_m \times 10^{-6} [\text{\AA}^{-2}]$	0			0	
	$\chi^2 (\nu = 459)$	4182			1617	

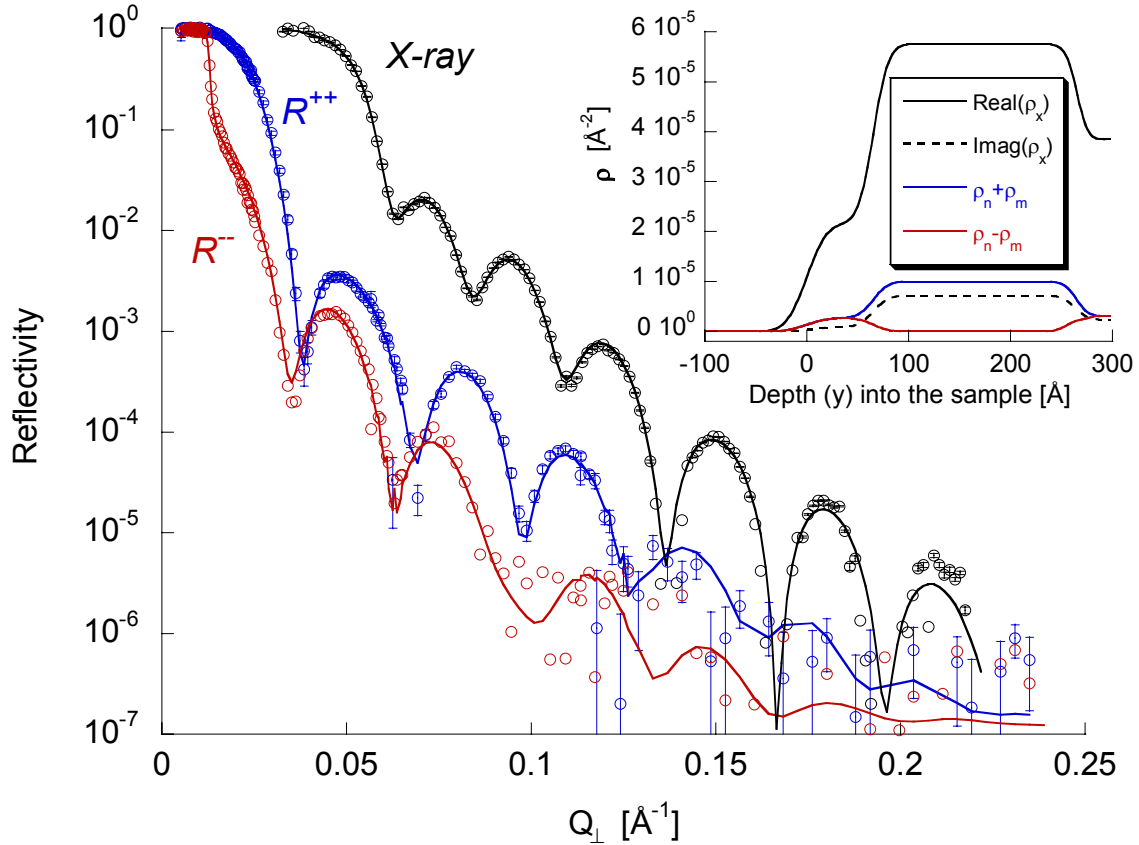


Figure 35 X-ray and neutron reflectivity curves of one model (inset) fitted to the X-ray and neutron data at the same time.

Magnetic and chemical structures obtained from vector magnetometry using neutron scattering

For magnetic systems with large remanent magnetization (or strong anisotropy), polarized neutron reflectometry with polarization analysis is a powerful tool for isolating the nuclear or chemical structure of a material from its magnetic structure. Indeed, artificially structured materials are examples of systems that often exhibit unusual magnetic anisotropies. Here, we show how the uniaxial anisotropy of a material and neutron scattering can be applied to rigorously separate the nuclear and magnetic structures of the sample discussed in the previous example.

First the magnetic history of the sample is prepared by applying a field along the [011] (easy) axis of the GaAs substrate (Step 1, Figure 36). The field is chosen to be large enough (1 kOe) in order to saturate the sample magnetization (Figure 32). Next, the field is reduced monotonically to a small value on the order of a few Oe (Step 2, Figure 36). The magnetization of the sample in this field remains nearly the same as its saturated value (see Figure 32). The sample is then rotated about its surface normal by 90° (Step 3, Figure 36), and the non-spin-flip and spin-flip reflectivities for the sample in a field of 9 Oe pointed along the $[01\bar{1}]$ axis are measured (Figure 37).

In order to investigate whether the nuclear and magnetic layer thicknesses of the FeCo layer were different, a second model was fitted to the data (symbols) shown in Figure 37. This model represents the nuclear and magnetic structures of the sample (inset, Figure 37) separately—the magnetic and nuclear layer thicknesses and interface roughnesses are optimized independently. Finally, to account for the vector property of the sample magnetization, an angle, ϕ , between the sample magnetization and the applied field (Figure 36) was also refined. The best fitting reflectivities are shown as the solid curves in Figure 37. The input guesses and the optimized parameters for the nuclear and magnetic models are listed in Table 6.

An important result of the data analysis is that the portion of the sample magnetization that rotated with the sample is about 5.5 Å thinner than the thickness attributed to the nuclear scattering from FeCo. In other words the magnetic thickness of FeCo is 197 Å thick. This result is consistent with the conclusion of the previous analysis of the X-ray and polarized neutron data which in order to account for a discrepancy between chemical thickness as determined by X-ray reflectometry and

magnetic thickness as determined by polarized neutron reflectometry (of the sample taken in saturation), a thin non-magnetic reacted layer was needed between FeCo and GaAs.

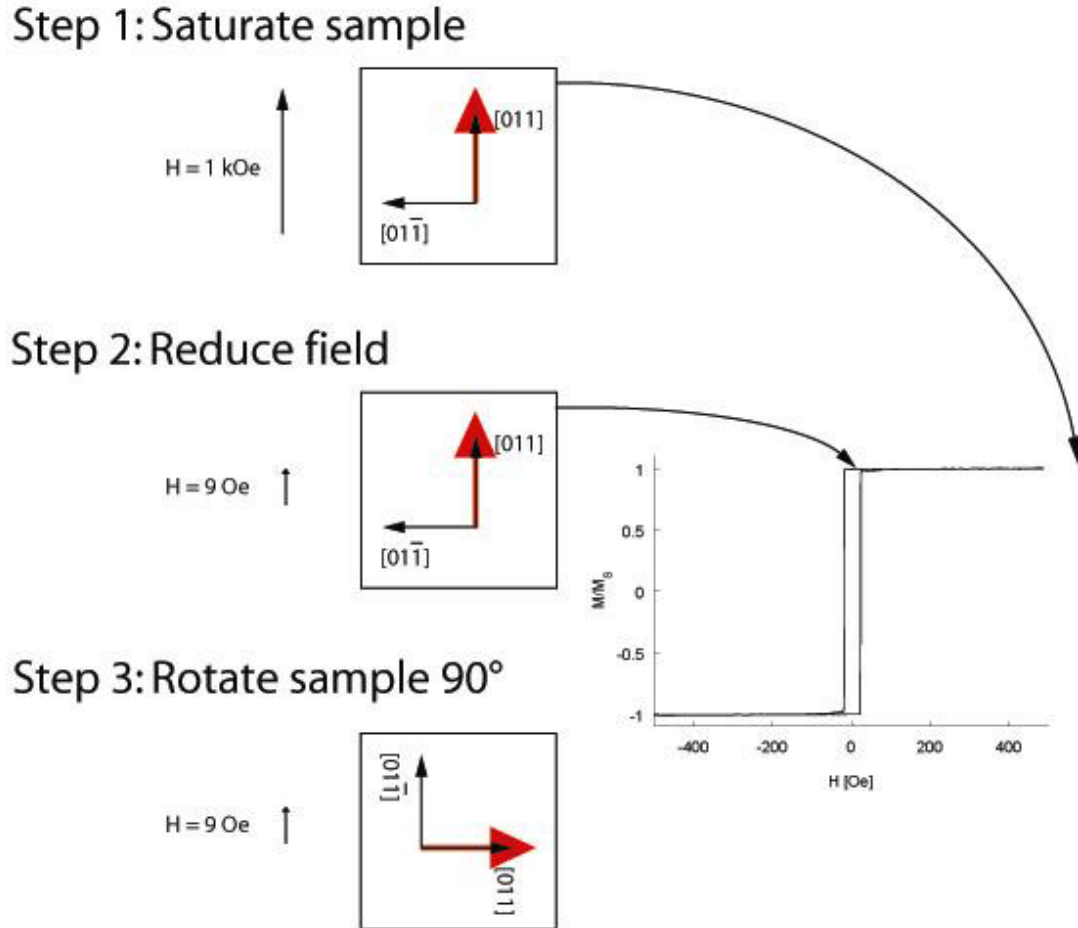


Figure 36 Procedure for preparing the magnetic history of the FeCo/GaAs sample prior to measurement with polarized neutrons. The magnetization of the sample is shown by the red arrow. The polarization of the neutron beam is parallel (or anti-parallel) to the applied field. The sample magnetization is first saturated, then the magnetic field is reduced to a small value—just large enough to maintain the polarization of the neutron beam, and finally the sample is rotated 90° about its surface normal, placing its magnetization perpendicular to the polarization axis of the neutron beam.

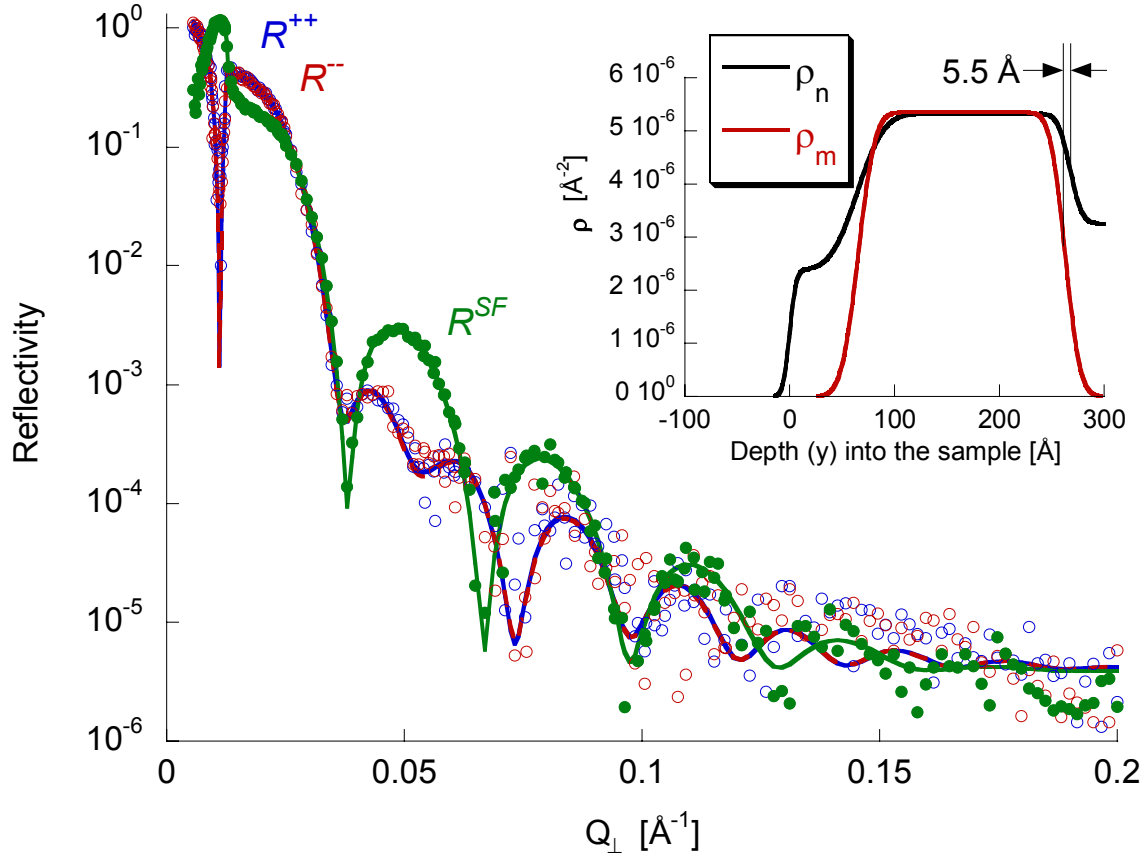


Figure 37 The polarized neutron reflectivities (symbols) of the FeCo/GaAs sample with its magnetization pointed along the neutron beam line (i.e., perpendicular to the applied field and in the plane of the sample) are shown. Note the R^{++} and R^{--} reflectivities are nearly superimposed. The fitted reflectivities (solid curves) were obtained from the nuclear and magnetic scattering length density profiles (inset). The magnetization vector has magnitude given by the magnetic component in the figure inset and a direction rotated about the surface normal from the applied field by an angle of 89.7° .

Table 6 Listing of guesses (v_0) and optimized parameters (v_{opt}) for nuclear magnetic models for the scattering length density profiles. Unless otherwise noted, values in the magnetic model were constrained to be the same as those in the nuclear model. The parameters were optimized between lower and upper limits, v_- and v_+ , respectively. If no limits are given the parameter was not optimized. The reflectivities contained 405 measurements.

Medium	Parameter	v_0	v_-	v_+	v_{opt}
(nuclear)	$\rho_n \times 10^{-6} [\text{\AA}^{-2}]$	0			0
	$\sigma_{01} [\text{\AA}^2]$	15.6	5	20	5.06

	$\Delta [\text{\AA}]$	0			0
Al-oxide (nuclear)	$\rho_n \times 10^{-6} [\text{\AA}^{-2}]$	2.36	2	4	2.37
	$\sigma_{01} [\text{\AA}^2]$	11.82	4	20	19.9
	$\Delta [\text{\AA}]$	65.46	60	70	64.6
FeCo (nuclear)	$\rho_n \times 10^{-6} [\text{\AA}^{-2}]$	5.01	4	6	5.32
	$\sigma_{01} [\text{\AA}^2]$	10.8	4	20	9.1
	$\Delta [\text{\AA}]$	200.9	190	210	202.9
GaAs (nuclear)	$\rho_n \times 10^{-6} [\text{\AA}^{-2}]$	3.10	2	4	3.26
Al-oxide (magnetic)	$\rho_m \times 10^{-6} [\text{\AA}^{-2}]$				
	$\sigma_{01} [\text{\AA}^2]$	11.82	5	20	12.65
	$\Delta [\text{\AA}]$				
FeCo (magnetic)	$\rho_m \times 10^{-6} [\text{\AA}^{-2}]$	5.0	4	6	5.36
	ϕ	$-\pi/2$	-1.6	-1.53	-1.565
	$\sigma_{01} [\text{\AA}^2]$	10.8	5	20	11.2
	$\Delta [\text{\AA}]$	197	190	210	197.4
GaAs (magnetic)	$\rho_m \times 10^{-6} [\text{\AA}^{-2}]$				

	$\chi^2(\nu = 391)$	3428			1511
--	---------------------	------	--	--	------

Summary and conclusions

The intent of this chapter is to provide a practical tutorial on polarized neutron reflectometry—one that provides reasonable limits to what can be learned from neutron reflectometry, a working knowledge of a polarized neutron reflectometer, a detailed understanding of how neutron scattering data are acquired and information obtained from the data, and a detailed worked example. Many other examples of solved problems exist in the literature, see for example Ref. [23] and references therein.

It is worth stressing the role polarized neutron reflectometry can play in solving problems involving artificially structured materials and nanomagnetism. Many sample fabrication techniques exist, *e.g.*, thin film growth, lithography, templating and self-assembly, to modulate the atomic, electronic and chemical structures of materials. Physical properties can be modulated via confinement in one, two or all dimensions to create multilayers, wires or dots that exhibit novel magnetic behavior. Confinement of physical structures can influence the magnetic properties of materials in ways that cannot be predicted from the averaging of constituent component properties, *e.g.*, giant magnetoresistance in Fe/Cr superlattices. These new nanocomposites are inhomogeneous materials with unique magnetic properties. To understand the magnetism of such artificially structured materials requires an understanding of the interplay between structure and magnetism at the nanometer length scale.

Because magnetism is inherently inhomogeneous in artificially structured materials, bulk probes, such as magnetometry, are ill-suited to provide information about the spatial variation of magnetization in non-homogeneous materials. Fortunately, the spatial length-scales of magnetism are precisely those that can be probed with neutron scattering. Particular strengths of polarized neutron reflectometry include its ability to measure the magnetic vector response of buried materials to extremes of magnetic and electric fields, temperature and (photon) irradiation. For example, polarized neutron reflectometry is a technique that can measure the depth dependent magnetization in thin films. Since polarized neutron reflectometry is inherently interface specific, the magnetization of the interfacial region can be measured with a great degree of accuracy in the presence of a strongly magnetic substrate. While not discussed in depth here, measurements of off-specular diffuse scattering in reflection geometry provide information about the lateral distribution of (inhomogeneous) magnetism across a sample surface or interface. For example, the lateral dimensions of magnetic domains can be determined from off-specular diffuse scattering and when these measurements are made as a function of Q_{\perp} , correlation lengths of lateral magnetic domains at one depth into the sample with those at another depth can be obtained. Other examples include characterizing the flow of magnetic induction around patterned holes (antidots) or correlation of magnetism between discrete but close by neighbors.

While many truly nanopatterned systems cannot be conveniently made in cm^2 size areas (necessary for study with neutron scattering) polarized neutron reflectometry may still provide important information to understand magnetism in model systems that replicate certain structural features, e.g., interfaces, in these systems. For example,

interest in ferromagnetic semiconductors is motivated by the prospect of spin-injection devices that *automatically imply the existence of buried interfaces* in the structures of interest. Characterization and understanding of interface quality is therefore a key issue for such devices to succeed. Here, polarized neutron reflectometry is expected to play an important role. For example, the flow of spin current, while most probably too small to be directly measured with neutron scattering, is profoundly affected by the magnetic properties of interfaces, which can be examined quite naturally with polarized neutron reflectometry.

Acknowledgments

The FeCo/GaAs sample and its magnetization data were kindly provided to us by X.Y. Dong, B.D. Schultz and C.J. Palmström (University of Minnesota). We thank S. Park (LANL) for the analyses of the X-ray and neutron data of the FeCo/GaAs sample. The polarizing supermirrors were made using facilities at the Paul Scherrer Institut provided to one of us (M.F.) by D. Clemens (HMI) and P. Böni (TU-München) for which we are grateful. We thank F. Mezi (HMI) for his advice, technical help and encouragement in the development of the polarization cavity and along with T. Keller (TU-München) and L. Mokrani (HMI) in the implementation of the radio-frequency gradient field spin flipper. Development of the polarized neutron reflectometer at LANSCE could not have been accomplished without the support of R. Pynn (LANL). This manuscript benefited greatly from vigorous discussions with G. Felcher (ANL), R. Pynn, I.K. Schuller (UCSD) and S. Sinha (UCSD). The neutron scattering facility of the Manuel Lujan Jr. Neutron Scattering Center is gratefully appreciated. The facility is

supported by the U.S. Department of Energy, BES-DMS under Contract No. W-7405-Eng-36.

Appendix 1: Instructions for using CO_REFINE

The computer program executable “co_refine.exe” optimizes parameters of a model subject to user-selectable bounds and constraints in order to minimize χ^2 [32, 70], a measure of error between measured and calculated reflectivities. The program requires one or more data files (in the absence of a data file, the program will produce only the X-ray and neutron reflectivities for the model structure), a file of model parameters and some user input. The program operates in a Windows environment.

Data file format

Data files consist of four columns of data separated by one or more spaces. The four columns are Q_{\perp} (in \AA^{-1}), R , σ_R^2 , and σ_Q^2 (in \AA^{-2}), respectively, where σ_R^2 is the variance on R and σ_Q^2 is the variance on Q_{\perp} (i.e., value of ΔQ^2 , see Equation 15). Q_{\perp} and σ_Q^2 should increase monotonically with row position. A portion of a data file is shown in Figure 38. CO_REFINE fits a model structure to X-ray, unpolarized neutron or polarized (NSF) neutron reflectivity data either separately, or X-ray data and one of either unpolarized or both polarized neutron reflectivities. The X-ray reflectivity curve must be named “pfn_xx.out”, where the choice of “pfn” is up to the user. Likewise the unpolarized neutron reflectivities or the spin-up and spin-down polarized neutron reflectivities are “pfn_uu.out”, or “pfn_pp.out” and “pfn_mm.out”, respectively. The maximum number of rows or values of Q_{\perp} is 3000.

Column 1	Column 2	Column 3	Column 4
5.1122247e-003	9.6100998e-001	3.8228720e-002	4.3366516e-008
5.3204708e-003	1.0199195e+000	3.7366647e-002	4.3366420e-008
5.5287168e-003	1.0813725e+000	3.0592421e-002	4.3366516e-008
5.7369634e-003	1.0186689e+000	2.1379778e-002	4.3366516e-008
5.9452094e-003	1.0323699e+000	1.5872519e-002	4.3366516e-008
6.1534559e-003	1.0648947e+000	1.2950795e-002	4.3366516e-008
6.3617020e-003	1.0213364e+000	9.6741142e-003	4.3366420e-008
6.5699480e-003	1.0496752e+000	8.3177052e-003	4.3366516e-008
6.7781946e-003	1.0427407e+000	6.4306096e-003	4.3366516e-008
6.9864406e-003	1.0553303e+000	5.6308783e-003	4.3366420e-008
7.1946867e-003	1.0129898e+000	4.4487622e-003	4.3366516e-008
7.4029332e-003	1.0402484e+000	3.9526848e-003	4.3366516e-008
7.6111793e-003	1.0133827e+000	3.3225839e-003	4.3366420e-008
7.8194253e-003	1.0274578e+000	2.9229610e-003	4.3366516e-008
8.0276718e-003	1.0251300e+000	2.5576549e-003	4.3366615e-008
8.2359184e-003	9.8727781e-001	2.1498785e-003	4.3366420e-008
8.4441639e-003	1.0218128e+000	1.9088250e-003	4.3366420e-008
8.6524105e-003	9.7317237e-001	1.6977043e-003	4.3366615e-008
8.8606570e-003	9.9624068e-001	1.5935383e-003	4.3366420e-008
9.0689026e-003	1.0079406e+000	1.3910802e-003	4.3366420e-008
9.2771491e-003	9.7570157e-001	1.2412651e-003	4.3366615e-008
9.3379403e-003	1.0466228e+000	1.2489481e-002	1.9071580e-007

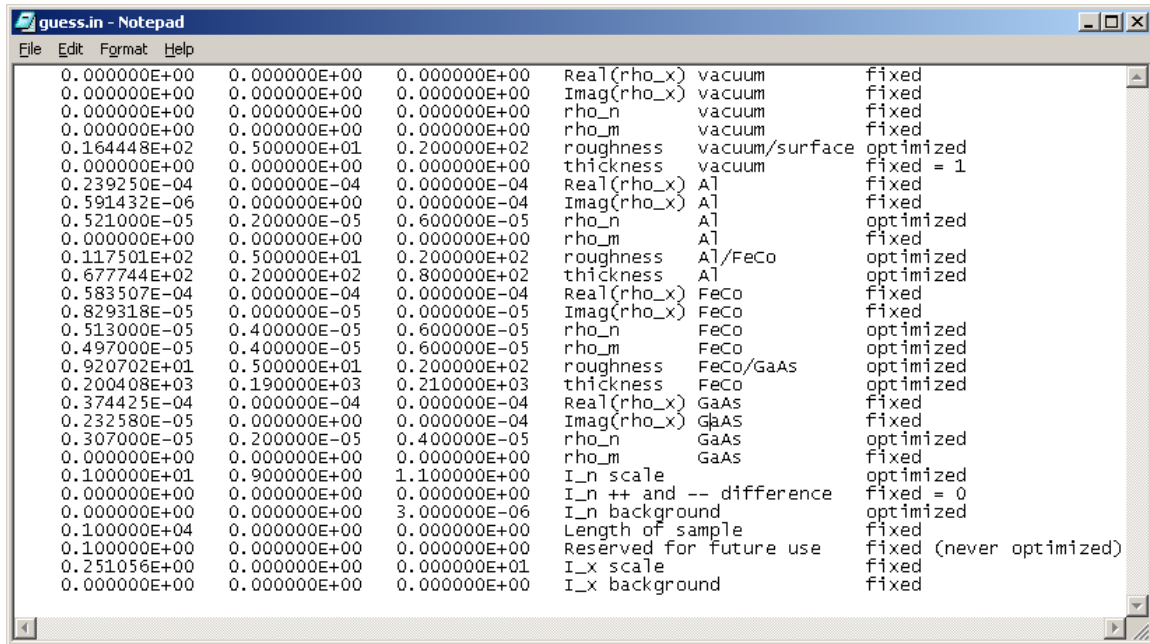
Figure 38 The first few entries of the polarized neutron data file “feco_pp.out” containing the spin-up neutron reflectivity. The columns are Q_{\perp} (in \AA^{-1}), R , σ_R^2 , and σ_Q^2 (in \AA^{-2}), respectively.

Model (or guess) file format

The model whose calculated reflectivity curves are fitted to the data consists of a sequence of layers (or films) on a substrate. Each layer is characterized by six parameters. For the j -th layer, the parameters are $\text{Real}(\rho_{xj})$, $\text{Imag}(\rho_{xj})$, ρ_{nj} , ρ_{mj} (all ρ 's are in units of \AA^{-2}), interface roughness between the j -th and $j+1$ -th layer [in \AA (rms)], and the thickness of the j -th layer (in \AA). The first layer is considered to be the surrounding medium, which is typically vacuum or air. The roughness parameter for this layer is the surface roughness of the sample. The thickness of the first layer is irrelevant (because it introduces only a phase factor), its thickness is zero.

The parameters of the model are tabulated in a three-column (separated by a space or spaces) format. The first column contains the value for the particular parameter, and

the next two columns are the lower and upper bounds, respectively, within which CO_REFINE will determine the value that yields a local (and hopefully a global) minimum of χ^2 . If no optimization of the parameter is desired, then the lower and upper limits should be equal. For example, if optimization of a model to only unpolarized neutron data is desired, then the lower and upper limits should be equal for all parameters involving $\text{Real}(\rho_{xj})$, $\text{Imag}(\rho_{xj})$, and ρ_{mj} . The maximum number of layers is 83 (excluding the substrate). A simple example of a model file describing a two-layer structure of Al on FeCo is shown in Figure 39.



0.000000E+00	0.000000E+00	0.000000E+00	Real(rho_x)	vacuum	fixed
0.000000E+00	0.000000E+00	0.000000E+00	Imag(rho_x)	vacuum	fixed
0.000000E+00	0.000000E+00	0.000000E+00	rho_n	vacuum	fixed
0.000000E+00	0.000000E+00	0.000000E+00	rho_m	vacuum	fixed
0.164448E+02	0.500000E+01	0.200000E+02	roughness	vacuum/surface	optimized
0.000000E+00	0.000000E+00	0.000000E+00	thickness	vacuum	fixed = 1
0.239250E-04	0.000000E-04	0.000000E-04	Real(rho_x)	Al	fixed
0.591432E-06	0.000000E+00	0.000000E-04	Imag(rho_x)	Al	fixed
0.521000E-05	0.200000E-05	0.600000E-05	rho_n	Al	optimized
0.000000E+00	0.000000E+00	0.000000E+00	rho_m	Al	fixed
0.117501E+02	0.500000E+01	0.200000E+02	roughness	Al/FeCo	optimized
0.677744E+02	0.200000E+02	0.800000E+02	thickness	Al	optimized
0.583507E-04	0.000000E-04	0.000000E-04	Real(rho_x)	FeCo	fixed
0.829318E-05	0.000000E-05	0.000000E-05	Imag(rho_x)	FeCo	fixed
0.513000E-05	0.400000E-05	0.600000E-05	rho_n	FeCo	optimized
0.497000E-05	0.400000E-05	0.600000E-05	rho_m	FeCo	optimized
0.920702E+01	0.500000E+01	0.200000E+02	roughness	FeCo/GaAs	optimized
0.200408E+03	0.190000E+03	0.210000E+03	thickness	FeCo	optimized
0.374425E-04	0.000000E-04	0.000000E-04	Real(rho_x)	GaAs	fixed
0.232580E-05	0.000000E+00	0.000000E-04	Imag(rho_x)	GaAs	fixed
0.307000E-05	0.200000E-05	0.400000E-05	rho_n	GaAs	optimized
0.000000E+00	0.000000E+00	0.000000E+00	rho_m	GaAs	fixed
0.100000E+01	0.900000E+00	1.100000E+00	I_n scale		optimized
0.000000E+00	0.000000E+00	0.000000E+00	I_n ++ and -- difference		fixed = 0
0.000000E+00	0.000000E+00	3.000000E-06	I_n background		optimized
0.100000E+04	0.000000E+00	0.000000E+00	Length of sample		fixed
0.100000E+00	0.000000E+00	0.000000E+00	Reserved for future use		fixed (never optimized)
0.251056E+00	0.000000E+00	0.000000E+01	I_x scale		fixed
0.000000E+00	0.000000E+00	0.000000E+00	I_x background		fixed

Figure 39 A model or guess file containing initial values for the different model parameters (first column) and the lower and upper bounds limiting optimization of the parameters. X-ray parameters are not optimized in this example, since this particular guess file is intended for fitting to only neutron data. Only the first three columns are required by CO_REFINE.

After the parameters for the layers, the next four parameters in the model file consist of values of $\text{Real}(\rho_x)$, $\text{Imag}(\rho_x)$, ρ_j , ρ_m for the substrate. The layer and substrate parameters are needed to calculate the depth dependence of the X-ray and/or neutron

scattering length densities. At the conclusion of the program, the scattering length density profiles are written to a file called “beta.out”. This file contains seven columns consisting of y-depth (in Å), $\text{Real}(\rho_x)$, $\text{Imag}(\rho_x)$, ρ_{-} , a “0”, ρ_{++} , and a “0” (again all ρ ’s are in units of Å⁻²).

Once the reflectivity curves are calculated, they are normalized to scale factors and a factor to account for Q_{\perp} -independent background (discussed later). These parameters are found in the last seven entries of Figure 39. The first three of the last seven parameters are applied to the calculated neutron reflectivities. They consist of a neutron scale factor, I_n^0 , (typically a value close to one, since conventionally the measured reflectivity curve is normalized to unity below the critical edge), a scale factor to account for a difference between the scale factors for spin-up and spin-down reflectivity curves, I_n^{Δ} , (this difference should be zero), and instrumental neutron background, I_n^B , (typically on order of 10^{-7} or 10^{-6}) that is treated as if it were independent of Q_{\perp} . The last four parameters are applied to the calculated X-ray reflectivity. The first is the length of the sample (in mm) (This parameter is used to calculate the variation of the reflectivity arising from the fraction of the X-ray beam subtended by the sample footprint as the sample angle is changed. To turn off the footprint correction, use a large value for the parameter, e.g., 1000. A footprint correction is not applied to neutron reflectivities because samples are typically always bathed in the neutron beam, and consequently the $1/\alpha_i$ -dependence is usually removed from the data before fitting.) The second parameter is reserved for future use. Set this

parameter to 1 and do not optimize it. The last two parameters are the normalization, I_x^0 , and background, I_n^B , factors.

CO_REFINE

The program CO_REFINE uses the parameters in the model (or guess) file to calculate X-ray and neutron scattering length density profiles as described in the text. The program then uses the dynamical recursive algorithm (the Parratt formalism described in the text) to calculate the reflectivity curve. The curve is calculated between Q_{\min} and Q_{\max} that extend beyond the measured range of Q_{\perp} in steps, Q_{step} , determined by the distance between the first two measurements of Q_{\perp} in the data file (thus the user has control over the step size by choosing the first two steps in Q_{\perp}). Not only must the number of measurements be less than 3000, but the number of points equal to $(Q_{\max} - Q_{\min})/Q_{\text{step}}$ must also be less than 3000 (effectively reducing the number of measurements to a value less than 3000).

Next, the convolution of the reflectivity curve and a Gaussian function with width given by σ_Q is computed. The result is a reflectivity curve that is compared to the experimental data by calculating χ^2 . The curve yielding a minimum of χ^2 is sought by the optimization routine in co_refine. After minimizing χ^2 , the program writes the scattering length density profile to a file called “beta.out”, and the best fitting reflectivity curves to “pfn_xx.fit”, “pfn_uu.fit” or “pfn_pp.fit” and “pfn_mm.fit”. The files containing the fitted curves consist of four columns, Q_{\perp} , $R(\text{fitted})$, $R(\text{observed})$, and $\sigma_R(\text{observed})$. Finally, a third file listing the values of the optimized model are written to a file of the user’s choice. This parameter-listing file is written with the same format as

the guess file with additional data describing the quality of the fit, the number of data points, etc., appended to the file. The parameter file can be used as a model or guess file after removal of the additional data (i.e., the last 11 lines). An example of a parameter file is shown in Figure 40.

```

0.000000E+00 0.000000E+00 0.000000E+00 1 0.000000E+00 0.000000E+00
0.000000E+00 0.000000E+00 0.000000E+00 1 0.000000E+00 0.000000E+00
0.000000E+00 0.000000E+00 0.000000E+00 1 0.000000E+00 0.000000E+00
0.000000E+00 0.000000E+00 0.000000E+00 1 0.000000E+00 0.000000E+00
0.106449E+02 0.500000E+01 0.200000E+02 0 0.355148E+00 -0.324100E+00
0.000000E+00 0.000000E+00 0.000000E+00 1 0.000000E+00 0.000000E+00
0.239250E-04 0.000000E+00 0.000000E+00 1 0.000000E+00 0.000000E+00
0.591432E-06 0.000000E+00 0.000000E+00 1 0.000000E+00 0.000000E+00
0.236278E-05 0.200000E-05 0.600000E-05 0 0.223120E-07 0.222513E-07
0.000000E+00 0.000000E+00 0.000000E+00 1 0.000000E+00 0.000000E+00
0.107722E+02 0.500000E+01 0.200000E+02 0 -0.101784E+00 0.126785E+00
0.627274E+02 0.200000E+02 0.800000E+02 0 0.318452E+00 0.317833E+00
0.583507E-04 0.000000E+00 0.000000E+00 1 0.000000E+00 0.000000E+00
0.829318E-05 0.000000E+00 0.000000E+00 1 0.000000E+00 0.000000E+00
0.493778E-05 0.400000E-05 0.600000E-05 0 0.132042E-07 -0.122070E-07
0.503551E-05 0.400000E-05 0.600000E-05 0 -0.125964E-07 -0.129875E-07
0.120010E+02 0.500000E+01 0.200000E+02 0 -0.135685E+00 0.142577E+00
0.197472E+03 0.190000E+03 0.210000E+03 0 0.141734E+00 0.147774E+00
0.374425E-04 0.000000E+00 0.000000E+00 1 0.000000E+00 0.000000E+00
0.232580E-05 0.000000E+00 0.000000E+00 1 0.000000E+00 0.000000E+00
0.307297E-05 0.200000E-05 0.400000E-05 0 0.146953E-07 0.146845E-07
0.000000E+00 0.000000E+00 0.000000E+00 1 0.000000E+00 0.000000E+00
0.972123E+00 0.900000E+00 0.110000E+01 0 -0.290289E-02 0.270815E-02
0.000000E+00 0.000000E+00 0.000000E+00 1 0.000000E+00 0.000000E+00
0.317160E-06 0.000000E+00 0.300000E-05 0 -0.781106E-07 0.737247E-07
0.100000E+04 0.000000E+00 0.000000E+00 1 0.000000E+00 0.000000E+00
0.100000E+00 0.000000E+00 0.000000E+00 1 0.000000E+00 0.000000E+00
0.251056E+00 0.000000E+00 0.000000E+00 1 0.000000E+00 0.000000E+00
0.000000E+00 0.000000E+00 0.000000E+00 1 0.000000E+00 0.000000E+00
NUMBER OF FITTED DATA POINTS = 174 174
NUMBER OF FITTED PARAMETERS = 11
CHISQR, CHISQR(REDUCED) USED IN FITTING = 0.1102E+04 0.3270E+01
REAL CHISQR, CHISQR(REDUCED) = 0.1102E+04 0.3270E+01
CHI_SPIN = 0.000000E+00 0.234266E+03 0.867885E+03
PROBABILITY = INF
VALUE OF CONSTANT USED IN PROBABILITY = 0.1000E+01
DETERMINANT OF THE HESSIAN MATRIX = 0.0000E+00
COMPILED BOUND = 0.4000E-03
IMSL OPTIMIZATION ERROR FLAG = 0
WEIGHTING SCHEME = 1.

```

Figure 40 A listing of the optimized parameters of a model. The optimized parameters are in the first column. The second and third columns show the lower and upper bounds limiting the optimization. The fourth column indicates whether a parameter was optimized (= 0), held fixed (= 1) or in the case of a negative number, constrained to equal the value of another parameter (see text). The final two columns show perturbations to the optimized value in the first column that increase χ^2 by 1, corresponding to a 1- σ error. The information below the columns must be deleted before the parameter listing can be used as a model file for a new optimization. The values of χ^2 and χ^2 reduced by the number of data points minus the number of fitted parameters are indicated in the information block. The contributions to χ^2 from the X-ray, spin-down and spin-up neutron data are shown in the part of the information block labeled “chi_spin”, respectively.

Tips for successful fitting

- (1) Be certain the data are worthy of analysis. Model fitting is often time consuming and tedious. Data that are free of systematic errors are usually easier to fit than data that are fundamentally compromised.
- (2) If possible obtain information about the sample from other sources, either from other measurements or the literature. Use this information in formulating sound initial guesses.
- (3) Try fitting just a few parameters at first, and as these parameters become optimized add new parameters to the fitting process. Fitting is often an iterative procedure.
- (4) Consider fitting only a portion of the data, e.g., data for small Q_{\perp} , to obtain better guesses, before fitting all the data. Or, consider fitting X-ray data before fitting X-ray and neutron data together. Or, consider fitting data from two spin states separately (e.g., by renaming the files as unpolarized data files “_uu”). By comparing the scattering length density profiles from separately fitted data files, sometimes a “universal” model can be developed.
- (5) At the conclusion of a successful fitting exercise, the sensitivity of model parameters to fitted reflectivity curve should be tested by making perturbations to the parameters. In this way one can determine the relative importance of the different parameters.
- (6) Use a fast computer and be patient!

A worked example using CO_REFINE

The CO_REFINE executable, an example of a guess file (guess.in) and the X-ray and neutron data appearing in Figure 35 are located in the co_refine directory of the attached compact disk. Output displayed during execution of the program is shown in Figure 41, Figure 42, and Figure 43.

One feature of the program that is not shown in the figures is the use of constraints. Parameters can be constrained to have the same values and then to be collectively optimized. This feature is useful optimizing a model with many parameters, e.g., as needed to describe a superlattice. For example, one might wish to constrain the roughness of every interface (or layer thickness, etc.) to be the same value, but this value would be subject to optimization. In this example, every fifth parameter in the guess file is a roughness parameter, so to optimize the roughness of all interfaces collectively, the usual lower and upper bounds are assigned to one of the roughness parameters, e.g., the 10th parameter, and the rest are constrained to it. Constraints are imposed by answering “Y” when prompted by the program: “Are there any constraints [N]?”. Next, pairs of parameters that are to be constrained are specified, such as 5, 10 which constrains the 5th parameter to have the value of the 10th, then 15, 10, etc., until no more pairs are to be constrained (at which point a blank line is returned). In this example lower and upper bounds would be specified in the guess input file for the 10th parameter.

```

C:\WINNT\System32\cmd.exe
Microsoft Windows 2000 [Version 5.00.2195]
(C) Copyright 1985-2000 Microsoft Corp.
C:\>cd co_refine
C:\co_refine>co_refine
CO_POLAR_SPEC: VERSION 1.0 10.06.94MF
POLARIZED OR UNPOLARIZED NEUTRON MEASUREMENTS [U]? p
WHAT IS THE NAME OF THE DATA FILE? feco
CHOICES FOR WEIGHTING:
-1 = DB WEIGHTED FIT
0 = UNWEIGHTED FIT
M = WEIGHT TO THE POWER OF M, M=1 IS TRADITIONAL
WEIGHTING CHOICE: 1
GET_DATA: 134 DATA POINTS FOUND IN: feco_XX.OUT
NUMBER OF OBSERVABLES: 1 134
SPANNING RANGE: 3.27200000000000E-002 0.231890000000000
NUMBER OF CALCULATED POINTS: 1 727
SPANNING RANGE: 4.73326666666666E-004 0.344112848666666
GET_DATA: 174 DATA POINTS FOUND IN: feco_MM.OUT
NUMBER OF OBSERVABLES: 2 174
SPANNING RANGE: 5.11222470000000E-003 0.238842370000000
NUMBER OF CALCULATED POINTS: 2 1028
SPANNING RANGE: 6.94153666666666E-005 0.443425362266663
GET_DATA: 174 DATA POINTS FOUND IN: feco_PP.OUT
NUMBER OF OBSERVABLES: 3 174
SPANNING RANGE: 5.11222470000000E-003 0.238842370000000
NUMBER OF CALCULATED POINTS: 3 1028
SPANNING RANGE: 6.94153666666666E-005 0.443425362266663
NAME OF FILE TO CONTAIN CALCULATED PROFILE? feco
NAME OF OUTPUT PARAMETER FILE: feco.para
X-RAY WAVELENGTH: 1.54178
NAME OF FILE-OF-GUESSES: guess.in
ARE THERE CONSTRAINTS [N]? n
CO_POLAR_SPEC: CHISQR = 1643.61878206233
DO YOU WANT MINIMIZATION [N]? y
1 1.56147000000000 0.500000000000000 2.00000000000000
2 2.16617005472206 2.00000005052425 3.00000007578638
3 0.810825002047136 0.000000000000000 1.00000000252476
4 2.67709000675900 2.00000000504951 6.00000001514854
5 1.18199000000000 0.500000000000000 2.00000000000000
6 0.654628000000000 0.600000000000000 0.700000000000000
7 0.575275014532669 0.500000012631063 0.600000015157275
8 0.716638018103799 0.000000000000000 1.00000002526213
9 0.500899012653773 0.400000010104850 0.600000015157275
10 0.500082012633134 0.400000010104850 0.600000015157275
11 1.07711000000000 0.500000000000000 2.00000000000000
12 0.513470012971344 0.300000007578638 0.600000015157275
13 3.08579000779087 0.000000000000000 10.0000000252476
14 0.612289015467721 0.300000007578638 0.700000017683488
15 0.930544005655354 0.000000000000000 600.000003646483
16 0.762687000000000 0.500000000000000 2.00000000000000
17 0.384357009709675 0.300000007578638 0.400000010104850
18 2.34511000592083 2.00000000504951 3.00000000757427
19 3.10139000783026 2.00000000504951 4.00000001009903
20 0.961899000000000 0.900000000000000 1.10000000000000
21 2.21135997415783 0.000000000000000 2.99999996494171
22 1.00000000000000 0.800000000000000 1.20000000000000
POWELL [P].
QUASI-NEWTON [Q].
LEAST SQUARES [L] MINIMIZATION, OR
HESSIAN MATRIX CALCULATION [H]? p
CHISQR = 1643.61878206233
OPTIMIZE: PERFORMING POWELL OPTIMIZATION.
0.1611E+04 OPTIMIZE: PARAMETERS AFTER OPTIMIZATION.
0.000000000000000

```

Figure 41 Invocation of co_refine and examples of user input to run the program are shown. The weighting choice of “1” is used to achieve a local minimum in χ^2 . The choice of “-1” imposes a logarithmic weighting scheme on the errors that more heavily weights measurements at large Q_{\perp} than at small Q_{\perp} . After selection of the weighting scheme, the range in Q_{\perp} over which the reflectivity is calculated is given (in comparing to the data, interpolations of the calculated curve to the measured values of Q_{\perp} are made) and the number of calculated points is reported. The number of calculated points must be less than 3000.

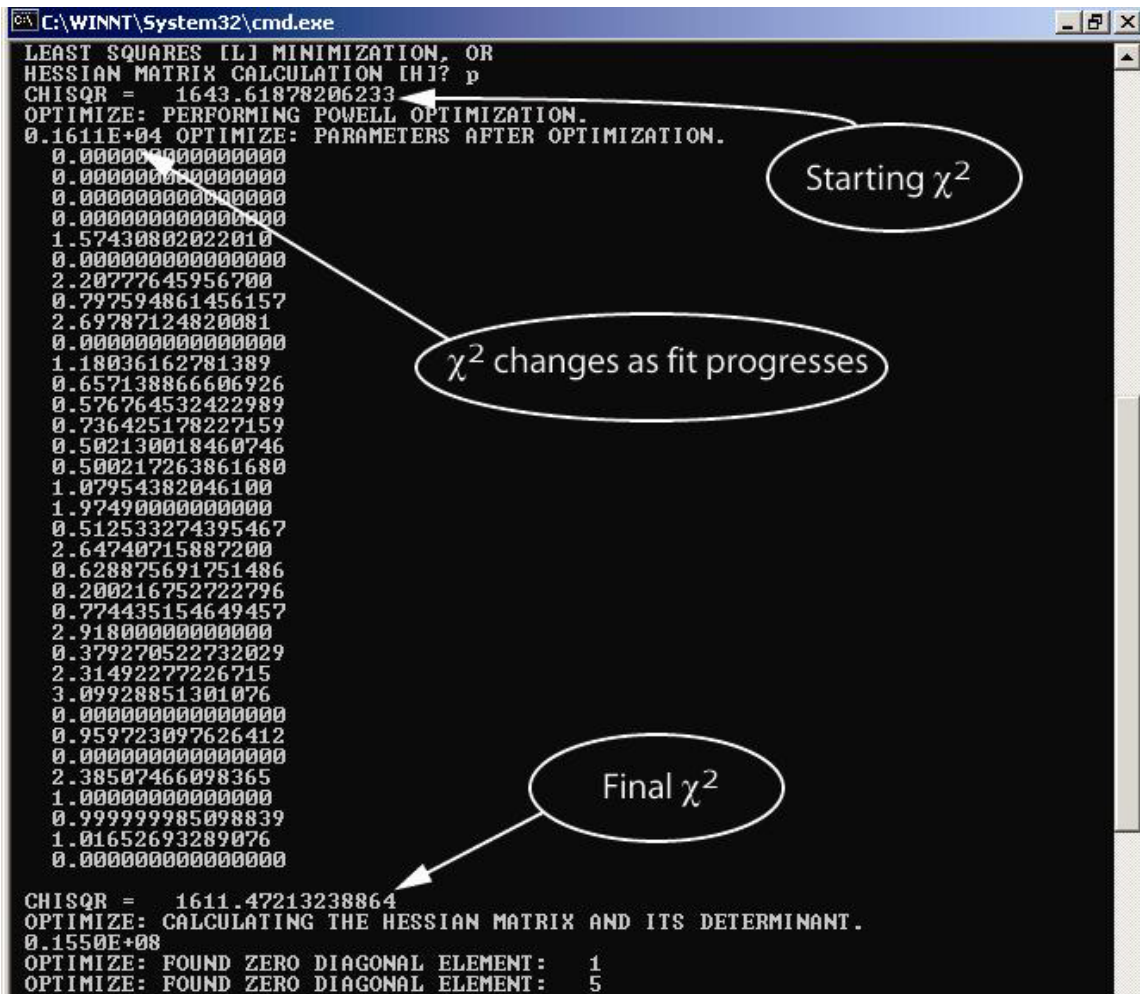


Figure 42 The values of χ^2 before and after optimization are shown.



Figure 43 The reduced value of χ^2 and the contributions to χ^2 from the fit to the X-ray and polarized neutron data are reported at the conclusion of the program.

Appendix 2: Instructions for using SPIN_FLIP

In contrast to the computer program CO_REFINE, which calculates the two non-spin-flip reflectivities R^{++} and R^- using a scalar scattering potential, the computer program SPIN_FLIP generates the vector scattering potential from which the non-spin-flip and spin-flip, R^{SF} , reflectivities are calculated with the aid of the subroutine, GEPORE [28].

Besides the capability to treat the net magnetization vector depth dependence of a sample (the sample magnetization is treated as if it were a single domain laterally), SPIN_FLIP can generate the nuclear and magnetic scattering length density profiles from a single model (like CO_REFINE), or use two models to generate the nuclear and magnetic potentials separately. Even for instances in which SF scattering is not observed (and a scalar potential would suffice), the SPIN_FLIP program offers the opportunity to characterize the magnetic structure of an interface differently from that of its nuclear structure. This feature is useful for fitting a model system in which the magnetic roughness of an interface differs from its and chemical roughness [71].

Data file format

The four-column data file format used by CO_REFINE is also needed by SPIN_FLIP. Three data files are required, “pfn_pp.out”, “pfn_mm.out”, and “pfn_sf.out” that contain the R^{++} , R^- and R^{SF} reflectivities, respectively. The maximum number of data points is 7000.

Model (or guess) file format

The three-column format containing a column of parameter values and lower and upper bounds used by CO_REFINE is required for SPIN_FLIP. After the first row, which simply contains the word “MODEL”, layers are parameterized by ρ_n , ρ_m , ϕ (the angle of between the layer magnetization and the applied field), σ , and layer thickness, Δ . Valid values of ϕ are those between -2π and $\pi/2$. The maximum number of layers is 203. Following the parameters for the layers, are the three parameters ρ_n , ρ_m , ϕ for the substrate, then I_n^0 and I_n^B .

For refinements involving one model, the nuclear and magnetic structures are provided in a single model file. Even though parameters for the magnetic structure of the sample can be included in the file (and optimized), this guess file is called the chemical file. For refinements involving a nuclear model that is possibly different from the magnetic model, the parameters of the nuclear model are given in the chemical file (an example is shown in Figure 44), and the parameters of the magnetic model, which may include values of ρ_m , ϕ , σ , or Δ for different layers, are given in the second file (called the magnetic guess file, see Figure 45) and supercede those in the first if different.

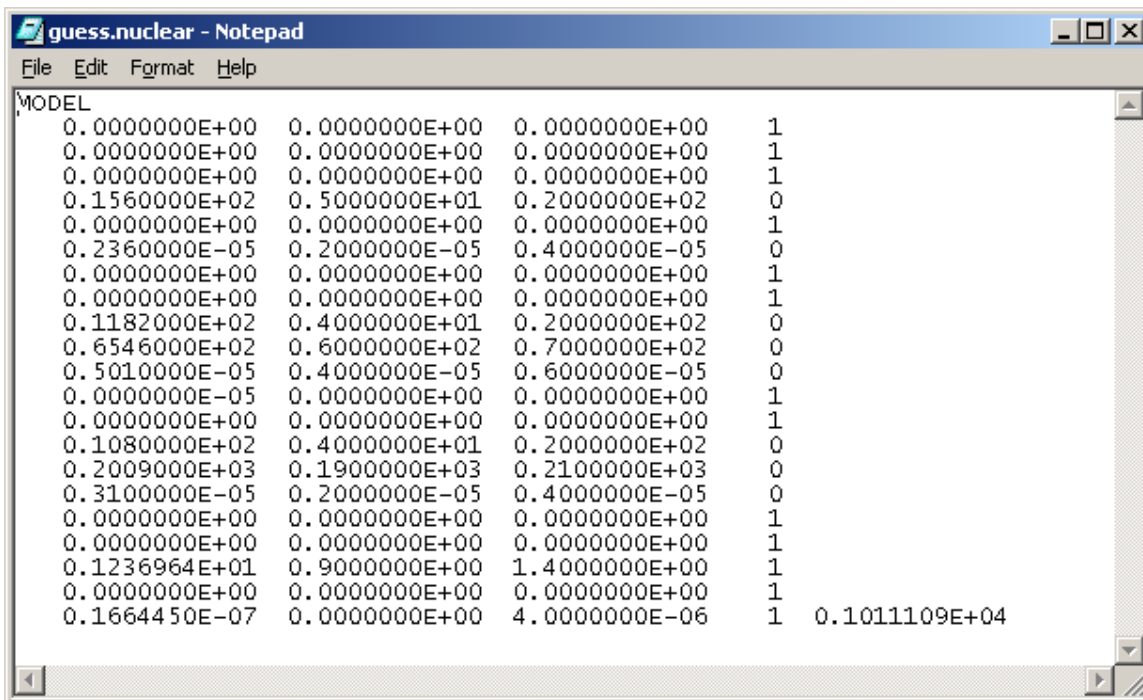


Figure 44 An example of a file containing guess parameters that describe the chemical or nuclear scattering length density profiles of the FeCo/GaAs sample. Information about the magnetic structure of the sample can also be included in the chemical guess file. The chemical guess file is required for operation of SPIN_FLIP.

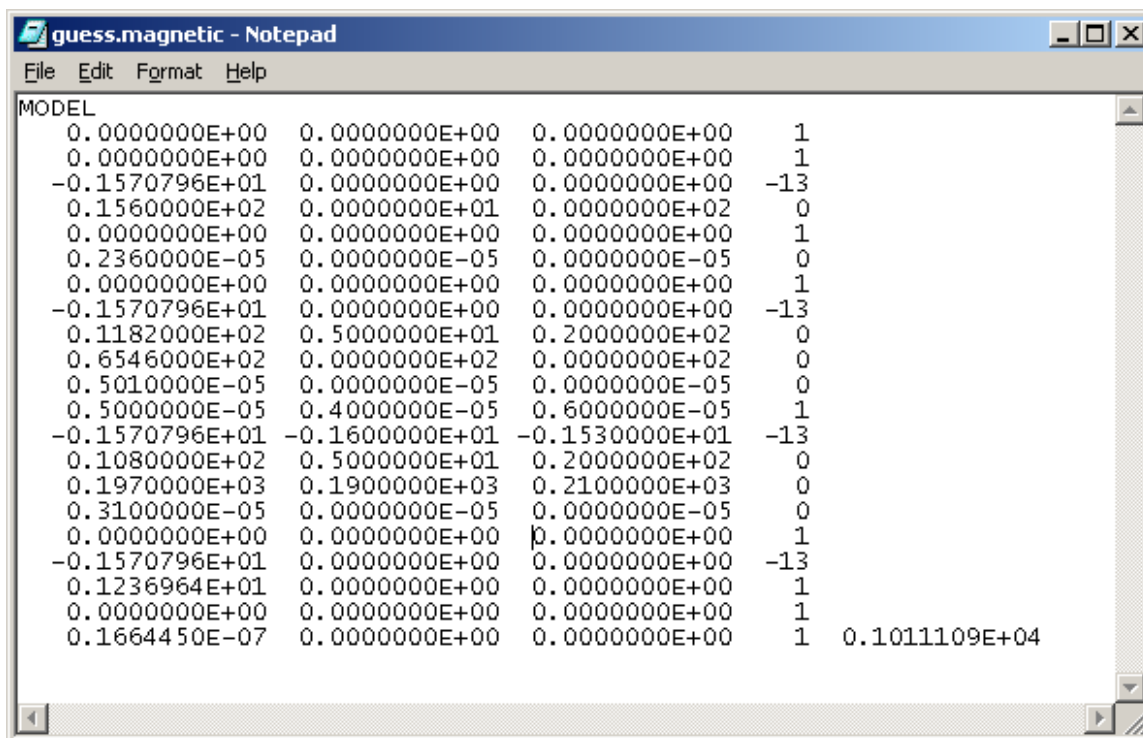


Figure 45 An example of a file containing guess parameters that describe the magnetic scattering length density profile of the FeCo/GaAs sample. The magnetic guess file is optional for operation for SPIN_FLIP. Two guess files, chemical and magnetic files, are required in simulations in which the chemical and magnetic structures of a sample are not necessarily commensurate.

A worked example using SPIN_FLIP

Operation of SPIN_FLIP is nearly identical to that of CO_REFINE. Examples of guess files, containing nuclear and magnetic parameters in one file (guess.joint), and in separate files (guess.nuclear and guess.magnetic) are located in the spin_flip directory of the attached compact disk. Neutron data appearing in Figure 37 are also located in this directory. In calculating the scattering length density profiles, SPIN_FLIP like CO_REFINE uses the parameters in the guess files to construct Gaussian profiles that comprise the derivatives of the nuclear and magnetic density profiles with depth. The same technique is also used to compute the depth profile of $\phi(y)$ —the angle between the applied field and the sample magnetization. In other words, if $\phi = -\pi/2$ were specified for the FeCo layer and is 0 elsewhere, then at the Al/FeCo interface and the FeCo/GaAs

interface, not only would the magnitude of the FeCo magnetization increase as the FeCo layer is approached (an increase determined by the magnetic roughness of the interface), but the direction of the magnetization would rotate (in the sample plane) from 0° to 90° to the applied field as well. For some systems, the twisting of ϕ might be desirable, but for the case of representing the magnetization of FeCo/GaAs, twisting was not desired. Twisting magnetization can be avoided by constraining ϕ for every layer to be the same (and then optimizing one of values of ϕ , if desired) using the method of constraints discussed in the previous section.

SPIN_FLIP can be invoked and information fed into the program interactively, or information can be fed into the program from a command file (this mode of operation is also possible with CO_REFINE). For example, information from the file “job.txt” (see Figure 46) containing information needed by SPIN_FLIP, is fed to the program by typing the command line “SPIN_FLIP < job.txt”. Use of constraints is also shown in the figure. An example of execution of SPIN_FLIP is shown in Figure 47.

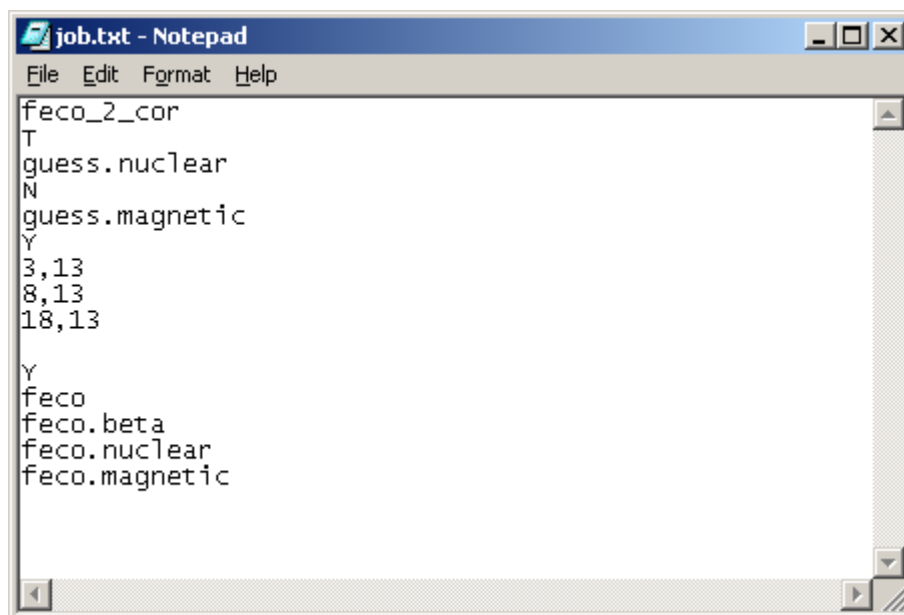


Figure 46 File containing information needed to run SPIN_FLIP. The information can be supplied interactively or a file containing the information can be fed into SPIN_FLIP. An example of the use of constraints is shown in this example. Here, the values of ϕ (see text) for the first, second and substrate layers are constrained to be the same as the value of ϕ for the third layer (i.e., parameter number 13).

```

C:\WINNT\System32\cmd.exe - spin_flip
Microsoft Windows 2000 [Version 5.00.2195]
(C) Copyright 1985-2000 Microsoft Corp.

C:\>cd spin_flip

C:\spin_flip>spin_flip
WHAT IS THE NAME OF THE DATA FILE? feco_2
TRADITIONAL (T), MODIFIED (M) OR DB (D) [T]:
GET_DATA: FOUND 216 DATA POINTS FOR ++ SP
GET_DATA: FOUND 216 DATA POINTS FOR -- SP
GET_DATA: FOUND 216 DATA POINTS FOR SF SPIN STATE.
GET_DATA: SIG_BAR SET TO 1 FOR 1 SIGMA RESOLUTION BARS.
GET_GUESS: PROGRAM REQUIRES A CHEMICAL PROFILE
GET_GUESS: GUESS FILE- THE MAGNETIC PROFILE IS OPTIONAL.
NAME OF CHEMICAL GUESS PROFILE: guess.nuclear
ARE THERE CONSTRAINTS [N]? n
GET_GUESS: FOUND 21 PARAMETERS.
GET_GUESS: 10 PARAMETERS TO OPTIMIZE.
NAME OF MAGNETIC GUESS PROFILE: guess.magnetic
ARE THERE CONSTRAINTS [N]? n
GET_GUESS: FOUND 21 MAGNETIC PARAMETERS.
GET_GUESS: 5 MAGNETIC PARAMETERS TO OPTIMIZE.
0.4208E+04 SPIN_FLIP: CHISQR = 4207.94248764401
DO YOU WANT TO OPTIMIZE THE PARAMETERS [N]? y
0.4208E+04 OPTIMIZE: CHISQR = 4207.94248764401
OPTIMIZE: NUMBER OF CHEMICAL VARIABLES TO OPTIMIZE: 10
OPTIMIZE: NUMBER OF MAGNETIC VARIABLES TO OPTIMIZE: 5
OPTIMIZE: PERFORMING POWELL OPTIMIZATION.
INITIAL GUESSES:
1 15.600000000000 5.000000000000 20.000000000000
2 2.360000000000E-006 2.000000000000E-006 4.000000000000E-006
3 11.820000000000 4.000000000000 20.000000000000
4 65.460000000000 60.000000000000 70.000000000000
5 5.010000000000E-006 4.000000000000E-006 6.000000000000E-006
6 10.800000000000 4.000000000000 20.000000000000
7 200.900000000000 190.000000000000 210.000000000000
8 3.100000000000E-006 2.000000000000E-006 4.000000000000E-006
9 1.236764000000 0.900000000000 1.400000000000
10 1.664450000000E-008 0.000000000000 4.000000000000E-006
11 11.820000000000 5.000000000000 20.000000000000
12 5.000000000000E-006 4.000000000000E-006 6.000000000000E-006
13 -1.570796000000 -1.600000000000 -1.5300000000
14 10.800000000000 5.000000000000 20.00000000
15 197.000000000000 190.000000000000 210.000000
BEGINNING CHISQR: 4207.94248764401
0.1590E+04

```

name of the nuclear guess file is "guess.nuclear", and no nuclear-parameters are constrained.

χ^2 updated during optimization

Figure 47 Invocation of the SPIN_FLIP program is shown. After optimization is complete (this figure shows SPIN_FLIP during optimization) the user is queried for names of files to contain the fitted curves, the scattering length density profiles, and the parameter listing files, respectively.

-
- [1] V. Lauter-Pasyuk, H.J. Lauter, B.P. Toperverg, L. Romashev, V. Ustinov, Phys. Rev. Lett., **89**, 167203 (2002).
 - [2] J.F. Ankner, C.F. Majkrzak, D.A. Neumann, A. Matheny and C.P. Flynn, Physica B, **173**, 89 (1991).
 - [3] D.R. Lee, G. Srajer, M.R. Fitzsimmons, V. Metlushko, S.K. Sinha, Appl. Phys. Lett., **82**, 82 (2003).
 - [4] L.G. Parratt, Phys. Rev. **95**, 359 (1954).
 - [5] T.P. Russell, Annual Review of Materials Science, **21**, 249 (1991).
 - [6] J. Lekner, Theory of Reflection of Electromagnetic and Particle Waves, (Martinus Nijhoff Publishers, Dordrecht 1987).
 - [7] H. Dosch, Phys. Rev. B, **35**, 2137 (1987).
 - [8] G.H. Vineyard, Phys. Rev. B, **26**, 4146 (1982).
 - [9] S. Dietrich and H. Wagner, Z. Phys. B, **56**, 207 (1984).
 - [10] M. Tolan and W. Press, Z. Kristallogr., **213**, 319 (1998).
 - [11] G.S. Smith and C.F. Majkrzak, in the International Tables of Crystallography, edited by E. Prince, volume B, 3rd edition (Kluwer Academic Publishers, Dordrecht 2004).
 - [12] Y. Y. Huang, C. Liu, and G. P. Felcher, Phys. Rev. B **47**, 183 (1993).
 - [13] A. Hoffmann, J.W. Seo, M.R. Fitzsimmons, H. Siegwart, J. Fompeyrine, J.P. Locquet, J.A. Dura, C.F. Majkrzak, Phys. Rev. B, **66**, 220406 (2002).
 - [14] M.R. Fitzsimmons, P. Yashar, C. Leighton, I.K. Schuller, J. Nogues, C.F. Majkrzak, J.A. Dura, Phys. Rev. Lett., **84**, 3986 (2000).
 - [15] M. Gierlings, M.J. Prandolini, H. Fritzsche, M. Gruyters, D.Riegel, Appl. Phys. A, **74**, S1523 (2002).
 - [16] K. Temst, M.J. Van Bael, H. Fritzsche, J. of Magn. Magn. and Mater., **226**, 1840 (2001).
 - [17] H. Fritzsche, M.J. Van Bael, K. Temst, Langmuir, **19**, 7789 (2003).
 - [18] V. Leiner, K. Westerholt, A.M. Blixt, H. Zabel and B. Hjörvarsson, Phys. Rev. Lett., **91**, 037202-1 (2003).
 - [19] G.P. Felcher, R.O. Hilleke, R.K. Crawford, J. Haumann, R. Kleb, and G. Ostrowski, Rev. Sci. Instrum. **58**, 609 (1987).
 - [20] C.F. Majkrzak, Physica (Amsterdam) **221B**, 342 (1996).
 - [21] H. Dosch, Physica B, **192**, 163 (1993).
 - [22] J.A.C. Bland in Ultrathin Magnetic Structures, J.A.C. Bland and B. Heinrich (eds.), (Springer Verlag, Berlin, 1994).
 - [23] M.R. Fitzsimmons, S.D. Bader, J.A. Borchers, G.P. Felcher, J.K. Furdyna, A. Hoffmann, J.B. Kortright, Ivan K. Schuller, T.C. Schulthess, S.K. Sinha, M.F. Toney, D. Weller, S. Wolf, in press, J. Magn. Magn. Mater. (2004).
 - [24] S. Dietrich and H. Wagner, Z. Phys. B, **59**, 35 (1985).
 - [25] <http://www.lpm.u-nancy.fr/webperso/mangin.p/hercules/courshercules.html>
 - [26] J.F. Ankner and G.P. Felcher, J. of Magn. Magn. Mater., **200**, 741 (1999).
 - [27] W.G. Williams, Polarized Neutrons, (Clarendon Press, Oxford 1988).
 - [28] C.F. Majkrzak, K.V. O'Donovan and N.F. Berk, unpublished.
 - [29] E. Merzbacher, Quantum Mechanics, (John Wiley & Sons, Inc., New York 1970).

-
- [30] Additional scattering lengths can be obtained at <http://www.ncnr.nist.gov/resources/n-lengths/>.
 - [31] M. Born and E. Wolf, *Principles of Optics, Electromagnetic Theory of Propagation, Interference and Diffraction of Light*, (Pergamon Press, Oxford, 1980) p. 563.
 - [32] P.R. Bevington and D. K. Robinson, *Data Reduction and Error Analysis for the Physical Sciences*, 3rd edition, (McGraw-Hill Book Company, New York 2003) p. 2.
 - [33] P.G. Shewmon, *Diffusion in Solids*, (McGraw-Hill Book Company, New York 1963).
 - [34] P.R. Bevington and D. K. Robinson, *Data Reduction and Error Analysis for the Physical Sciences*, 3rd edition, (McGraw-Hill Book Company, New York 2003) p. 252.
 - [35] R.N. Bracewell, *The Fourier Transform and its Applications*, (McGraw-Hill Book Company, New York 1978).
 - [36] L. Nevot and P. Croce, *Rev. Phys. Appl.*, **15**, 761 (1980).
 - [37] B.E. Warren, *X-ray Diffraction*, (Dover Publications, Inc., New York 1990).
 - [38] F. Radu, A. Vorobiev, J. Major, H. Humblot, K. Westerholt, H. Zabel, *Physica B*, **335**, 63 (2003).
 - [39] R.K. Kawakami, Y. Kato, M. Hanson, I. Malajovich, J.M. Stephens, E. Johnston-Halperin, G. Salis, A.C. Gossard, D.D. Awschalom, *Science*, **294**, 131 (2001).
 - [40] D.J. Hughes and M.T. Burgy, *Phys. Rev.*, **76**, 1413 (1949).
 - [41] J. Schwinger, *Phys. Rev.* **51**, 544 (1937).
 - [42] F. Bloch, *Phys. Rev.* **50**, 259 (1936).
 - [43] D.J. Hughes and M.T. Burgy, *Phys. Rev.*, **81**, 498 (1951).
 - [44] M.R. Fitzsimmons, M. Lütt, H. Kinder and W. Prusseit, *Nucl. Inst. and Methods, Section A*, **411**, 401 (1998).
 - [45] F. Mezei, *Z. Physik*, **255**, 146 (1972).
 - [46] J.D. Jackson, *Classical Electrodynamics*, (John Wiley & Sons, Inc. New York 1975).
 - [47] E. E. Fullerton, D.M. Kelly, J. Guimpel, I.K. Schuller, and Y. Bruynseraede, *Phys. Rev. Lett.* **68**, 859 (1992).
 - [48] H. Ohno, *Science* **281**, 951 (1998).
 - [49] M. Born and E. Wolf, *Principles of optics: electromagnetic theory of propagation, interference and diffraction of light*, (Pergamon Press, New York 1980).
 - [50] W.T. Lee, S.G.E. te Velthuis, G.P. Felcher, F. Klose, T. Gredig, E.D. Dahlberg, *Phys. Rev. B*, **65**, 22417 (2002).
 - [51] S.G.E. teVelthuis, A. Berger, G.P. Felcher, B.K. Hill, E.D. Dahlberg, *J. of Appl. Phys.*, **87**, 5046 (2000).
 - [52] F. Mezei, *Comm. on Physics*, **1**, 81 (1976).
 - [53] F. Mezei and P.A. Dagleish, *Comm. on Physics*, **2**, 41, (1977).
 - [54] D. Clemens, P. Böni, H.P. Friedli, R. Göttel, C. Fermon, H. Grimmer, H. van Swygenhoven, J. Archer, F. Klose, Th. Krist, F. Mezei, P. Thomas, *Physica B*, **213 & 214**, 942 (1995).
 - [55] P. Høghøj, I. Anderson, R. Siebrecht, W. Graf and K. Ben-Saidane, *Physica B*, **267**, 355 (1999).
 - [56] P. Dhez and C. Weisbuch, eds., *Physics, Fabrication and Applications of Multilayered Structures*, NATO ASI Series B, **182** (Plenum Press, New York 1988).

-
- [57] C. Majkrzak, ed., Proc. Conf. On Thin-film Neutron Optical Devices, San Diego, USA, August 1988 SPIE Proc., **983** (Bellingham, WA 1989).
 - [58] F. Mezei in: Use and Development of Low and Medium Flux Research Reactors, eds., O.K. Harling, L. Clark and P. von der Hardt, Supplement to Atomenergie-Kerntechnik, **44** (Karl Thiemig, München 1984) p. 735.
 - [59] J.B. Hayter in Neutron Diffraction, ed. H. Dachs, (Springer Verlag, Berlin 1978).
 - [60] C.P. Slichter, Principles of Magnetic Resonance, (Springer Verlag, Berlin 1980).
 - [61] G. Badurek, Nucl. Instr. and Methods, **189**, 543 (1981).
 - [62] O. Scharpf in Neutron Spin Echo, ed. F. Mezei (Springer-Verlag, Berlin 1980) pp. 27-52.
 - [63] R. Herdin, A. Steyerl, A.R. Taylor, J.M. Pendlebury and R. Golub, Nucl. Instr. and Methods, **148**, 353 (1978).
 - [64] T. Keller, T. Krist, A. Danzig, U. Keiderling, F. Mezei, A. Wiedenmann, Nucl. Instr. and Methods A, **451**, 474 (2000).
 - [65] S.Park, M.R. Fitzsimmons, X.Y. Dong, B.D. Schultz and C.J. Palmstrøm, submitted to Phys. Rev. B.
 - [66] L.C. Chen, J.W. Dong, B.D. Schultz, C.J. Palmstrøm, J. Berezovsky, A. Isakovic, P.A. Crowell and N. Tabat, J. Vac. Sci. Technol. **B18**, 2057 (2000).
 - [67] B.D. Schultz, H.H. Farrel, M.M.R. Evans, K. Lüdge, and C.J. Palmstrøm, J. Vac. Sci. Technol. **B 20**, 1600 (2002).
 - [68] M. Lütt, M.R. Fitzsimmons, D. Li, *J. Chem. Phys. B*, **102**, 400(1998).
 - [69] P.R. Bevington and D. K. Robinson, Data Reduction and Error Analysis for the Physical Sciences, 3rd edition, (McGraw-Hill Book Company, New York 2003) p. 67.
 - [70] W.H. Press, B.P. Flannery, S.A. Teukolsky, and W.T. Vetterling, *Numerical Recipes, the art of scientific computing*, (Cambridge University Press 1986) p. 536.
 - [71] J.W. Cable, M.R. Khan, G.P. Felcher and I.K. Schuller, Phys. Rev. B **34**, 1643 (1986).